Development of an Aeroelastic Model for a Flared Folding Wing Tip

An exploration into the multibody framework of PROTEUS

Aakash Ghosh

Technische Universiteit Delft

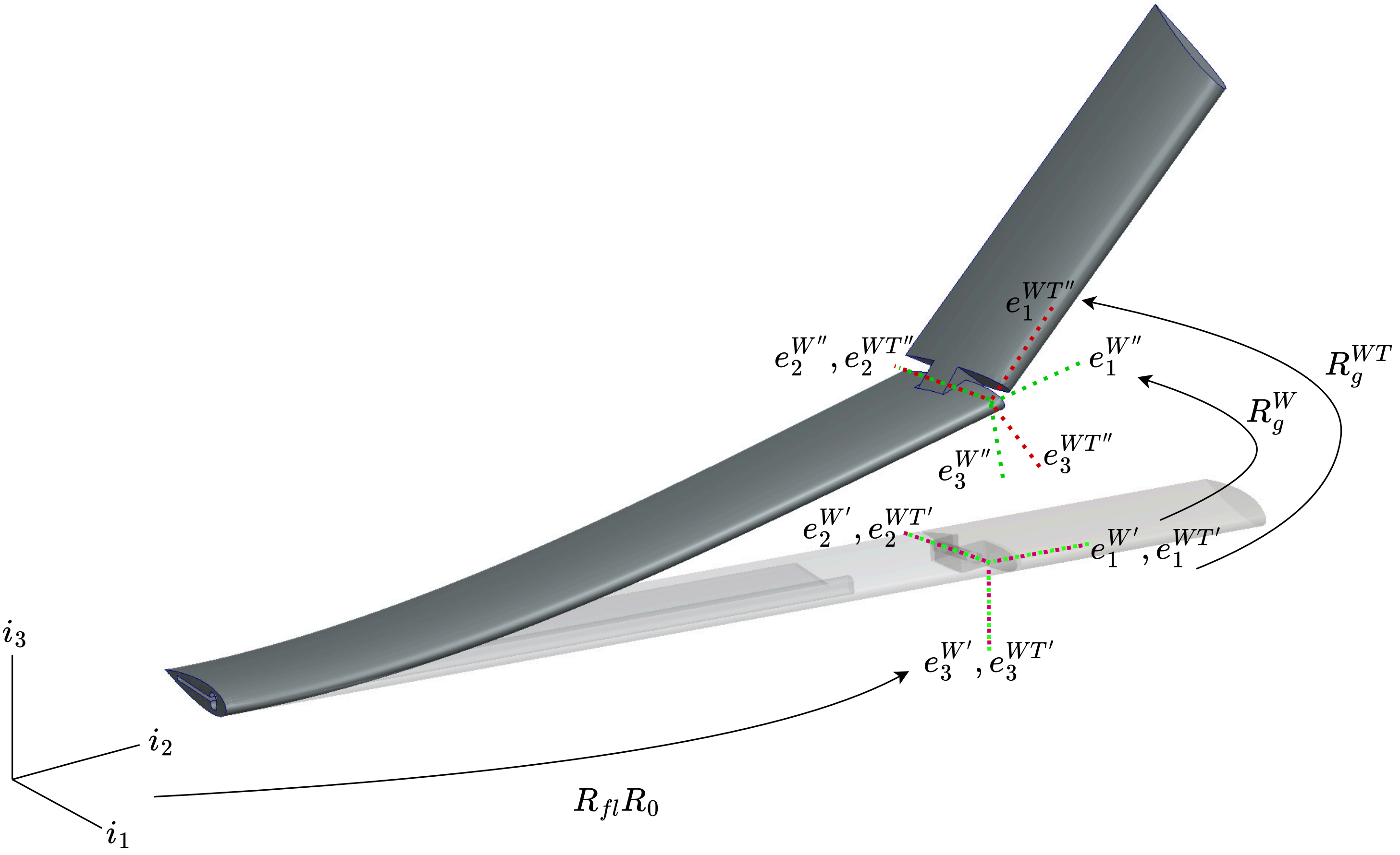

Development of an Aeroelastic Model for a Flared Folding Wing Tip

An exploration into the multibody framework of PROTEUS

by

Aakash Ghosh

to obtain the degree of Master of Science at the Delft University of Technology, to be defended publicly on Wednesday, February 26th, 2025 at 13:00 PM.

Student Number:	5772532	
Project Duration:	July, 2024 - January, 2025	
Thesis Committee:	Dr. Sergio Turteltaub	TU Delft, ASM, Chair
	Dr. Xuerui Wang	TU Delft, ASM, External Examiner
	Dr. Jurij Sodja	TU Delft, ASM, Daily Supervisor
	Ir. Xavier Carrillo Córcoles	TU Delft, ASM, Daily Supervisor

Date: February 18, 2025

Delft
University of Technology

Acknowledgements

Words here cannot fully encompass my gratitude and respect for my supervisor, Dr. Jurij Sodja. Getting to know him, his focus, and his passion for aeroelasticity has motivated me throughout the past year. His support and mentorship, from my honours project to the completion of my master's thesis, have been truly invaluable. A special thanks to Xavi, whose guidance over the past few months made it possible to finish this thesis. Helping me trick PROTEUS countless times and opening this Pandora's box of new challenges, while patiently guiding me through my mistakes and assisting with coding, I am truly grateful.

I am extremely lucky to have a family away from home, Arno & Angie, helping me take my mind off of my problems on the dullest of weekends and feeding me delicious dinners. My brothers in arms - Harsha and Murali- from choosing this track two and a half years ago to finishing it, we did it! I am truly thankful to Bhatia for sitting beside me throughout the dark winter days in the faculty & library, and to Kaushik for the weird discussions we'd have during our runs. Thank you guys for putting up with me and my jokes; the lore we have written over the past few years is priceless.

Finally and most importantly: to my mother, who constantly reminded me to eat my meals, and to my father, who continues to be my idol to date: thank you for your unwavering support and love, there is no chance I would have made it this far without you two.

Aakash Ghosh

Delft, February 2025

Abstract

Flared folding wing tips (FFWTs) improve aerodynamic efficiency but present aeroelastic challenges. This study develops an FFWT aeroelastic model using: (i) multibody constraint formulation for kinematics, (ii) non-linear static analysis for equilibrium under aerodynamic loading, and (iii) linearised dynamic analysis for time-dependent behaviour.

The multibody formulation defines the wing tip's motion through hinge constraints, while the non-linear static analysis examines the effects of flare angles on equilibrium fold angles and reaction forces. The wing root bending moment (WRBM) decreases by 17% compared to a locked configuration but increases by 23.4% as the flare angle grows from 0° to 20°. For flare angles below 10°, the solver characteristics and initial equilibrium positions at lower velocities can lead to numerical issues such as zero-division errors and poorly conditioned matrices.

The linearised dynamic model, based on the static solution, is evaluated with different configurations: a locked hinge, a free hinge, and a locked-free hinge. Smaller flare angles allow higher fold angles but introduce minor anomalies in the inner wing tip's response, while larger flare angles improve numerical stability yet cause more persistent oscillations. The locked-free case assesses hinge release during a gust encounter, where releasing the hinge at peak gust intensity leads to larger persistent oscillations. Artificial numerical diffusion and structural damping effectively reduce numerical noise in reaction moments, revealing underlying trends and improving stability.

Contents

List of Figures

Nomenclature

Abbreviations

AR	Aspect ratio of the wing	
AoA	Angle of Attack	deg
CFD	Computational Fluid Dynamics	
CS-25	Certification Specifications for Large Aeroplanes (EASA)	
DLM	Doublet Lattice Method	
EASA	European Union Aviation Safety Agency	
FFAST	Future Fast Aeroelastic Simulation Technologies	
FFR	Floating Frame of Reference	
FFWT	Flared Folding Wing Tip	
GAF	Generalized Aerodynamic Forces	
GLA	Gust Load Alleviation	
MLA	Manoeuvre Load Alleviation	
PTWT	Passive-Twist Wing-Tip	
RMS	Root-Mean Square	
SVG	Switchable Vortex Generators	
TE	Trailing Edge	
UVLM	Unsteady Vortex Lattice Method	
WRBM	Wing Root Bending Moment	

Greek Symbols

α_{air}	Angle of attack induced by the free-stream flow	°
χ	Diffusion coefficient	
$\Delta\alpha$	Variation of angle of attack due to deflection	deg
$\Delta\phi_b$	Velocity potential difference of the wing-body	
$\Delta\phi_w$	Velocity potential difference of the wake	
ϵ	Strain vector	
γ	Loading parameter	
Γ_b	Vortex strength	m^2/s
Γ_w	Wake vortex strength	m^2/s

Λ	Flare angle	deg
λ	Lagrange Multiplier	
λ_h	Lagrange multiplier for holonomic constraints	
λ_n	Lagrange multiplier for non-holonomic constraints	
$\Phi(\mathbf{p})$	Constraint function	
$\mathcal{W}$	Strain energy functional	J
Ω	Ratio of circular frequency to true airspeed	
ω	Circular frequency	rad/s
$\phi(\Omega)$	Power spectral density	m^2/s
Φ^*	Total velocity potential	m^2/s
ρ	Fluid density	
σ^2	Root-mean-squared velocity	$(\mathrm{m}/\mathrm{s})^2$
θ	Fold angle	deg
θ_h	Rotation angle in the hinge frame	rad
θ_s	Pseudo-vectorial representation of the rotation	rad
θ_t	Angle of attack due to the wing twist	°

Latin Symbols

$\mathfrak{R}$	Rotation matrix (Co-Rotational Framework)	
$\mathbf{A_{ss}}$	State Matrix	
$\mathbf{B_h}$	Jacobian matrix for holonomic constraints	
$\mathbf{B_n}$	Jacobian matrix for non-holonomic constraints	
$\mathbf{B_{ss}}$	Input Matrix	
$\mathbf{C_{eq}}$	Equivalent output formulation to resolve constraint forces	
$\mathbf{C_{ss}}$	Output Matrix	
$\mathbf{C}$	Damping matrix	
$\mathbf{D_{eq}}$	Equivalent feedthrough formulation to resolve constraint forces	
$\mathbf{D_{ss}}$	Feedthrough Matrix	
$\mathbf{F}_\lambda$	Reaction forces of the Constraints	
$\mathbf{F_{ext}}$	External forces	N
$\mathbf{F_s}$	Structural internal forces	N
$\mathbf{H}$	Selection Arrays to transfer correlating aerodynamic data	

$\mathbf{K_i}$	Input Transfer matrices $(i = 1, 2, \ldots)$	
$\mathbf{K_{st}}$	Influence coefficients of the wing and the semi-infinite wake	
$\mathbf{K}$	Stiffness matrix	
$\mathbf{L_i}$	Output Contribution matrices $(i = 1, 2, \ldots)$	
$\mathbf{M}$	Mass matrix	
$\mathbf{p}$	Degrees of freedom containing displacements and rotations	
$\mathbf{Q}$	Generalized Aerodynamic Force matrix	
$\mathbf{RAS}$	Selection Arrays to transfer aerodynamic input to Structural coordinates	
$\mathbf{T}_\alpha$	Coupling matrix for angle of attack	
$\mathbf{T_n}$	Coupling matrix for normal forces	
$\mathbf{T_t}$	Coupling matrix for twist angle	
$\mathbf{T_{AS}}$	Aero-to-Structural Transfer Matrix	
$\mathbf{V}_\infty$	Free-stream velocity	m/s
$\mathbf{V_w}$	Wake velocity	m/s
$\mathbf{x}$	State Vector	
$\mathbf{X}_{c2f}$	Inverse Reduction Matrix to convert the state vector from reduced to complete form	
$\mathbf{y}$	Output Vector	
a	Slope of the aircraft's normal force coefficient curve	
C	Cross-sectional stiffness tensor	$\mathrm{N/m^2}$
C_l	Coefficient of lift	
C_{d_i}	Induced drag coefficient	
$C_{N_{A\max}}$	Maximum normal force coefficient	
e	Efficiency factor of the wing	
e^W	Nodal Triad for the Inner Wing Tip	
e^{WT}	Nodal Triad for the Root of the FFWT	
F_g	Flight profile alleviation factor	
F_L	Lift force	N
g_h	Holonomic constraint function	
g_n	Non-holonomic constraint function	
H	Distance between zero to maximum gust velocity	m
i	Unit vector defining the FFWT's orientation	

i_0	Undeformed configuration vector	
K_g	Gust alleviation factor	
K_θ	Stiffness coefficient for hinge	Nm/rad
L	Gust length	m
M	Moments	Nm
$M_{\max}$	Maximum allowable hinge moment	Nm
M_{NL}	Nonlinear hinge moment	Nm
n	Positive manoeuvring load factor at cruise speed	
q_i	Bubble function coefficients ($i = 1, .., n$)	N/m^2
r_g	Position vector of the FFWT relative to the hinge	m
s	Penetration distance	m
S	Plate area (reference area)	
t	Time	s
T_W, T_{WT}	Transformation matrices, also referred to as tangent operators, for the wing tip and FFWT root nodes, respectively.	
t_{release}	Time at release	s
U	Maximum gust velocity	m/s
$u(s)$	Gust velocity as a function of penetration distance s	m/s
u_h	Translation displacement in the hinge frame	m
U_{ds}	Design gust velocity	m/s
U_{ref}	Reference gust velocity	m/s
V	True airspeed of the aircraft	m/s
V_A	Design Manoeuvring Speed	m/s
V_B	Design speed for maximum gust intensity	m/s
V_C	Design cruise speed	m/s
V_{S1}	Stalling speed with retracted wing flaps	m/s
w	Average wing loading (in pounds per square foot)	lb/ft^2
x_h	Position of the hinge	m
z_g	Centre of gravity of the FFWT relative to the undeformed reference	m
b	Semi-Chord Length	m
k	Reduced Frequency	

I

Introduction

1 Introduction to Core Concepts

Bio-mimicry is the science of developing designs or concepts inspired by nature. Evolution has led every species to adapt to their surrounding environmental conditions and these adaptations can be incorporated into current designs to improve their efficiency. Bio-inspired designs can be found everywhere in the aerospace sector, from aircraft structural design to the control laws used to fly and stabilise them. Biomimetics can be used to improve current designs which is critical to increasing flight efficiency to meet the global demand while limiting emissions. From a global perspective, aviation only accounted for around 3% of CO_2 emissions in 2019 but is projected to increase by around 2.6 times by 2050 based on the rising demand for aviation [9]. Hence sustainable solutions in aviation have become increasingly important. Aviation can be regarded as one of the most problematic industries for reducing emissions due to its dependability on energy-dense fuels. The industry must incorporate new and radical technologies to achieve such an ambitious goal while catering for the increase in passengers.

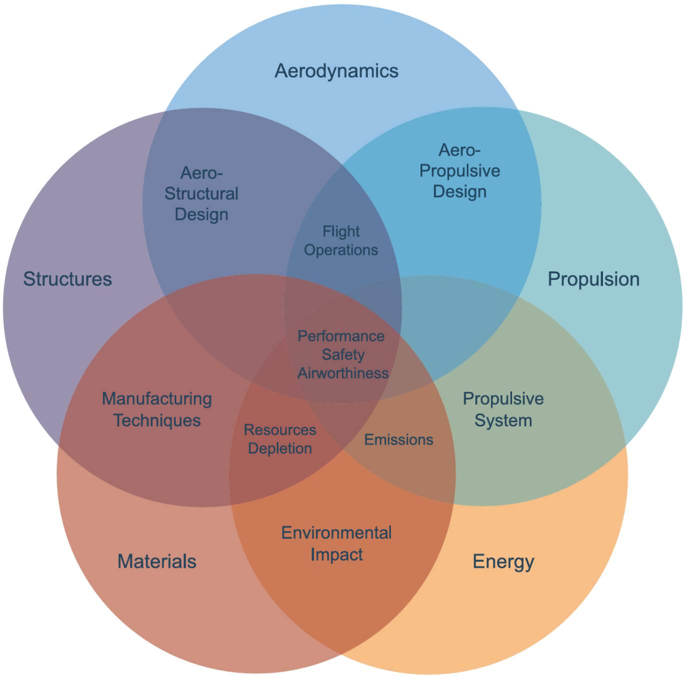

Figure 1.1: Disciplines contributing to Sustainable Aviation [2]

Sustainable development in aviation is a highly interlinked and multidisciplinary field and the main contributors can be posed through a Venn diagram presented by Afonso et al. (2023)[2], in Figure 1.1. Emission reductions can be achieved through developments in propulsion systems and by the use of Sustainable Aviation Fuels (SAFs) or by the integration of hydrogen or electric propulsion systems, however, to maintain the performance of these systems the other aspects of the Venn diagram play a major role. Similarly, the propulsion demand of an aircraft can be reduced by making its structures lighter and its designs more aerodynamic, however, from an aero-structural point of view, this can introduce an aircraft with new instabilities as the interaction between the flow and the structure may become more prominent. These instabilities can also occur in current aircraft designs. To ensure safe flight operations, aircraft performance is constrained within a defined set of parameters known as the flight envelope. The flight envelope represents the boundaries of speed, altitude, and manoeuvrability within which the aircraft can operate safely without encountering unstable or dangerous conditions. By adhering to these limits, pilots and automated systems can prevent the aircraft from entering regimes where instabilities are more likely to occur.

To ensure safety, the structure must be designed to withstand the manoeuvre and gust loads dictated by the flight envelope, often resulting in the need for heavier structures with high safety factors. However, since the flight envelope is fundamentally determined by these loads, reducing them through load alleviation could enable a reduction in structural weight. To circumvent this issue load management of these structures must be improved. Several solutions have been researched ranging from tailored materials for the wings to control structural deformation to the use of dedicated load alleviation techniques. This research delves into one of those dedicated load alleviation concepts known as the *Flared Folding Wing-Tip (FFWT)*. The FFWT can be categorised as a gust-load alleviation device that can be initiated in flight. This concept allows longer in-flight wing spans which help improve aerodynamic efficiency, and the folded configuration allows the aircraft to comply with airport gate regulations. This study will aim to model the flared hinge into the in-house aeroelastic optimization software, PROTEUS. Incorporation of the hinge into PROTEUS will allow further optimizations of the concept, where the effect of aeroelastic tailoring and control surface deployment can be explored.

This chapter forms the knowledge base for the succeeding chapters. Hence, the following sections are designed to introduce the fundamental concept of aeroelasticity (Section 1.1). Section 1.2 introduces the concept of gusts and the different models used to handle them for analysis. Section 1.3 elaborates on the different *active* and *passive* systems developed to reduce loads during manoeuvres and gust encounters.

1.1. Aeroelasticity

Aeroelasticity is the study of the effects arising from the interaction between flow and structure. Aeroelastic effects become relevant when there is significant interaction between the flow and the structure. These interactions can be categorised based on the forces due to which they arise and can be elegantly portrayed using Collar's triangle.

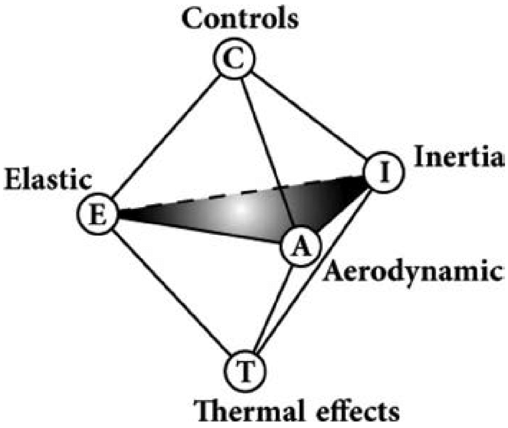

Figure 1.2: Extended Collar's Triangle [3]

Aerodynamic forces can be classified as the forces rising due to the flow around the structure and the elastic forces are forces due to the elastic or structural properties of the object in question. Inertial forces are those rising from the mass and the acceleration of the object. These three corners complete the classic Collar's shaded triangle. The interaction between the elastic and aerodynamic forces classify *static aeroelasticity* as inertial forces are neglected, similarly, the study relating only to the inertial forces and the elastic forces is classified as structural dynamics. Lastly, the study relating the aerodynamic forces and inertial forces is classified as aerodynamic stability problems. Combining all three corners of the classic triangle represents *dynamic aeroelastic problems*. Further interactions have been incorporated into the extended Collar's triangle by including the forces arising from controls and thermal effects. Control forces account for the dynamic influence of flight control systems, such as actuators and aerodynamic surfaces, which can affect the stability and performance of the structure. Thermal effects, on the other hand, consider the impact of temperature variations and heat loads, which can lead to material expansion, stress redistribution, and changes in structural properties. Together, these factors introduce additional complexities in the interaction between aerodynamic, inertial, and elastic forces, necessitating advanced analysis and design strategies to ensure overall system stability and performance.

1.2. Gusts

Gust loads can be classified as a mixed interaction of the upper half of the extended Collar's triangle, making it a dynamic aeroelastic problem. Gusts are essentially variations in free-stream velocity which can act on the plane from any direction [10]. Such events can increase the loads on the wing and have the possibility to cause dynamic instabilities, hence such events must be taken into account when designing the structures. Gusts are studied in aeroelasticity with two main types of models: discrete and continuous.

1.2.1. Discrete Gust Models

Discrete gusts include defined velocity profiles, hence the event is deterministic and usually solved in the time domain [11]. There are three standard discrete gust profiles used namely: *sharp-edge*, *linear-ramp* and the *1-cosine* gust profile. The sharp-edge gust is one of the simplest representations of gust and can be represented with the following equation [12]:

$$\frac{u(s)}{U} = 1 \tag{1.1}$$

Here U is the maximum gust velocity and $u(s)$ is gust velocity as a function of the penetration distance, s.

Another representation of gust which was adopted in the late 1930s is the linear-ramp gust. This model presents a linear relationship between the gust velocity and the distance from zero to maximum gust velocity, H [12].

$$\begin{cases} \frac{u(s)}{U} = \frac{s}{H} \quad (0 < s < H) \\ \frac{u(s)}{U} = 0 \quad (s < 0 \quad \text{or} \quad s > H) \end{cases} \tag{1.2}$$

The 1-cosine gust profile is widely used for modelling discrete gust responses, and current regulations adopt it for aircraft certification. This preference stems from its mathematical simplicity and its ability to provide a gradual aerodynamic input that closely resembles real-life gust encounters, unlike an idealised step function. Depending on the chosen modelling parameters, the 1-cosine profile can simulate a range of aerodynamic loads, from unsteady to quasi-steady conditions. Additionally, by adjusting the gust frequency to align with the structure's eigenfrequencies, it enables analysis of non-linear aeroelastic responses. Equation 1.3 gives the mathematical representation of the gust model [12].

$$\begin{cases} \frac{u(s)}{U} = \frac{1}{2}\left(1 - \cos\frac{\pi s}{H}\right) \quad (0 < s < 2H) \\ \frac{u(s)}{U} = 0 \quad (s < 0 \quad \text{or} \quad s > 2H) \end{cases} \tag{1.3}$$

This $1 - \cos$ gust profile is graphically represented in Figure 1.3.

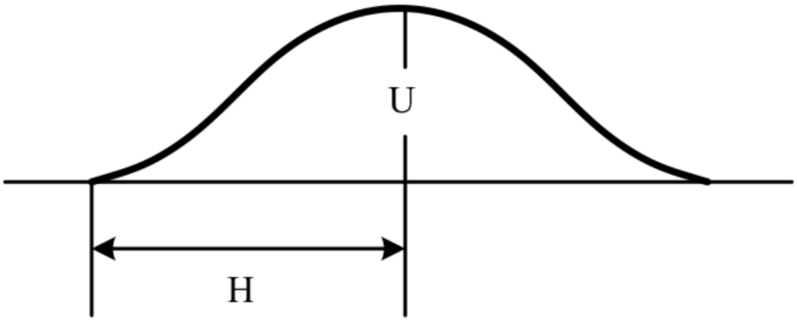

Figure 1.3: 1 – cosine Gust Shape for Arbitrary Values

H is the half-gust length, signifying the distance (parallel to flight direction) for the gust to reach its maximum velocity. The EASA CS-25 [13] states that critical responses must be analysed for H-values in the range of $9m$ to $107m$. The design gust velocity can be further calculated from the following expression:

$$U_{ds} = U_{ref} F_g \left(\frac{H}{107} \right)^{1/6} \tag{1.4}$$

U_{ref} and F_g are the reference velocities and the flight profile alleviation factor which are further expressed in the CS-25 [13].

1.2.2. Continuous Gust Models

Continuous gust models are statistical representations of gusts. These models try to emulate the continuous and random nature of real atmospheric turbulence. These statistical representations of continuous gust velocity profiles can be used to derive the dynamic responses of an aircraft and are presented in the frequency domain. Two main shapes of continuous gusts are the von Karman and the Dryden spectra which are defined by Equation 1.5 and Equation 1.6 respectively.

$$\phi(\Omega) = \sigma^2 \frac{L}{\pi} \frac{1 + \frac{8}{3}(1.339\Omega L)^2}{[1 + (1.339\Omega L)^2]^{\frac{11}{6}}} \tag{1.5}$$

$$\phi(\Omega) = \sigma^2 \frac{L}{\pi} \frac{1 + 3(\Omega L)^2}{[1 + (\Omega L)^2]^2} \tag{1.6}$$

In both these spectra, a Gaussian distribution is assumed. The European Union Aviation Safety Agency (EASA) uses the von Karman spectra to describe turbulence for large aircraft [13]. σ^2 defines the root-mean squared velocity of the flight, $\phi(\Omega)$ is the power spectral density and L is the gust length as defined in EASA guidelines [13]. Ω is the ratio between the circular frequency (ω) and the aeroplane's true airspeed (V).

1.3. Load Alleviation

There are two main forms of dynamic loads which act on the aircraft which can be categorised into manoeuvre loads and gust loads. An aeroplane can perform manoeuvres in the horizontal plane or its vertical plane. On the vertical plane, the plane can "climb" or "dive" by changing the trim and creating a moment about its centre of gravity. On the other hand, the plane can perform "yaw" or "roll" on its horizontal plane. All such manoeuvres exert loads on the aircraft's structure and hence the design of structures must be done by taking *probable* manoeuvres into account. While, gusts can be seen as atmospheric turbulence, and the topic of gust alleviation systems has been explored extensively. Manoeuvre load alleviation and gust load alleviation systems are classified based on these load cases encountered by an aircraft.

The EASA CS-25 regulations define several key design speeds that form the basis for establishing the flight envelope and corresponding structural load limits. These speeds correlate different operating conditions (such as manoeuvres and gust encounters) to load factors, n, ensuring the aircraft structure can safely withstand the induced loads[13].

- V_A (Design Manoeuvring Speed): This is the speed below which full control deflection can be applied safely without risking structural damage. It is defined by the relation: $V_A \geq V_{S1}\sqrt{n}$, where V_{S1} is the stalling speed with retracted wing flaps and n is the positive manoeuvring load factor at cruise speed. Essentially, V_A marks the upper limit of speeds where the aircraft's response to control inputs remains within safe structural bounds.

- V_B (Design Speed for Maximum Gust Intensity) EASA CS-25 requires that the design speed for maximum gust intensity, V_B, must not be less than:

  $$V_B \geq V_{sl}\sqrt{1 + \frac{K_g\, U_{\text{ref}}\, V_C\, a}{498\, w}}, \tag{1.7}$$

  where
  - V_{sl} is the 1-g stall speed (flaps retracted) at the weight under consideration.
  - V_C is the design cruise speed.
  - U_{ref} is the reference gust velocity
  - w is the average wing loading (in pounds per square foot).
  - a is the slope of the aircraft's normal force coefficient curve.
  - K_g is a gust alleviation factor determined by wing loading and aerodynamic characteristics.

  This formulation stresses the importance of gust loading experienced by the aircraft's structure and establishes a defined margin of safety. By reducing the loading on the wing, this margin of safety can be minimised, paving the way for the design of lighter structures.

- V_C (Design Cruise Speed): This represents the speed at which the aircraft is expected to operate during the cruise phase of flight. The design at V_C ensures that the structure is optimised for the typical aerodynamic loads encountered in normal operations. This speed is prescribed to be much larger than V_B to model worst-case scenarios due to atmospheric turbulence.

- V_D (Dive Speed): This speed is related to the limits encountered during high-speed or extreme conditions, such as dives. It provides an additional margin for ensuring the structural integrity of the aircraft when exposed to transient or extreme load cases.

Each of these speeds is integral to the overall structural design strategy. By defining the load cases over the operating envelope, techniques such as manoeuvre load alleviation can be applied [14]. These techniques, whether through deflecting control surfaces or employing aeroelastic tailoring, adjust the distribution of aerodynamic loads, leading to reduced peak loads and bending moments on the wing. This reduction enables the design of lighter wing-box structures without compromising safety or performance.

While manoeuvre load alleviation covers methods for reducing loads during manoeuvres, gust load alleviation strategies are implemented to reduce the loads acting on the structure due to a gust. Multiple methods to tackle such loading scenarios can be broadly sub-categorised into *active* and *passive* systems.

The conceptual difference between active and passive systems is that active systems require external energy and tend to adapt and work with real-time inputs, while passive systems do not require input energy to be activated and are not controlled using real-time inputs, hence their response time can generally be quicker than that of an active control system.

1.3.1. Active Systems

Active systems are those which make use of sensors and actuators to alter control surfaces on the wings (i.e. flaps, spoilers, elevators) to react to atmospheric changes. A common active load alleviation system incorporated in an aircraft involves deflections of control surfaces to create opposing forces and moments to stabilize the aircraft. The main objective of using flap-based load alleviation systems is to initiate a local lift re-distribution which causes the lift forces to act further inboard towards the wing root resulting in reduced wing root bending moments. White (1971) [15] discussed a practical approach to the use of flaps and ailerons to achieve the aforementioned load distribution for MLA, and a critical finding of the research is that with such load reduction, longer spans can be made possible but also with reduced wing root bending moments, the structure can be further optimised resulting in further weight savings. White (1971) studied several control surface designs, including a hinged wing tip, which provided highly beneficial MLA as well as was suggested to help improve the roll characteristics of the aircraft. Similar studies were also performed by Karpel (2007) [16] where three different control surface configurations were modelled and compared. A baseline arrangement was kept with normal ailerons which was compared against a model with forward-placed under-surface control surfaces placed at 0.8 wingspan and a special wing tip forward control surface. A clear advantage was realised with the use of the *special* control surfaces, especially at higher speeds.

Heinze & Karpel (2006) [17] also performed experimental tests on a piezoelectric actuated tab to control a floating control surface. The paper's objective was to study the dynamic aeroelastic response of the tab when the control surface is under floating conditions. The study also presents an MSC/NASTRAN numerical model of the wind tunnel wing to study appropriate control laws that can be used to optimize the flutter behaviour further. However, key practical issues were also noticed: at lower frequencies effect of the floating tab was counteracted by the deflection of the tab. Furthermore, the flap deflection is limited. Moreover, it was seen that the flap had to have no rotational stiffness and damping to alleviate severe aero-servoelastic instabilities. A gust response study was also performed with a simplistic control law, that proved that structural vibrations can be significantly reduced using the concept. This system hence was further extended and a secondary purpose of energy harvesting was also identified by Bernhammer et al. (2014) [18, 19], where it was realised that such a system can be self-powered.

Another system computationally studied by Ajjour et al. (2022) [20] utilised a lower surface spoiler to reduce the bending moments to reduce gust load alleviation. The study discusses how the sole use of the upper spoiler increased torsional loads while a combined use of the upper and lower spoiler was able to achieve 14 % bending moment relief under a 2.5g symmetric manoeuvre. Such load alleviation systems, however, seem to be highly dependent on the control systems holding them together. To achieve optimal load alleviation, the response of these control surfaces must be optimised as well, which is also reflected by the authors.

The research in mechanical control-surface-based GLA systems also depends on the improvement of sensing and actuating technology. A key research branch is in the use of dynamic flaps. Dynamic flaps are those which are actuated in a specific way under a gust encounter, as opposed to constant actuation wherein, the flaps get deflected through a constant motion [21]. Ullah et al. (2022) [22] studies the use of active segmented leading edge flaps and trailing edge flaps for active gust alleviation using steady, dynamic and superimposed steady and combined deflection concepts. The superimposed flap actuation is done in steps where the steady flap deflection is used in order to redistribute the load to reduce the inherent structural loads *before gust encounter*, followed by the dynamic flap deflection upon gust encounter. The study showed significant improvement in load alleviation however it was noted that wing torsional moment was still quite high. Another study by Klug et al. (2020) [23] explores different actuator concepts on the DLR LEISA configuration at transonic speeds. The study finds that a combination of leading edge and trailing edge flaps shows great potential in alleviating gust loads. The study also explores two wing configurations namely. a forward-swept and a backward-swept configuration. The use of fuselage flaps shows minimal contribution in GLA, while the application of wing tip flaps on the forward swept wing results in a very favourable redistribution of loads.

Another novel method being researched to control the flow over the wing to achieve gust load alleviation is switchable vortex generators (SVG) [4]. The device works by changing its orientation to cater for high AoA as well as high-speed load cases. During gusts, the SVGs can align perpendicular to the airflow acting analogous to a Gurney flap and reducing the lift of the wing. During high-lift scenarios, the SVGs can be set parallel to the airflow working as vortex generators and delaying flow separation. The working principle of the GLA device is presented in Figure 1.4.

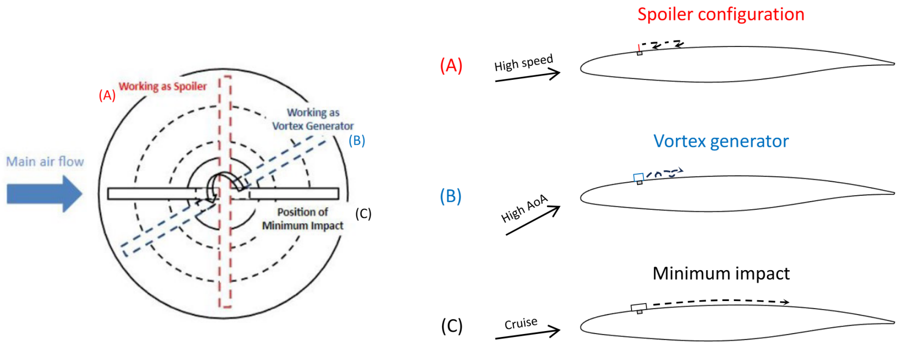

Figure 1.4: Working principle of the Switchable Vortex Generator (SVG) as presented by Luca et al. (2024) [4]

3D computational fluid dynamic-based parametric performed by Luca et al. (2025) [24] suggest that the concept is successful in performing load alleviation. However, based on the load profile, the study suggests that key geometric parameters must be changed to achieve optimal results.

Furthermore, current research also focuses on the use of active flow control by inserting fluid jets on the lift surface [25]. Li et al. (2022) present a comprehensive review of the different non-conventional gust load alleviation devices. There exists a plethora of research which have explored the use of synthetic jets, blowing-suction devices as well as Coandă-based circulation control devices to improve the aerodynamic characteristics of the wing. Coandă-based controls revolve around the Coandă effect, wherein the flow follows the outer shape of the protuberance present in the flow [25]. These devices work by disrupting the flow over the wing and thereby the circulation created by the wing, hence altering the loads on the wing. Though these devices provide a potential solution that may require fewer moving parts and faster response times, Li et al. (2022) conclude that such systems still need more research to improve their load control characteristics.

Although the use of active systems is much easier to adopt and integrate into current configurations, there exist certain drawbacks, one primary issue regarding the use of active flow control is the phase lag between actuation and gust encounter. Furthermore, a possible drawback that can be highlighted with active mechanical devices, such as the switchable vortex generator, is that optimised results can only be achieved by tailoring key geometric parameters of the device, which may be complex to achieve in-flight. Issues also arise in the use of fluidic actuators wherein a decrease in load alleviation is noted with higher incoming flow speeds [25]. Hence, passive systems, have certain functional benefits when compared to active systems, as they do not require complex control systems nor extensive tailoring to achieve load alleviation. The following section presents some of these passive systems being researched.

1.3.2. Passive Systems

One major area of research regarding passive systems is aeroelastic tailoring. Aeroelastic tailoring is the term given to the multi-disciplinary optimization of composites by making use of their directional stiffness to target aeroelastic loads. Common composite stacks include the use of $0^o/\pm45^o/90^o$ angled unidirectional plies, this is mainly due to the strongly developed existing knowledge base on the use of these plies, however with the advancement of fibre placing strategies with the introduction of automated fibre placement (AFP), variable stiffness laminates can be created. This method allows continuous variation of fibres among laminates and helps integrate ply continuity in the optimisation framework [26]. Ply continuity is an important design consideration as significant differences between adjacent plies can negatively affect the structural integrity of the overall structure[27]. Furthermore, as an effort to reduce structural weight, wing-box designs are made with the use of multiple zones, wherein each zone has its composite orientation. This leads to a direct increase in the design variables needed for the optimization. Although the use of aeroelastic tailoring can be beneficial, the overall gust-load alleviation may be limited given the overall design variables which must also be satisfied for a safe design.

Another passive load alleviation technology is the use of bi-stable structures. Bi-stable structures can be described as those which have multiple equilibria in a post-buckled state. Hence under dynamic loading, they can "snap-through" to a different stable state. This behaviour can be exploited to morph wing geometry as shown by Kuder et al. (2016) [5], where they use bi-stable laminates to *morph* the trailing edge section, as represented in Figure 1.5.

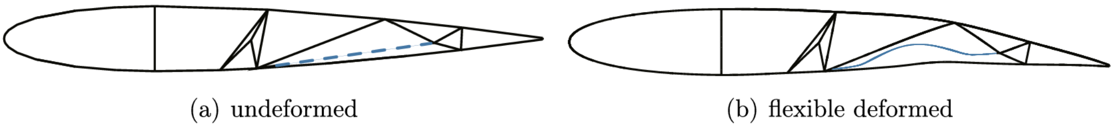
(a) undeformed (b) flexible deformed

Figure 1.5: Undeformed (a) and morphed (b) configurations of the trailing edge due to the bi-stable laminate presented by Kuder et al. (2016) [5].

Such a system may seem too disruptive for current aerostructure design, hence simpler systems have been recently studied by Airbus [28], where control surfaces can be actuated using the same snap-through behaviour called the Superelastic Monostable Spoiler (SMS). Castrichini et al. (2024) [29] presented a preliminary study of such a system for dynamic load reduction. One critical observation of this study was the retraction of the spoiler must be slow, to avoid any self-induced vibration of the structure. This concept is still in a relatively early stage and has theoretical standing, hence practical analysis of such a system is still required.

Slightly more dedicated GLA systems have also been researched, such as the passive-twist wing tip (PTWT) presented by Guo et al. (2012) [30] and further applied in large aircraft models [31]. The passive-twist wing tip works as a separate wing segment at the end of the primary wing. The PTWT is connected using a shaft and a torque spring. The shaft being in front of the aerodynamic centre, causes the PTWT to go *nose-down* when acted on by a gust load. While the torque spring is stiff enough to keep the required angle-of-attack (AoA) under 1g cruise loads, the main advantage of passive systems comes from their reliability and the lack of any dependence on any underlying sub-systems.

2 State of the Art

This chapter presents a more theoretically detailed insight into the flared folding wing tip (FFWT) concept. The chapter introduces the importance of wing aspect ratio, followed by a brief introduction of related concepts that have been developed and used to improve aircraft efficiency. The major aerodynamic force opposing the flight direction is *drag*. *Induced drag* is a component of drag arising from the three-dimensional effects of the flow interacting with the shape of the wing. Lift on a wing can be attributed to the difference in pressure between the upper and lower surface of the wing with the lower surface having higher pressure. However, with a finite wing, the high-pressure air starts to flow upwards to the lower-pressure region, developing wing tip vortices. This creates a downwash effect behind the wing increasing the local angle of attack and developing another force acting downstream. This induced drag is defined using a non-dimensional coefficient which can be mathematically represented as:

$$C_{d_i} = \frac{C_l^2}{\pi \, \mathrm{AR} \, e} \tag{2.1}$$

Where C_l is the coefficient of lift, AR represents the aspect ratio of the wing and, e gives the efficiency factor which is based on the shape of the wing. The AR is the ratio between the square of the span and the wing area, hence the C_{d_i} is inversely proportional to the square of the span. Winglets help increase the effective span of the wing, which results in reduced induced drag, the effect of which however is not as pronounced as elongating the wing. However, longer wings change the gate class for commercial planes which increases gate charges incurred by airlines. Furthermore, longer wings need to be well secured from the wing root to handle larger deformation and loads.

Variable wing geometries offer solutions for achieving longer wings during flight while still allowing them to be stowed on the ground. For instance, the *Wright Flyer* employed wing warping to control roll, and the Bell X-5, developed from the Messerschmitt P.1101 (which featured a ground-adjustable variable-sweep wing), was later enhanced by Bell Aircraft Works in the US to enable in-flight wing sweep variation [32]. This evolution ultimately led to designs such as the F14 Tomcat, famous for its variable wing sweep, which facilitated storage on aircraft carriers and inspired modern concepts like the Boeing 777x.

In addition to these storage and control benefits, morphing wings have been conceptualised to mimic bird-like wing movements, thereby offering aerodynamic advantages, particularly in reducing induced drag. Projects such as the SmartX Wing [33] employ a modular Translation Induced Camber (TRIC) morphing method that combines wing warping and skin bending to dynamically adjust the wing's camber and twist. By actively optimizing the wing shape during flight, these morphing techniques can improve the lift distribution along the span, effectively reducing induced drag. Morphing wings of this kind, however, are still in their nascent phase and will require further research and development before being adopted into commercial designs.

Therefore, the concept of folding wing tips has been in the aerospace industry for a long time. One of the earliest uses of a hinge-based wing mechanism can even be dated back to 1922 when Juan de la Cierva developed a rotorcraft called the Autogyro C3. The aircraft was designed with a five-blade rigid rotor, which caused the aircraft to fall sideways. As a response to this issue, de la Cierva incorporated a hinge at the root of the blades eliminating rolling moments in forward flight [34]. Although de la Cierva's designs paved the way for the modern helicopter, the use of folding mechanisms for aeroplane wings came later.

The bio-inspired design of folding wing tips, intended for in-flight deployment on commercial aircraft, is derived from the Albatross seabird. Airbus' *AlbatrossONE* project initially tested this concept on a small-scale demonstrator [35]. Building on these findings, Airbus is now advancing the technology by integrating and testing it on a modified Cessna Citation VII demonstrator as part of the *Extra Performance*

Wing program. This larger-scale testing aims to assess the aerodynamic benefits, structural dynamics, and overall feasibility of adaptive wing technologies in real-world flight conditions [36].

2.1. The Flared Folding Wing Tip (FFWT)

The folding wing tip concept as a loads alleviation device was initially tested and introduced by Airbus around 2004 [37] which initiated a multi-institutional effort to further understand the use of this device. Wilson et al. (2017) [38] then patented a much more developed design of the system for dynamic load alleviation.

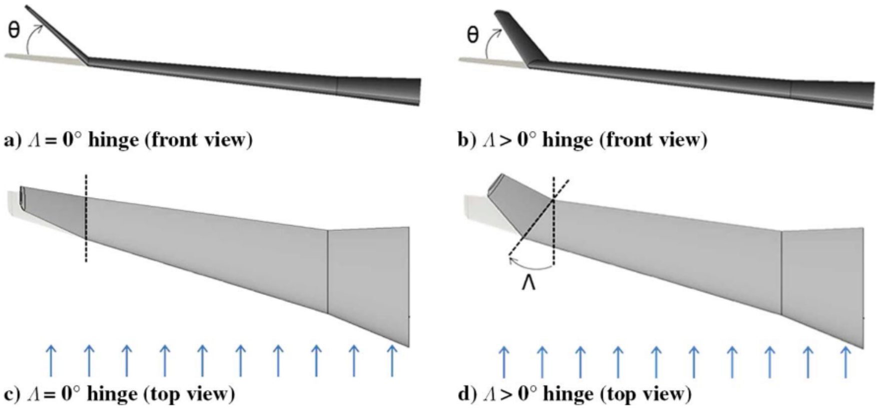

Figure 2.1: The FFWT Concept [6]

Figure 2.1 can be used to understand the different parameters of the FFWT. The *flare-angle* is represented by Λ, which is the angle between the hinge axis and the free-stream flow. Upon release, the wing tip is allowed to rotate freely about the hinge axis achieving a *fold-angle*, denoted by θ. The concept of the flare is introduced to reduce the local angle of attack (AoA), and with an assumption of small deflections, the variation of this angle of attack, $\Delta\alpha$, can be defined using:

$$\Delta\alpha = -\arctan(\tan\theta\sin\Lambda) \tag{2.2}$$

Once the gust passes, and the loading goes back to $1g$, the wing tip would realise its original position. Several studies have since studied the concept including low-fidelity models to experimental tests. The fidelity of the models varies in both the structural formulation, where reduced order models based on linear assumptions were initially used for preliminary studies. The incorporation of non-linearities and dynamic behaviours has further been augmented to improve the accuracy of these models. On the other hand, the aerodynamic models also contribute to the accuracy of the whole model. The simplest aerodynamic model is the strip model, which neglects 3D aerodynamic effects and is followed by panel methods such as vortex and doublet lattice methods which are relatively higher fidelity models. More complex fluid-structure interaction formulations are used wherein flexible multi-body formulations are coupled with computational fluid dynamics (CFD). Some of these studies will be presented in the following section.

The preliminary study performed by Castrichini et al. (2017) [6] used the FFAST aeroelastic model which is a stick model of a representative civil airliner with a lumped mass assumption. This model is coupled with a DLM aerodynamic model. The drawbacks of the low fidelity are discussed by the authors, however, it must be noted that the use of a simple model reduces computational efforts and hence allows the authors to present a thorough study of the concept. The paper discusses four analyses: a static trim solution, flutter analyses, a 1−cosine gust response and a continuous gust response. Different configurations were modelled based on two different masses of the wing tip (100kg and 943kg), as well as the flare angle, where a 0^o and 25^o flare angle were compared to a baseline model with no folding wing tip. It was observed that the higher mass of the wing was detrimental to load alleviation since the inertia of the system increased too much to have significant rotations. From the static solution, it was observed that with a 25^o flare angle and a heavier wing tip, a coupling between the first wing bending mode interacted with the wing tip first mode, while the lighter wing tip showed heavily damped results. The same trend of results was seen in the other analyses, nevertheless, an overall benefit of the FFWT was realised. However, it must be noted that this was one of the first studies and employed a very low-fidelity model.

Non-linear models were studied to understand the effects of the FFWT further. Building up the last paper, a non-linear stiffness hinge was incorporated into the FFAST (Future Fast Aeroelastic Simulation Technologies) model [39]. However, this model used a commercial multi-body code to incorporate the floating frame of reference (FFR) method to improve the dynamic description of the wing tip. The FFR technique essentially uses two sets of coordinates, namely *the reference coordinates* to describe the location and orientation of a body reference and *the elastic coordinates* which describes the deformation with respect to the body reference frame. This is done using techniques such as Rayleigh-Ritz methods, which essentially limit the modelling of the system to small and linear deformations. One critical feature of this model was the use of variable stiffness to describe the hinge moment, this was done only to allow movement of the wing tip when a high enough aerodynamic load was acting on the system. This was implemented using a piecewise function for the nonlinear hinge moment,

$$\begin{aligned} &M_{NL} = -K_\theta \theta \\ &\text{where,} \\ &K_\theta = \begin{cases} 1.0E^{12}\,\text{Nm/rad} & \text{if } K_\theta\theta \le M_{\max} \text{ and } 0 < t < t_{\text{release}} \\ 1.0E^{0}\,\text{Nm/rad} & \text{if } K_\theta\theta > M_{\max} \text{ and } t \ge t_{\text{release}} \end{cases} \end{aligned} \tag{2.3}$$

This study realises the importance of the speed of the FFWT response, hence a high moment threshold ($M_{\max}$) can be detrimental to the desired effect. Hence it was found that lower values of the threshold combined with low hinge damping provided rapid response leading to WRBM lower than the baseline model. The experimental results further reinforce these findings. The experimental tests also considered the delays during the actuation of the hinge, which resulted in an unwanted increase in the release threshold. Hence, for shorter gusts, a reduction in load alleviation was recorded. Furthermore, a critical observation of the study points to the increase in loads and instability if the hinge is released closer to the peak load. Such a non-linear phenomenon cannot be modelled using steady linear solvers. Basic panel methods also cannot model such behaviour; the incompatibility of DLM, for example, is highlighted in a study by Cheung et al. (2018) [40], which concluded that the lack of non-linearity of the DLM model restricts it from modelling large deflections and rotations of lift surfaces.

Different methods have been used to incorporate non-linearities to analyse the FFWT concept. Two main methods, albeit similar, are the geometrically exact representation of effective angle of attack introduced by Healy et al. [7]. The other proponent is the multibody formulation used in SHARPy [1]. Both of these methods are delineated in the following subsections.

2.1.1. Geometrically Exact Representation of Effective Angle of Attack

Conti et al. (2021) [41] introduced a non-linear aeroelastic formulation to model the larger deformation. The multi-body formulation presented in this study assumes that the FFWTs are rigid bodies undergoing no local deformation relative to the displacement of the tip from the hinge. The main structure, however, is modelled using a set of mode shapes and is modelled as a linear flexible body. While the translations,

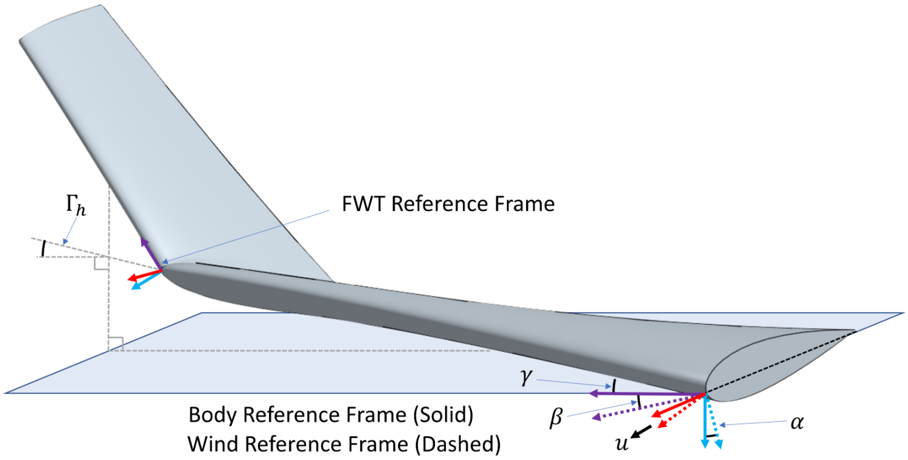

Figure 2.2: The reference system as described by Healy et al. (2022) [7]

u_h and the rotations θ_h are in the form of summations of the product between modal shapes and modal coordinates, the description of the FFWT must be understood. The model defines the centre of gravity, z_g, of the FFWT from the undeformed reference with a unit vector i defining the FFWT's orientation.

$$z_g = x_h + u_h + r_g \tag{2.4}$$

$$i = i_0 + \theta_h \times i_0 \tag{2.5}$$

Where r_g is the position vector of the FFWT with respect to the hinge, and i_0 defines the undeformed configuration. i_0 is used here to define the orientation in the undeformed configuration. The absolute velocity, angular velocity, and absolute acceleration are derived from this. The equations of motions derived from this description are then transformed into generalized coordinates and coupled with the doublet lattice method (DLM). However, in this aerodynamic model, generalized aerodynamic forces (GAF) matrices are calculated, which are aerodynamic loads based on the generalized structural displacements. The study ultimately shows that for a static calculation, the inclusion of non-linearity in the geometry only adds incremental changes from a linear model. However, due to the use of quasi-steady assumptions, dynamic effects cannot be completely captured.

Taking inspiration from the model presented by Conti et al. (2021) [41], another model was developed by Healy et al. (2022) [7] to further capture the nonlinear dynamics of the FFWT specifically. This model is created using a Lagrangian coordinate approach [42], where a set of transformation matrices are used to describe the aircraft velocity vector from a reference frame centred about the FFWT. Three reference frames as described are shown in Figure 2.2.

A set of rotation matrices is used to define the body reference frame from the wind frame.

$$\mathbf{H}_b^w = \mathbf{R}_z(\beta)\mathbf{R}_y(\alpha) \tag{2.6}$$

Further, another transformation matrix defining the FFWT reference frame from the body reference frame is calculated by,

$$\mathbf{H}_t^b = \mathbf{R}_x(\Gamma_h)\mathbf{R}_z(\Lambda)\mathbf{R}_x(\theta)\mathbf{R}_z(\gamma - \Lambda) \tag{2.7}$$

Hence to define the aircraft velocity in the FFWT reference frame the following formulation can be used,

$$\vec{\mathbf{v}}_t = \left[v_{t1}\ v_{t2}\ v_{t3}\right]^T = (\mathbf{H}_b^w \mathbf{H}_t^b)\vec{\mathbf{v}}_w = (\mathbf{H}_t^w)\vec{\mathbf{v}}_w \tag{2.8}$$

This formulation can be used to describe a *rigid* FFWT and the local AoA and the sweep angle of the FFWT can be found. The critical advantage of parametrically studying these components allows better analysis of the different non-linear coupling mechanisms identified for the FFWT concept.

2.1.2. SHARPy Implementation of the FFWT [1]

A similar theoretical concept is further implemented into *SHARPy*, which is a non-linear aeroelastic analysis software [43]. SHARPy, envisioned as a general case aeroelastic solver, defines the multibody framework in a more general way allowing its user to test different configurations. Furthermore, in this formulation the dependency of the hinge line vector as a function of time is eliminated by defining its projection in two local frames, the main body frame and the wing tip frame as shown in Figure 2.3.

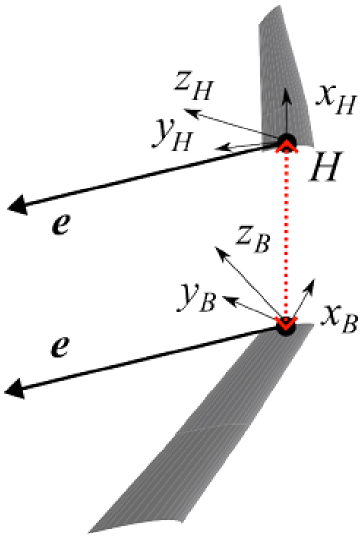

Figure 2.3: Reference Axes used for Wing Tip by Cheng et al. (2024) [1]

Furthermore, the formulation makes use of holonomic and non-holonomic constraints to define the connections between different nodal DOFs. To augment these constraints, Cheng et al. [1] (2024) use Lagrange multipliers and hence define an augmented Lagrangian which is further explained in Subsection 3.1.2.

$$\begin{cases} \mathbf{M}(q)\ddot{q} + \mathbf{B}_h^T(q,t)\lambda_h + \mathbf{B}_n^T(\dot{q},t)\dot{\lambda}_n = \mathbf{Q}(q,\dot{q},t), \\ \mathbf{g}_h(q,t) = 0, \\ \mathbf{g}_n(q,\dot{q},t) = \mathbf{B}_n(q,t)\cdot\dot{q} + \mathbf{g}_{n_0} = 0 \end{cases} \tag{2.9}$$

Here, $\mathbf{M}$ is the mass matrix, $\mathbf{Q}$ is the matrix containing all the forces and $\mathbf{B_h}$ and $\mathbf{B_n}$ are the Jacobians of the holonomic and non-holonomic constraints. These matrices are functions of the generalised displacements, q, and their derivatives. When Equation 2.9 is put into matrix form, the tangent stiffness ($\mathbf{K}^t$) and damping ($\mathbf{C}^t$) matrices also appear with the constraint matrices as their part,

$$\begin{bmatrix} \mathbf{M} & 0 & 0 \\ 0 & 0 & 0 \\ 0 & 0 & 0 \end{bmatrix} \begin{pmatrix} \Delta\ddot{q} \\ \Delta\ddot{\lambda}_h \\ \Delta\ddot{\lambda}_n \end{pmatrix} + \begin{bmatrix} \mathbf{C}^t & 0 & \mathbf{B_n}^T \\ 0 & 0 & 0 \\ \mathbf{B_n} & 0 & 0 \end{bmatrix} \begin{pmatrix} \Delta\dot{q} \\ 0 \\ \Delta\dot{\lambda}_n \end{pmatrix} + \begin{bmatrix} \mathbf{K}^t & \mathbf{B_h}^T & 0 \\ \mathbf{B_h} & 0 & 0 \\ 0 & 0 & 0 \end{bmatrix} \begin{pmatrix} \Delta q \\ \Delta\lambda_h \\ 0 \end{pmatrix} = \begin{pmatrix} r^o \\ -g_h^o \\ -g_n^o \end{pmatrix} \tag{2.10}$$

Cheng et al. (2024) then use the Newmark-β method to solve for the system. The tangent stiffness and damping terms are functions of the constraints and are given by Equation 2.11.

$$\begin{cases} \mathbf{C}^t = \frac{\partial \mathbf{B_n}^T \dot{\lambda}_n}{\partial \dot{q}} - \frac{\partial \mathbf{Q}}{\partial \dot{q}}, \\ \mathbf{K}^t = \frac{\mathbf{M}\ddot{q}}{\partial q} + \frac{\mathbf{B}_h^T \lambda_h}{\partial q} - \frac{\partial \mathbf{Q}}{\partial q} \end{cases} \tag{2.11}$$

Hence the constraint equations are derived and sequentially the above terms can be formed. Cheng et al. (2024) further verify the model by developing a rigid body model of a flared double pendulum case and comparing it to a NASTRAN model. It was found that the deviations only occur upon the second swing of the pendulum, as the system gets more chaotic, however, the overall pattern was observed to be similar. A closer agreement between the NASTRAN solution was observed by reducing the rigidity.

2.2. Aerodynamic Modelling

The most basic implementation of an aerodynamic model is through *strip theory*. The main drawback of this model is that 3D effects of the flow are not fully captured, such as the effect of vortices [44]. The wing is discretized by a finite number of spanwise strips and the lift is calculated using Theodorsen's aerodynamic theory. Lift and resulting moments are split into circulatory and non-circulatory parts. Based on the time discretization required by the analysis a steady, quasi-steady or an unsteady form of the model can be used for the analysis. A quasi-steady strip theory with adaptations for the FFWT was employed by Corcoles et al. (2023) [45]. However, it was noted that the model deviated from the experimental results due to the lack of accuracy when modelling dynamic response under unsteady conditions due to the quasi-steady assumptions. Healy et al. (2024) [46] developed such a model that utilised an unsteady strip theory, and to further incorporate 3D effects, lift curves were interpolated from calculations done using lifting line theory. There was good agreement between the experimental and numerical models for their model. However, one concern of such a model lies in its applicability to other geometries and problems, hence for each new issue, it will be required to perform all the interpolations again.

There are several approaches to modelling the flow around the structure. Computational Fluid Dynamics (CFD) is one method and an aeroelastic analysis of the FFWT has been conducted by Valente et al. [47]. Due to the computationally heavy nature of CFD models, they cannot be adopted for parametric studies, optimization problems or preliminary design explorations. Hence, studies of the FFWT have mainly adopted panel methods. Panel methods are numerical methods based on *potential flow theory*, wherein the flow is considered irrotational and incompressible, and satisfies the Laplace equation [48].

$$\nabla^2 \Phi^* = 0 \tag{2.12}$$

Where Φ^* is the total velocity potential and its gradient ($\nabla\Phi$) leads back to the velocity vector. The Laplace equation is essentially developed from placing the irrotational assumption on the incompressible continuity equation [48].

Singularity solutions are one of the most common ways to approach incompressible and irrotational problems. Three main singular elements can be used to represent flow around a body: source, doublets, and vortices. Elements can be picked depending on the type of problem and analysis [48]. The most widely used method for capturing the unsteady effects of the flow is the doublet lattice method (DLM).

Much of the studies presented in reference to the FFWT [39, 40, 49] were performed using this method. DLM operates in the frequency domain, and hence a solution must be found for a range of frequencies, and the aerodynamic influence coefficient matrix must be formed for each of these frequencies, which can be highly computationally extensive. Furthermore, another major drawback of this method lies in the definition of the panel's normal, which only acts perpendicular to the panel from its initial state, hence its applicability to small deflections. Steady Vortex Lattice Method on the other hand can be considered simple since it assumes steady and inviscid flow. To account for unsteady effects, an augmented VLM model is used *unsteady vortex lattice method (UVLM)*. A study presented by Cheung et al. (2018) [50] compared DLM with UVLM, and it was noticed that DLM over-predicted the GLA due to the FFWT, this was mainly a result of DLM not being able to capture the coupling of the bending mode of the main wing with the pitching mode of the FFWT, leading to an inaccurate aerodynamic stiffness of the FFWT. UVLM has been used in SHARPy [43], and hence also used by Cheng et al. (2024) [1] for the analysis of the FFWT.

2.3. Research Objective

The literature review highlights an extensive knowledge base employing diverse strategies to analyse the Flared Folding Wing Tip (FFWT) concept. Among these, SHARPy [1, 43] is a recent implementation that integrates an Unsteady Vortex Lattice Method (UVLM) with a multi-body description of the FFWT. However, SHARPy primarily serves as an open-source analysis tool, with limited design optimization capabilities. On the other hand, PROTEUS not only facilitates aeroelastic analysis but also incorporates gradient-based optimization techniques, making it a more suitable platform for enhancing wing designs. Building on this capability the following research objective was framed:

> This study aims to extend the PROTEUS framework by incorporating hinge constraints into its existing representation of the wing. This involves augmenting the multibody formulation to analyse the static behaviour of the FFWT and expanding the dynamic framework to capture the effects of hinge release during gust encounters. Through these extensions, the study seeks to evaluate the FFWT concept via both static and dynamic analyses within the improved PROTEUS framework.

2.3.1. Research Questions

From the stated objective, the research questions are divided based on the static and dynamic behaviour of the FFWT as follows:

1. **Static Behaviour of the FFWT**
    - **Main Question:** How can the static behaviour of the Flared Folding Wing Tip be accurately captured using the in-house aeroelastic optimization framework?
    - **Sub-Question:**
        - How can the hinge axis be integrated into the existing co-rotational, non-linear static structural framework?
2. **Dynamic Behaviour of the FFWT**
    - **Main Question:** How can the dynamic module of PROTEUS be adapted to simulate a hinge-unlocking event in a wing with a Flared Folding Wing Tip?
    - **Sub-Questions:**
        - Can PROTEUS' dynamic solver capture the response of a Flared Folding Wing Tip (FFWT) with an unlocked hinge?
        - What modifications can be made to the existing dynamic formulation to transition from a locked to an unlocked hinge state?
        - How does the timing of the hinge release affect the wing's response during a gust encounter?

3 PROTEUS

PROTEUS is an in-house aeroelastic modelling and optimization framework based on the work of De Breuker (2011)[8]. Since its inception, several additions have been implemented to the framework making it more versatile. The work by Werter (2017)[51] stands out in its integration of a dynamic solver and the optimization framework. The following chapter lays down the crucial aspects of the structural and aerodynamic model used in PROTEUS. The following chapter is dedicated to giving a brief overview of the existing solver, including some key aspects such as the co-rotational framework and the Lagrange multiplier method.

3.1. Structural Solver

PROTEUS was developed to model the aeroelastic behaviour of slender morphing wings; hence, large deformations must be considered. Given the slenderness of wing structures, a stick model is used for the structural representation of the wing. Using the stick model helps reduce the degrees of freedom while providing sufficiently accurate results for analysis and optimization. The structure is reduced to a one-dimensional Timoshenko beam model by developing the Timoshenko cross-sectional stiffness matrix with the beam as the reference axis to embed the three-dimensional effects of composite laminates. The work of Werter (2017) also introduced the dynamic model expanding on the non-linear static model implemented by De Breuker (2011) [8].

3.1.1. Co-Rotational Framework

To incorporate non-linear effects into the system, PROTEUS uses a co-rotational framework, introduced by Battini & Pacoste (2002) [52]. This framework models the rigid displacements and incremental elastic deformations of beam elements to capture the large deformations and rotations. These rigid displacements are calculated with the aid of local reference frames which are attached to each element. Linear elastic analysis is done for each of these local element frames and their deformations account for the geometric non-linear behaviour.

To fully understand the framework, it is also essential to examine the implementation of the rotational formulation. De Breuker (2011) [8] adopts a *total rotation* parametrization instead of an *incremental rotation* approach due to reduced computational complexity. However, the total rotation formulation inherently limits the rotation magnitude to 2π. Despite this restriction, the rotations expected in the FFWT are not large enough for this limitation to be a concern.

Within this framework, rotations are represented using Rodrigues' rotation formula. Specifically, rotation matrices are expressed as the matrix exponential of their associated pseudo-vectorial representation, $\boldsymbol{\theta}_s$. This approach provides an efficient and consistent way to handle rotational transformations.

$$\mathcal{R} = \exp(\theta_s) \tag{3.1}$$

As discussed, rotations are performed in the element frame, whereas the structural solutions obtained in PROTEUS are referenced to the body-fixed frame. Figure 3.1 illustrates the different reference frames and their transformations. The initial element frame represents the undeformed state of the beam, with the first direction vector, $\mathbf{e_1^0}$, aligned along the beam. Once this primary direction is established, the third direction vector, $\mathbf{e_3^0}$, is defined to point in the global negative z-direction, and the second direction vector is then determined as the cross-product of the first and third vectors.

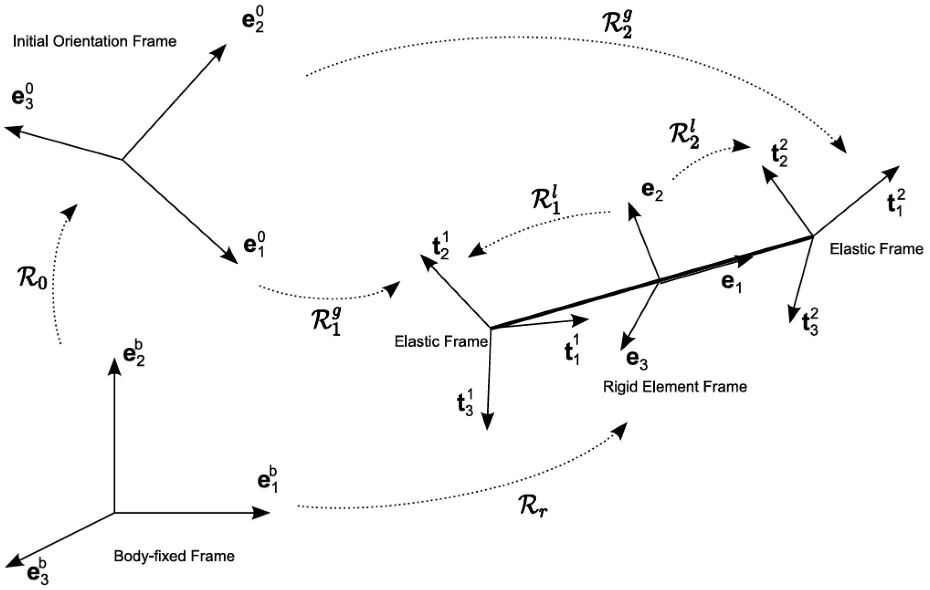

Figure 3.1: Involved Rotations in the Co-rotational framework [8]

Focusing on the transformations between, the body-fixed frame, the rigid element frame and the elastic frame as shown in Figure 3.1. $\mathcal{R}_0$ transform the boxy-fixed frame to the initial orientation frame for each node. Followed by $\mathcal{R}_1^g$ and $\mathcal{R}_2^g$ which are used to rotate the initial orientation frame to the deformed nodal elastic frame. These nodal frames are used later to define the joint constraints. Finally, these nodal triads indicated by $\mathbf{t}^1$ and $\mathbf{t}^2$ are used to develop the rigid beam element frame. Rotations $\mathcal{R}_1^l$ and $\mathcal{R}_2^l$ link the rigid beam element frame to its corresponding nodal triads. Lastly, in order to represent the rigid element frame in the body-fixed frame, the transformation matrix $\mathcal{R}_r$ is defined.

This co-rotational framework is used in conjunction with linear Timoshenko beam elements. De Breuker (2011) [8] used a 20-degree-of-freedom formulation to define the elements given in Figure 3.2.

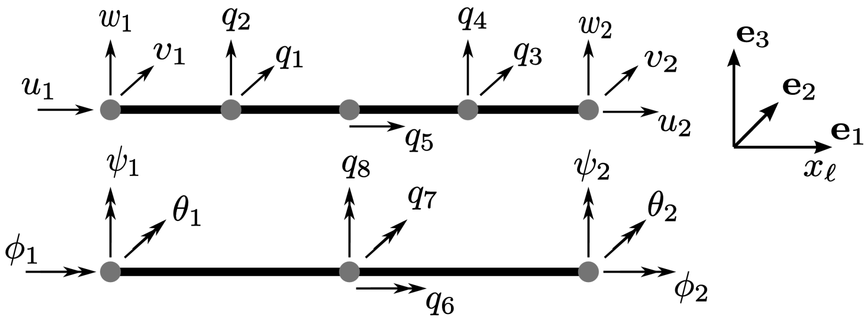

Figure 3.2: Element Degrees of Freedom [8]

Eight coefficients, q_1 to q_8, are parameters used for the quadratic or cubic bubble functions that enhance the performance of the shape functions. These functions avoid shear locking by introducing additional flexibility into the displacement field, improving bending behaviour and reducing artificial shear deformations. A reduced 12-degree-of-freedom description of a beam element is then obtained through Guyan reduction, ultimately leading to a final framework with six degrees of freedom for a node i: three displacement degrees of freedom, u_i, v_i, and w_i, and three rotational degrees of freedom, ψ_i, θ_i, and ϕ_i. This completes the definition of the discretisation and rotational framework used to capture deformations. With this foundation in place, the following subsection details the formulation of the non-linear solver for the multibody problem.

3.1.2. Lagrange Multiplier Method

The multibody formulation framework used in PROTEUS is based on the *Lagrange Multiplier Method*. This method transforms a constrained problem into an equivalent unconstrained form by introducing additional variables, known as Lagrange multipliers. Although this approach increases the number of unknowns, it ensures that the variables remain independent of each other, enabling a more flexible and systematic solution process [42, 53].

For a function $\mathcal{F} = \mathcal{F}(p_1, p_2, \ldots, p_n)$ that depends on a constraint $\Phi = \Phi(p_1, p_2, \ldots, p_n)$, the variations of $\mathcal{F}$ with respect to the variables p_i are not independent due to the constraint. To address this, the Lagrange Multiplier Method introduces an additional variable, λ, called the Lagrange multiplier. By forming a new function $\mathcal{L} = \mathcal{F} + \lambda\Phi$, the problem becomes one of solving a system of equations where variations in p_i and λ can be treated independently. Function, $\mathcal{L}$, must vanish under the condition for equilibrium giving Equation 3.2.

$$\frac{\partial \mathcal{F}}{\partial p_1}\delta p_1 + \ldots + \frac{\partial \mathcal{F}}{\partial p_n}\delta p_n + \lambda\left[\frac{\partial \Phi}{\partial p_1}\delta p_1 + \ldots + \frac{\partial \Phi}{\partial p_n}\delta p_n\right] = 0 \tag{3.2}$$

Further simplifying the equation gives:

$$\sum_{i=1}^{n}\left[\frac{\partial \mathcal{F}}{\partial p_i} + \lambda\frac{\partial \Phi}{\partial p_i}\right]\delta p_i = 0. \tag{3.3}$$

For a kinematic problem, the function, $\mathcal{F}$, takes the form of the system's total energy. Assuming a kinematic configuration with n components, the strain energy of the system can be described by the formulation presented by Géradin [42]:

$$\mathcal{W} = \frac{l_0}{2}\int_0^1 \epsilon^T C \epsilon d\xi \tag{3.4}$$

Where, ϵ is the strain vector, and C is the cross-sectional stiffness tensor. Addressing the equation as a minimization problem, Equation 3.5 is obtained, where $\mathbf{p}$ represents the degrees of freedom (DoFs), $\mathbf{e}(\mathbf{p})$ is the vector of generalized strains, and $\mathbf{K}$ is the stiffness matrix.

$$\min_{\mathbf{p}} \mathcal{W} = \frac{\mathbf{1}}{\mathbf{2}}\mathbf{e}(\mathbf{p})^{\mathbf{T}}\mathbf{K}\mathbf{e}(\mathbf{p}) \tag{3.5}$$

With constraint: $\Phi(\mathbf{p}) = 0$, the problem can be transformed to an equivalent unconstrained problem following Equation 3.3. The minimization problem hence becomes:

$$\min_{\mathbf{p},\lambda} \frac{\mathbf{1}}{\mathbf{2}}\mathbf{e}(\mathbf{p})^{\mathbf{T}}\mathbf{K}\mathbf{e}(\mathbf{p}) + \lambda^T\Phi(\mathbf{p}) \tag{3.6}$$

The stationary point of the above function can then be expressed as:

$$\begin{cases} \delta\mathbf{p}^T(\mathbf{E}^{\mathbf{T}}\mathbf{K}\mathbf{e} + \mathbf{B}^{\mathbf{T}}\lambda) = 0 \\ \delta\lambda^{\mathbf{T}}\Phi = 0 \end{cases} \tag{3.7}$$

Here, $\mathbf{E} = \frac{\partial \mathbf{e}}{\partial \mathbf{p}}$ is the strain matrix of the system, and $\mathbf{B} = \frac{\partial \Phi}{\partial \mathbf{p}}$ is the gradient matrix of the constraints. These equations give a set of non-linear equations, assuming $\delta\mathbf{p}$ is arbitrary. Linearising the problem by assuming an approximate solution $\mathbf{p}^*$ and λ^*.

$$\begin{aligned} \mathbf{p} &= \mathbf{p}^* + \Delta\mathbf{p} \\ \lambda &= \lambda^* + \Delta\lambda \end{aligned} \tag{3.8}$$

The tangent stiffness matrix $\mathbf{K}_T$ is found upon linearising Equation 3.7.

$$\boldsymbol{K}_T = \frac{\partial}{\partial p}(\mathbf{E}^\mathbf{T}\mathbf{Ke}) = \mathbf{E}^\mathbf{T}\mathbf{Ke} + \frac{\partial \mathbf{E}}{\partial p}(\mathbf{Ke}) \tag{3.9}$$

Finally, to solve for the static equilibrium, Equation 3.7, and Equation 3.9 can be incorporated to form Equation 3.10 which represents the linear set of equations in residual form:

$$\begin{bmatrix} \mathbf{K_T} & \mathbf{B^T} \\ \mathbf{B} & 0 \end{bmatrix} \begin{bmatrix} \Delta\mathbf{p} \\ \Delta\lambda \end{bmatrix} = \begin{bmatrix} r(\mathbf{p}^*) \\ -\Phi(\lambda^*) \end{bmatrix} \tag{3.10}$$

Here $r(\mathbf{p}^*)$ and $-\Phi(\lambda^*)$ represent the residual forces associated with the degrees of freedom and the Lagrange multipliers, respectively, based on their approximate solutions. To solve for static equilibrium in the presence of geometric and boundary condition-based non-linearities, an iterative approach is required. The next section outlines the solution strategy employed by PROTEUS to handle these non-linear effects and determine equilibrium configurations efficiently.

3.1.3. Static Non-Linear Solver

Structural equilibrium is defined when the internal forces are equal to the applied external forces. Non-linear behaviour for a structure may root from the structure's geometry, the boundary conditions, or the material. In dynamics, damping terms, as well as inertial and vibrational effects, can induce non-linear behaviour. PROTEUS assumes no material non-linearities, however, for static conditions, geometric non-linearities based on large displacements, and boundary condition-based non-linearities can be modelled.

$$\mathbf{F_s}(\mathbf{p}) = \mathbf{F_{ext}}(\mathbf{p}) \tag{3.11}$$

The forces in the structure depend on its degrees of freedom, represented by its displacements and rotations, henceforth denoted as $\mathbf{p}$. Equation 3.11 equates the internal forces ($\mathbf{F_s}$) with the external forces ($\mathbf{F_{ext}}$ to describe the structural equilibrium. To incorporate non-linear behaviour, PROTEUS divides the solution over incremental load steps. This is defined by a loading parameter, γ, ranging from 0 to 1.

$$\mathbf{F_s}(\mathbf{p}) = \gamma\mathbf{F_{ext}}(\mathbf{p}) \tag{3.12}$$

Equation 3.12 is then solved using the Newton-Raphson root-finding method. This method works by guessing the displacements and the Lagrange multipliers for which the equilibrium is satisfied. The residual vector for each estimated solution then becomes the difference between the internal force and the load-factored external force, which should be 0 at equilibrium.

3.1.4. Dynamic Solver Extension

The non-linear static structural solution provides a solution in which the system is in a state of equilibrium, satisfying Equation 3.11. Assuming small displacements, $\Delta\mathbf{p}$, Equation 3.11 can be expanded to give the linearised static equilibrium equation Equation 3.13.

$$\mathbf{F}_{\mathbf{s_0}} + \mathbf{K}_{\mathbf{s_0}}\Delta\mathbf{p} = \mathbf{F}_{\text{ext}_0} + \mathbf{K}_{\text{ext}_0}\Delta\mathbf{p} \tag{3.13}$$

Using the static equilibrium condition as prescribed in Equation 3.11, the following equation is formed,

$$\mathbf{K}_{\mathbf{s_0}}\,\Delta\mathbf{p} = \mathbf{K}_{\text{ext}_0}\,\Delta\mathbf{p}. \tag{3.14}$$

Here, $\mathbf{F}_{\mathbf{s_0}}$ is the initial internal force vector, $\mathbf{K}_{\mathbf{s_0}}$ is the initial stiffness matrix of the system, $\mathbf{F}_{\text{ext}_0}$ is the initial external force vector, $\mathbf{K}_{\text{ext}_0}$ is the initial stiffness matrix of the external load system, $\Delta\mathbf{p}$ is the displacement vector.

In PROTEUS, to transition from the static to the dynamic formulation, a mass matrix is augmented to capture the inertia of the beam elements. This mass matrix is formed from the mass matrix of the deformed static equilibrium configuration. The kinetic energy of a structure is given by the following equation:

$$\mathcal{T} = \frac{1}{2}\int_V \rho\mathbf{v}^{\mathbf{T}}\mathbf{v}\,dV \tag{3.15}$$

Where the integral of the mass density, ρ times the local velocity vector, $\mathbf{v}$, squared is calculated. This velocity can be written considering velocity $\dot{\mathbf{u}}$ and angular velocity, as:

$$\mathbf{v} = \dot{\mathbf{u}} + \dot{\theta}_{\mathbf{s}} \times \mathbf{r} \tag{3.16}$$

With $\mathbf{r}$ as the distance vector of a location in the wing with respect to the beam element axis. Further expanding Equation 3.15 using Equation 3.16 and the beam's cross-sectional properties and writing in terms of the local degrees of freedom:

$$\mathcal{T} = \frac{L}{2}\int_0^1 mA\dot{\mathbf{u}}\cdot\dot{\mathbf{u}} + 2\dot{\mathbf{u}}^{\mathrm{T}}m\mathbf{Q}\dot{\boldsymbol{\theta}} + \dot{\boldsymbol{\theta}}^{\mathrm{T}}m\mathbf{I}\dot{\boldsymbol{\theta}}\,d\xi \tag{3.17}$$

Which gives three mass components, with mA giving the mass per unit length, **mQ** the mass moments per unit length and finally **mI** which gives the mass inertia tensor with respect to the beam element axis. Based on the formulation of Werter (2017) [51], the shape functions are introduced and the mass matrix is calculated by computing the Hessian of the kinetic energy. Finally, the local mass matrix is transformed from the local beam element reference system to the global body-fixed reference system to get **M**. Writing the dynamic equation of motion:

$$\mathbf{M}\Delta\ddot{\mathbf{p}} + \mathbf{C}\Delta\dot{\mathbf{p}} + \mathbf{K}_{\mathbf{s_0}}\,\Delta\mathbf{p} + \mathbf{B}\lambda = \mathbf{K}_{\text{ext}_0}\,\Delta\mathbf{p} \tag{3.18}$$

Finally, in order to develop the state space system, a QR decomposition is performed to incorporate the Lagrange multipliers since they appear implicitly in Equation 3.18, and is further elaborated in Section A.1.

3.2. Aerodynamic Solver

The aerodynamic solver employed in PROTEUS is a continuous-time formulation of the unsteady vortex lattice method (UVLM). Since this is a panel method, the flow field is globally described by small panels, which are expressed based on vortex rings. Each panel is defined with a vortex ring made of four vortex filaments. Furthermore, in order to improve the accuracy of the lift distribution, a half-cosine spanwise mesh distribution approach is used, hence there are more panels near the wing tip. The mesh is deformed with a set of rotation matrices based on the structural deformation. This is achieved by applying the rotations to the chord vector.

3.2.1. Wake Definition

The wake is modelled as a rigid surface connected to the wing's trailing edge. The advection equation can then be used to define the transport of vorticity onto the wake surface.

$$\frac{\partial \Delta\phi}{\partial t} + \mathbf{V_w} \cdot \nabla\Delta\phi = 0 \tag{3.19}$$

Here $\Delta\phi$ represents the jump in the velocity potential, and $\mathbf{V_w}$ is the wake velocity. Following the small perturbation theory, it can be assumed that the wake is convected with the free-stream velocity, allowing the assumption that the local wake velocity is equal to the free-stream velocity, $\mathbf{V}_\infty$.

$$\frac{\partial \Delta\phi}{\partial t} + \mathbf{V}_\infty \cdot \nabla\Delta\phi = 0. \tag{3.20}$$

For a static case, the Kutta condition can be applied wherein it is assumed that the flow leaves the wing smoothly, this can be expressed mathematically as:

$$\Delta\phi_b|_{TE} = \Delta\phi_w|_{TE}, \tag{3.21}$$

where $\Delta\phi_b$ and $\Delta\phi_w$ are the velocity potential differences of the wing-body and the wake respectively, along the same streamline.

3.2.2. Static Aerodynamic Solution

As aforementioned, the vortex strength distribution in the wake is constant in the flow direction, hence the semi-infinite wake solution is used. The following system of equations is generated based on the Kutta condition and the flow-tangency condition:

$$\mathbf{K_{st}}\mathbf{\Gamma_b} = -\mathbf{V}_\infty \cdot \mathbf{n_p} \tag{3.22}$$

Where $\mathbf{K_{st}}$ contains the influence coefficients of the wing and the semi-infinite wake, and Γ_b represents the vortex strength. The values of Γ_b are determined and subsequently substituted into equations derived from the Kutta-Joukowski theorem to compute the steady and unsteady aerodynamic forces and moments.

3.2.3. Aerodynamic State-space Formulation

Unlike the steady solution, the wake changes over time under dynamic conditions. To account for this transport of the wake, the steady aerodynamic solver must be altered and extended. Consequently, the wake must also be discretized. This is done using the discontinuous Galerkin method to discretize the advection equation. The aerodynamic state space equation is hence developed taking into account the Kutta condition, the flow tangency equation and the vorticity transport in the wake, giving:

$$\dot{\Gamma} = \mathbf{K_1}\Gamma_\mathbf{w} + \mathbf{K_2}\alpha + \mathbf{K_3} \tag{3.23}$$

Where Γ_w denotes the wake vortex strength, and α represents the increment in the angle of attack of the wing surface. The corresponding transfer matrices $\mathbf{K_1}$ and $\mathbf{K_2}$ give the contributions from the wake and the change in the angle of attack, respectively. Additionally, $\mathbf{K_3}$ represents the contribution of wing motion, which is incorporated using Equation 3.24.

$$\alpha = \alpha_{\text{air}} + \theta_t - \frac{\dot{h}}{V_\infty} + \frac{\dot{\theta}_t(x - x_b)}{V_\infty} \tag{3.24}$$

In this formulation, the angle of attack induced by the free-stream flow is captured by α_{air}, while θ_t represents the contribution due to wing twist. The last two terms account for the local heave motion and the local pitch rate of the wing, respectively. The local pitch rate is defined by the distance between the aerodynamic panel location and the pitch axis of the wing, $x - x_b$. Based on this formulation, the contribution of wing motion ($\mathbf{K_{10}}$) is incorporated into the aerodynamic input through the ($\mathbf{B_{ss}}$) matrix in Equation 3.26.

In order to define the aerodynamic output system given in Equation 3.25, the aerodynamic forces and moments are related to the state vector and the input. The vortex strengths of the wing and the wake contained within $\Gamma_\mathbf{w}$ are related using $\mathbf{L_1}$. Followed by the contribution of the free stream flow modelled with the induced angle of attack (α) and the time rate of change of the angle of attack ($\dot{\alpha}$), which are related to the aerodynamic forces and moments using matrices $\mathbf{L_2}$ and $\mathbf{L_3}$. Lastly, the motion of the wing is related using $\mathbf{L_4}$.

$$\begin{pmatrix} \mathbf{F} \\ \mathbf{M} \end{pmatrix} = \mathbf{L_1}\Gamma_\mathbf{w} + \mathbf{L_2}\alpha + \mathbf{L_3}\dot{\alpha} + \mathbf{L_4} \tag{3.25}$$

Putting Equation 3.23 and Equation 3.25 together, the aerodynamic state-space equation can be written as:

$$\dot{x} = \underbrace{\begin{bmatrix} \mathbf{K}_1 & \mathbf{K}_2 \\ 0 & 0 \end{bmatrix}}_{\mathbf{A_{ss}}} x + \underbrace{\begin{bmatrix} 0 & \mathbf{K}_3 \\ \mathbf{I} & 0 \end{bmatrix}}_{\mathbf{B_{ss}}} u \tag{3.26}$$

$$y = \underbrace{\begin{bmatrix} \mathbf{L}_1 & \mathbf{L}_3 \end{bmatrix}}_{\mathbf{C_{ss}}} x + \underbrace{\begin{bmatrix} \mathbf{L}_2 & \mathbf{L}_4 \end{bmatrix}}_{\mathbf{D_{ss}}} u \tag{3.27}$$

Where the input, $\mathbf{u}$, can be identified as $\begin{pmatrix} \dot{\alpha} & 1 \end{pmatrix}^T$, with $\mathbf{B_{ss}}$ being the corresponding input matrix. While, x is the state vector containing the wake vortex strength,Γ_w and the angle of attack (α) arranged as $\begin{pmatrix} \Gamma_w & \alpha \end{pmatrix}^T$. $\mathbf{A_{ss}}$ is the corresponding state matrix. Since, y, corresponds to the output equation, it's a vector containing the aerodynamic forces and moments from Equation 3.25. The right-hand side of the output equation hence resolves the state outputs using matrices $\mathbf{C_{ss}}$ which is the output matrix and $\mathbf{D_{ss}}$ is the feedthrough matrix.

3.3. Coupling

In order to solve the coupled system, unsteady aerodynamic forces need to be imposed on the structural nodes. Similarly, the increment of the angle of attack and its derivative formed due to the structural deformations need to be input into the unsteady aerodynamic system. The aerodynamic state space system has been introduced in Subsection 3.2.3. Furthermore, to incorporate the dynamic perturbation of the angle of attack due to the twist, Werter (2017) [51] defines the local angle of attack as:

$$\alpha_l = \underbrace{\alpha_0}_{\text{static equilibrium}} + \underbrace{\frac{\partial \alpha_l}{\partial \theta_s}\Delta\theta_a}_{\text{dynamic perturbation, } \theta_a} \tag{3.28}$$

In essence, the dynamic perturbation is defined from the static equilibrium. This perturbation, $\Delta\theta_a$, is given with respect to the structural rotational degrees of freedom and their dynamic increments. Similar to the static solution, the change in the local angle of attack is found based on the orientation of the local beam element. Based on these additions, the new aerodynamic state-space system can be defined by:

$$\begin{pmatrix}\dot{\Gamma}_{\mathbf{w}} \\ \dot{\alpha}_{\text{air}}\end{pmatrix} = \begin{bmatrix}\mathbf{K_1} & \mathbf{K_2} & -\frac{\mathbf{K_2B}_\alpha}{\mathbf{V}_\infty} & \mathbf{K_2B}_\alpha & \mathbf{K_2B}_{\text{pitch}} \\ 0 & 0 & 0 & 0 & 0\end{bmatrix}\begin{pmatrix}\Gamma_{\mathbf{w}} \\ \alpha_{\text{air}} \\ \dot{\mathbf{h}} \\ \theta_{\mathbf{a}} \\ \dot{\theta}_{\mathbf{a}}\end{pmatrix} + \begin{bmatrix}0 \\ \mathbf{I}\end{bmatrix}\dot{\alpha}_{\text{air}} \tag{3.29}$$

Here, $\mathbf{B}_\alpha$, is used to link the pitch angle with the heave motion of the wing. $\mathbf{B}_{\text{pitch}}$ is used to transform the spanwise pitch rate to the local induced angle of attack. $\mathbf{K_1}$ and $\mathbf{K_2}$ are the transfer matrices and can be traced back to Subsection 3.2.3. One important aspect of this formulation is that the time derivative of the free-stream angle of attack is taken only as an input. This equation can then be transformed to make the aerodynamic state space system a function of the structural deformations:

$$\begin{pmatrix}\dot{\Gamma}_{\mathbf{w}} \\ \dot{\alpha}_{\text{air}}\end{pmatrix} = \underbrace{\begin{bmatrix}\mathbf{K_1} & \mathbf{K_2} & -\frac{\mathbf{K_2B}_\alpha\mathbf{T_n}}{\mathbf{V}_\infty} & \mathbf{K_2B}_\alpha\mathbf{T}_\alpha & \mathbf{K_2B}_{\text{pitch}}\mathbf{T_t} \\ 0 & 0 & 0 & 0 & 0\end{bmatrix}}_{\mathbf{H_1}}\begin{pmatrix}\Gamma_{\mathbf{w}} \\ \alpha_{\text{air}} \\ \dot{\mathbf{u}}_{\mathbf{s}} \\ \theta_{\mathbf{s}} \\ \dot{\theta}_{\mathbf{s}}\end{pmatrix} + \underbrace{\begin{bmatrix}0 \\ \mathbf{I}\end{bmatrix}}_{\mathbf{H_2}}\dot{\alpha}_{\text{air}} \tag{3.30}$$

.

Here matrices, $\mathbf{T}_\alpha$, $\mathbf{T_t}$ and $\mathbf{T_n}$ transform the structural degrees of freedom to their equivalent aerodynamic terms. Similarly, the output equation can be formed by extending Equation 3.25. Proteus defines the state vector, x, as $\begin{pmatrix}\Gamma_{\mathbf{w}} & \alpha_{\text{air}} & \dot{\mathbf{p}} & \mathbf{p}\end{pmatrix}$. The bottom two rows make up the structural state vector. Based on the structural equation of motion, the state-space system can be defined as:

$$\begin{pmatrix}\ddot{\mathbf{p}} \\ \dot{\mathbf{p}}\end{pmatrix} = \underbrace{\begin{bmatrix}\mathbf{M}^{-1}\mathbf{C} & \mathbf{M}^{-1}\mathbf{K} \\ \mathbf{I} & 0\end{bmatrix}}_{\mathbf{A}_s}\underbrace{\begin{pmatrix}\dot{\mathbf{p}} \\ \mathbf{p}\end{pmatrix}}_{\mathbf{x}_s} + \underbrace{\begin{bmatrix}\mathbf{M}^{-1} \\ 0\end{bmatrix}}_{\mathbf{B}_s}\mathbf{T_{AS}R}_\alpha\mathbf{F_a^a} \tag{3.31}$$

Where $\mathbf{T_{AS}}$ is used to translate aerodynamic forces from the aerodynamic to the structural frame of reference. It must be noted that the constraint gradient matrix, $\mathbf{B}$, does not explicitly appear in the state matrix and is incorporated inherently by QR decomposition, which is elaborated in the following discussions. As a result, Equation 3.31 represents the system in terms of the reduced set of structural degrees of freedom, with the constraints inherently satisfied. In order to write Equation 3.31 in the coupled system, the aerodynamic output equation must be linked to the structural system with a set of transformation matrices. The resulting coupled state-space system can then be written as:

$$\dot{\mathbf{x}} = \underbrace{\begin{bmatrix} \mathbf{H}_1\mathbf{T}_1 \\ \mathbf{H}_4^{-1}\mathbf{H}_5 \end{bmatrix}}_{\mathbf{A}_{ss}} \mathbf{x} + \underbrace{\begin{bmatrix} \mathbf{H}_2 \\ \mathbf{H}_4^{-1}\mathbf{H}_6 \end{bmatrix}}_{\mathbf{B}_{ss}} \dot{\alpha}_{\text{air}} \tag{3.32}$$

Where the coupled output equation can then be written, taking into account the aerodynamic forces as a function of the state-vector, **x**.

$$\begin{pmatrix} \mathbf{F} \\ \mathbf{p} \\ \mathbf{B}\cdot\lambda \end{pmatrix} = \underbrace{\begin{bmatrix} \mathbf{R}_\alpha\mathbf{H}_8 \\ \mathbf{T}_4 \\ \mathbf{C_{eq}} \end{bmatrix}}_{\mathbf{C}_{ss}} \mathbf{x} + \underbrace{\begin{bmatrix} \mathbf{R}_\alpha\mathbf{H}_9 \\ \mathbf{0} \\ \mathbf{D_{eq}} \end{bmatrix}}_{\mathbf{D}_{ss}} \mathbf{u} \tag{3.33}$$

Where $\mathbf{H_8}$ and $\mathbf{H_9}$ are transformations derived to link the state vector to the aerodynamic forces. $\mathbf{T_4}$ is used to select and link the structural degrees of freedom from the state vector to the desired displacements. A more elaborate explanation of these transformations and linking matrices can be found in the derivations by Werter (2017) [51]. Lastly, **u** contains the input vector representing the gust input, $\dot{\alpha}_{\text{air}}$.

It must be noted here that the terms $\mathbf{C_{eq}}$ and $\mathbf{D_{eq}}$ are the equivalent output and feedthrough matrices respectively, and are derived from solving the equation of motion for $\mathbf{B}\cdot\lambda$ in order to resolve the reaction forces. These terms deviate from the formulation presented by Werter (2017)[51]. The current PROTEUS framework utilises a QR decomposition to reduce the full system by removing constrained degrees of freedom. This process incorporates the boundary conditions through the constraint gradient matrix **B**, ensuring that the equation of motion is free of implicit variables, such as the Lagrange multipliers. As a result, it simplifies the formulation of the state-space system, as further elaborated in Section A.1.

Furthermore, in order to integrate the state space system in time, PROTEUS utilises the trapezoidal integration scheme, which is a second-order accurate implicit time integration scheme. To use this scheme, the **A** matrix is prepared to map the state from one time step to the next and is defined as:

$$\begin{aligned} F &= F_1 \cdot \left(\mathbf{I} + \mathbf{A_{ss}} \cdot \frac{dt}{2}\right), \\ \text{where,} \quad F_1 &= \left(\mathbf{I} - \mathbf{A_{ss}} \cdot \frac{dt}{2}\right)^{-1}. \end{aligned} \tag{3.34}$$

Finally, putting the discretized system together Equation 3.35 can be written.

$$\begin{aligned} x_i &= \mathbf{F}x_{i-1} + \mathbf{B_{ss}} \cdot \frac{u_{i-1} + u_i}{2} \\ y_i &= \mathbf{C_{ss}}x_i + \mathbf{D_{ss}}u_i \end{aligned} \tag{3.35}$$

The equation above is then integrated over time and the resulting displacements and forces are extracted from the output vector y.

3.4. Limitations of the Framework

One of the main limitations of the framework revolves around the dynamic structural model. The dynamic model is built through linearising around the static equilibrium by assuming small dynamic disturbances [51]. In this formulation, the mass matrix is a result of the non-linear static equilibrium but is assumed to be constant due to linearisation. However, for a fully non-linear solution, the mass matrix will not stay constant as these displacements cause a significant mass shift. Including these effects will introduce an extra structural damping and stiffness term. Furthermore, velocity-level constraints cannot be expressed through this linearised state-space model which may lead to the hinge joint not being perfectly constrained over time which may lead to numerical errors.

Furthermore, another limitation of the framework lies in its aerodynamic wake implementation, wherein a fixed wake solution is considered. The wake is assumed to follow the free stream flow direction regardless of the airfoil deformation and is valid with a small disturbance theory. However, this assumption may not fully comply with the larger deflections of the flared folding wing tip.

3.5. Concluding Remarks

The existing literature shows that the Flared Folding Wing Tip is a viable concept for gust-load alleviation while also allowing aircraft to employ longer wings. Since its conception, it has been heavily researched and still is a relevant solution being considered in the industry. Studies have experimentally studied the concept and developed computational models. Reduced order and low fidelity models are mostly studied, incorporating ever-increasing characteristics of the FFWT. The key challenge arises in modelling the flared folding wing tip, as it requires successfully implementing the flared hinge and modelling the shifting mass with the large displacements of the wing tip. Consequently, the interaction between the FFWT and the main wing is a key modelling goal since it affects the dynamics of the complete system. Based on the review of the existing framework in PROTEUS, the current solvers appear suitable for modelling a wing with an FFWT. However, given the inherent assumptions and PROTEUS's intended use case, modelling highly non-linear systems is expected to present challenges.

A challenge in the current formulation of the non-linear static solver arises from its reliance on the Newton-Raphson algorithm, which requires an initial displacement guess to solve for subsequent load steps. While this approach performs well for smaller displacements with stiffer geometries, it becomes less reliable for multi-body systems undergoing larger displacements. In such cases, the initialisation of the solver plays a critical role in ensuring stability and accuracy, and further refinement of this process is essential to improve solver performance. Furthermore, this method incrementally increases the load while solving for equilibrium between structural and external forces based on their respective stiffness matrices. However, for small load values, as the FFWT generates near-zero lift and the hinge lacks rotational stiffness about one axis, these matrices may become poorly conditioned, leading to numerical issues that can result in inaccurate or physically inconsistent solutions.

Finally, modelling this concept within the dynamic framework remains manageable as long as the state-space representation of the system remains unchanged, owing to the linearisation of the solver around the static equilibrium. This existing framework is highly interdependent and performs well for stiffer problems; however, for a multibody system such as this, a more advanced non-linear solver would be required, which is beyond the scope of this thesis. However, addressing the research question on the dynamic release of the wing using the current framework requires careful consideration of the changes in the reaction forces and system representation involved during state transitions. Accurately capturing these changes is crucial for improving the fidelity of the existing model and providing reliable insights into the system's dynamic behaviour, which will be explored in the following chapters.

II

Methodology

4 Multibody Formulation & Implementation

The flared folding wing tip is connected to the main wing using a hinge joint. A hinge joint is a so-called *lower pair joint* which restricts the movement of the two joining bodies to only one rotational degree of freedom. A hinge joint, also known as a revolute joint, can be modelled through *five* constraints: three displacement constraints and two rotational constraints. The three displacement constraints that impose equality of position at the connecting nodes given by Equation 4.1 must be defined to connect the two bodies and they can be imposed using basic boolean relations. Lastly, two rotational constraints must be placed that restrict relative rotation about two directions given by Equation 4.2[42].

$$x_A - x_B = 0 \tag{4.1}$$

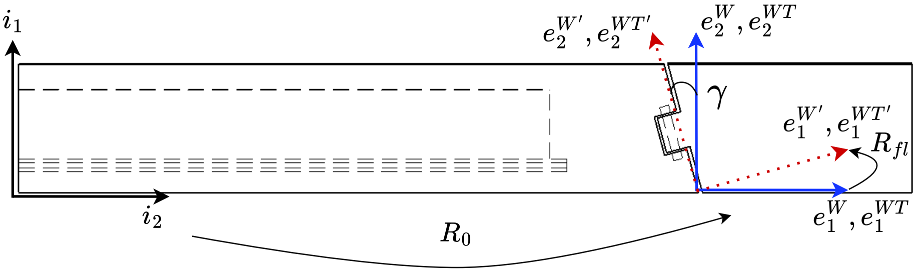

Figure 4.1: Representation of the Wing and Hinge in Initial Configuration

To develop these constraints, the correct reference system must be established. Figure 4.2 illustrates the different rotations and is based on the reference systems used in the co-rotational framework of PROTEUS, as introduced in Subsection 3.1.1. The base reference system (or body-fixed frame) is defined by the triad $\{i_1, i_2, i_3\}$, where i_1 is the chordwise direction vector, i_2 the spanwise direction vector and i_3 represents the out-of-plane direction vector. To align this body-fixed frame with the initial orientation of the shared nodes at the inner wing tip and the root of the FFWT, the transformation R_0 is applied. This rotation maps the body fixed frame to the respective local frames: $\{e_1^W, e_2^W, e_3^W\}$ for the inner wing tip and $\{e_1^{WT}, e_2^{\mathrm{WT}}, e_3^{\mathrm{WT}}\}$ the FFWT root.

However, if there is a flare, the hinge axis is not aligned with this reference system. To correct this, an additional transformation, R_{fl}, must be performed to align e_2 with the hinge axis as illustrated in Figure 4.1. As the wing and the wing tip deform, their respective triads: $e_1^{W'}, e_2^{W'}, e_3^{W'}$ for the wing and $e_1^{\mathrm{WT}'}, e_2^{\mathrm{WT}'}, e_3^{\mathrm{WT}'}$ for the FFWT, are transformed to their deformed configuration with rotation matrices, R_g^W and R_g^{WT} respectively shown in Figure 4.2.

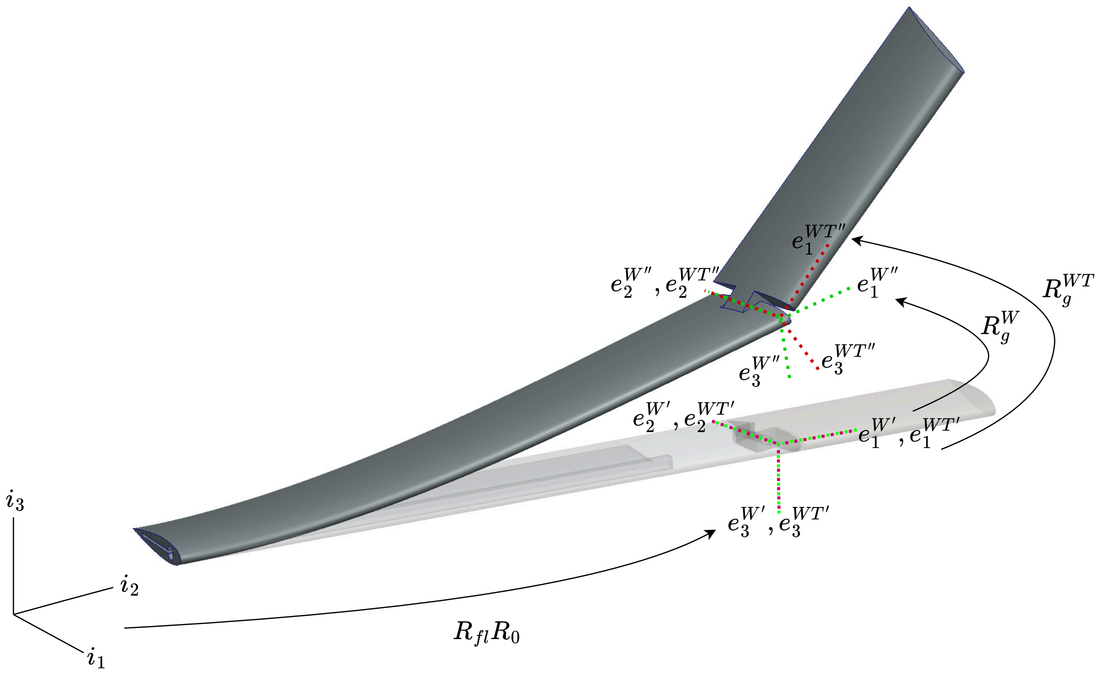

Figure 4.2: Reference System Representation from Initial to Deformed configuration

Matrices R_g^W and R_g^{WT} are transformations to rotate the triads aligned with the flare from their initial configuration to the deformed configuration. Equation 4.2 gives the orthogonality constraints which can be imposed to define the hinge.

$$\begin{aligned}\Phi_1 &= e_1^{W^T\prime} R_g^{W^T} R_g^{\mathrm{WT}} e_3^{\mathrm{WT}\prime} = 0\\ \Phi_2 &= e_2^{W^T\prime} R_g^{W^T} R_g^{\mathrm{WT}} e_3^{\mathrm{WT}\prime} = 0\end{aligned} \tag{4.2}$$

Taking the variation of these constraints in Equation 4.2 to develop the gradient constraint matrix:

$$\delta\Phi = B\delta q \tag{4.3}$$

Where B signifies the Jacobian of the constraint, $\frac{\partial\Phi_i}{\partial q_i}$, and q are the system's degrees of freedom for node i. Computing the gradient constraint matrix for the first two constraints (Φ_1 and Φ_2) and adopting the incremental form, Equation 4.4 is obtained.

$$\delta\Phi_N = (\delta R_g^{W^T} e_i^W)^T R_g^{\mathrm{WT}^T} e_2^{\mathrm{WT}} + (R_g^{W^T} e_i^W)^T \delta R_g^{\mathrm{WT}^T} e_2^{\mathrm{WT}} \quad N = 1,2; \quad i = 1,3 \tag{4.4}$$

The variation of the rotation operators $\delta R_g^{W^T}$ and $\delta R_g^{\mathrm{WT}^T}$ can be found using :

$$\delta R_g^n = R_g^n \delta\Theta_n \qquad n = W, \mathrm{WT} \tag{4.5}$$

Consequently, the variation of the local rotation vector Θ of a node n is given by:

$$\delta\Theta_i^n = T(\phi_i^n)\delta\phi_n \tag{4.6}$$

where $\delta\phi_n$ represents the variation of the three rotational degrees of freedom, ϕ_i^n (for $i = 1,2,3$), at the wing or wing-tip node n. And $T_n(\phi_i)$ is a transformation matrix that maps the variation $\delta\phi_n$ onto the local coordinate system of the node, and can also be referred to as the tangent operator. The three nodal rotational degrees of freedom, i, associated with each wing tip and the FFWT root are illustrated in Figure 4.3.

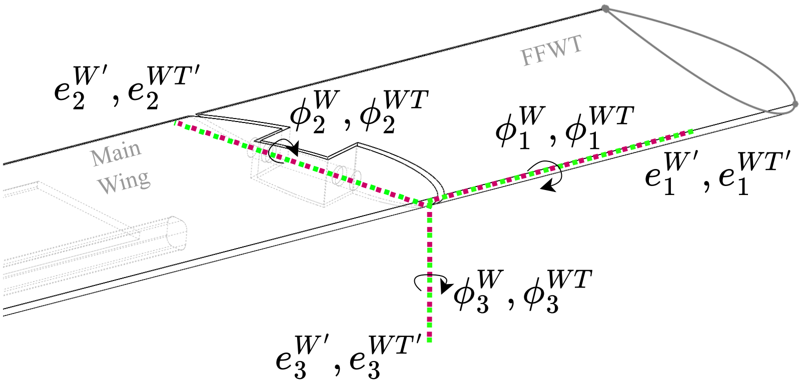

Figure 4.3: Representation of the nodal rotational degrees of freedom at the inner wing tip (W) and FFWT root (WT)

This transformation allows the change in the rotation to be expressed in terms of the nodal rotational degree of freedom, $\delta\phi_n$, which typically corresponds to the angular displacement or orientation change of the node in its local frame. Finally, replacing δR_g in Equation 4.4 with $R_g T_n(\phi_i^n)\delta\phi_n$ resulting in:

$$\delta\Phi_N = (R_g^{W^T} T_W \delta\tilde{\phi}_W\, e_i^W)^T R_g^{\mathrm{WT}^T} e_2^{\mathrm{WT}} + (R_g^{W^T} e_i^W)^T R_g^{\mathrm{WT}^T} T_{\mathrm{WT}}\, \delta\tilde{\phi}_{WT}\, e_2^{\mathrm{WT}} \quad N = 1,2; \quad i = 1,3 \tag{4.7}$$

Exchanging the skew operation in Equation 4.7, the theta variations can be taken out as common terms. Collecting these ϕ_i^n terms and putting the equation in matrix form:

$$B = \begin{bmatrix} (R_g^{W^T} T_W \tilde{e}_1^W)^T R_g^{\mathrm{WT}^T} e_2^{\mathrm{WT}} & (R_g^{W^T} e_1^W)^T R_g^{\mathrm{WT}^T} T_{\mathrm{WT}} \tilde{e}_2^{\mathrm{WT}} \\ (R_g^{W^T} T_W \tilde{e}_3^W)^T R_g^{\mathrm{WT}^T} e_2^{\mathrm{WT}} & (R_g^{W^T} e_3^W)^T R_g^{\mathrm{WT}^T} T_{\mathrm{WT}} \tilde{e}_2^{\mathrm{WT}} \end{bmatrix} \tag{4.8}$$

This gradient constraint matrix for the rotational degree-of-freedom of the hinge node, Equation 4.8, can be integrated into the complete gradient matrix. As aforementioned in Subsection 3.1.3, the Newton-Raphson root finding method solves for the displacement and the Lagrange multipliers by incrementing the load, which in this model is controlled by the flow velocity. Hence, the wing tip will droop due to gravity and a lack of lift force at lower velocities. If the increments are small, the initial load steps can incur zero-division errors, stressing the importance of initialising the solver properly. The following sections present the model used and the set-up of the static and dynamic solvers.

4.1. Model Description

The simulations were performed with an exaggerated wing-box model. The main wing is modelled as a cantilever with all degrees of freedom locked at the wing root. The main wing spans 16 meters and has a chord of 2.5 meters, while the flared folding wing tip spans another 4 meters. The folding wing tip is then attached to the tip of the main wing with the multi-body constraint formulation. The wing's exaggerated dimensions are taken to have a high aspect ratio of 16. It is found that this aspect ratio is suitable for the wing to exhibit displacement up to 1.5 m which is enough to study the effect of the FFWT.

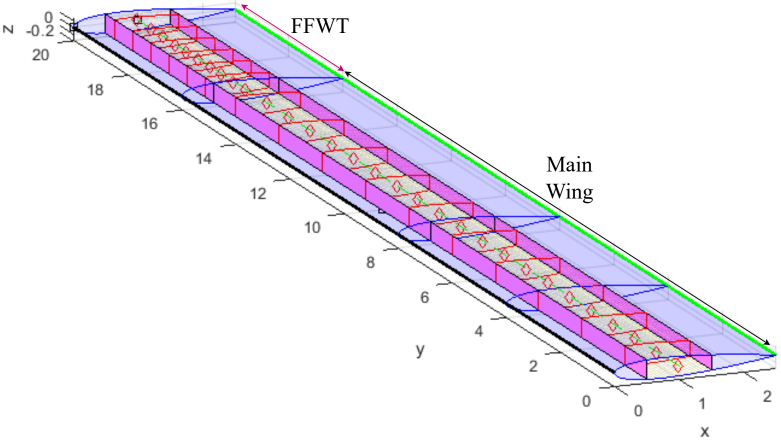

Figure 4.4: Model Geometry visualised through PROTEUS

The main wing is represented with 10 beam elements and the FFWT is comprised of 6 beam elements, which are found to be adequate to model the behaviour of the wing. Keeping around 1.5 to 2 aerodynamic panels per beam elements 16 and 12 aerodynamic panels are placed spanwise for the main wing and the FFWT respectively. 5 chordwise panels are used and 10 chord lengths of wake are modelled with 8 wake panels per chord.

4.2. Static Solver

The static solver is explained in Subsection 3.1.3, however, in order to solve for the multi-body system, the initial displacement prediction for the Newton-Raphson solver are set to zero. The static solution is solved with three different configurations:

1. Six Degrees-of-Freedom (DoF) Locked
2. Locked Hinge
3. Free Hinge

The six-DoF locked case is built by constraining all the nodal degrees of freedom at the joint by placing a 1-to-1 relation between the shared nodes. The locked hinge is created by adding an extra constraint to the existing hinge constraint and equating the rotational degree of freedom about the hinge axis for the shared nodes. These two cases should provide the same wing tip displacements. The free hinge is built by removing the rotational constraint from the second case following the formulation developed in Equation 4.8. Hence, allowing free rotation about the hinge axis.

Lastly, to better account for large rotations, the solver tolerances are separated and defined individually for displacements, rotations, and Lagrange multipliers. Unlike the existing approach, where tolerances are applied to the complete solution vector, this refinement allows for more precise control over the convergence criteria. By tuning the tolerances for each component separately, the solver can achieve convergence more effectively while maintaining accuracy.

4.3. Dynamic Solver

The dynamic solution is obtained by linearising around the static equilibrium. Since small perturbations are assumed, the mass matrices remain constant, and the state-space system is formulated once. Although this approach is not ideal for problems involving large displacements— as it does not account for changes in mass distribution and stiffness—certain modifications could allow it to model this system more effectively.

Releasing the FFWT leads to a change of reaction forces at the constrained points. To incorporate this change, the difference in the reaction forces between the two equilibrium states (fully locked and free hinge) can be introduced in the input vector as a constant force. For both the locked and unlocked cases, the reaction forces can be calculated by multiplying the Lagrange multipliers by the constraint gradient matrix, $\mathbf{B^T} \cdot \lambda$.

$$\Delta F_\lambda = \mathbf{F}_\lambda^\mathbf{L} - \mathbf{F}_\lambda^\mathbf{F} \tag{4.9}$$

$\mathbf{F}_\lambda^\mathbf{L}$ is the reaction force vector found through the static solver with the hinge locked, likewise $\mathbf{F}_\lambda^\mathbf{F}$ is the reaction force vector for a free hinge at static equilibrium. This ΔF_λ can be incorporated into the state-space through the input. As shown in Equation 3.32, $\mathbf{B_{ss}}$ is used to incorporate the aerodynamic forces into the coupled system. Hence, by performing the same transformation, and multiplying the ΔF_λ by the structural input matrix $\mathbf{B_s}$. The coupled input matrix initially only includes correlates the aerodynamic forces into the state-space system and is given by:

$$\mathbf{B_{ss}} = \begin{bmatrix} \mathbf{H_2} \\ \mathbf{H_4^{-1} H_6} \end{bmatrix}$$

Here $\mathbf{H_4^{-1} H_6}$ is a transformation from the aerodynamic to the coupled reference system. Incorporating the new $\mathbf{M^{-1}} \Delta \mathbf{F}_\lambda$ term, using the structural input matrix, the new free-hinge coupled input matrix can be given by:

$$\mathbf{B}_\mathbf{ss}^F = \begin{bmatrix} \mathbf{H_2} & \mathbf{0}_{\text{n-aero}\times\text{n-dof}} \\ \mathbf{H_4^{-1} H_6} & \mathbf{H_4^{-1} B_s} \end{bmatrix}. \tag{4.10}$$

$\mathbf{B_s}$ is given as $\left(\overline{\mathbf{M}^{-1}} \quad 0\right)^T$, and $\mathbf{H_4^{-1}}$ transforms the input, ΔF_λ, from the structural reference system to the coupled system. The matrix $\mathbf{0}_{\text{n-aero}\times\text{n-dof}}$ is placed here to span the null space of the structural degrees of freedom in the input vector, where *n-aero* and *n-dof* denote the aerodynamic inputs and the structural degrees of freedom, respectively. Based on this modification, the new structural state space system can be given by:

$$\dot{\mathbf{x}}_\mathbf{s} = \mathbf{A_s x_s} + \mathbf{H_4^{-1} H_6 \, F_a^a} - \mathbf{H_4^{-1} B_s} \Delta \mathbf{F}_\lambda \tag{4.11}$$

Equation 4.11 gives the state-space equation where the change in reaction force between the two states is accounted for. Recalling Equation 3.35, the new $\mathbf{B_{ss}}$ and $\mathbf{D_{ss}}$ matrices are replaced to account for the change in reaction loads. Given that PROTEUS employs a trapezoidal time integration scheme, the state from the previous time step is used to calculate the state of the current time step. This new state is then used to calculate the output. The output equation is formed by solving Equation 4.12 to Equation 4.14.

$$\mathbf{F_A} = \mathbf{RAS} \cdot \mathbf{H}_7 \cdot \mathbf{X}_{c2f} \cdot \mathbf{x} + \mathbf{RAS} \cdot \mathbf{H}_8 \cdot \dot{\alpha} \tag{4.12}$$

Equation 4.12 calculates the aerodynamic forces, wherein, $\mathbf{RAS} \cdot \mathbf{H_7}$ and $\mathbf{RAS} \cdot \mathbf{H_8}$ are transformation matrices which select the required values from the state and input vectors and transform the forces to the aerodynamic reference system. $\mathbf{X}_{c2f}$ is the inverse of the QR decomposition (introduced at the end of Section 3.3) used to reduce the full system to only account for the free degrees of freedom.

$$\mathbf{p} = \mathbf{T}_4 \cdot \mathbf{X}_{c2f} \cdot \mathbf{x} + [0]_{n\times m} \cdot \dot{\alpha}, \tag{4.13}$$

The displacements are then found using Equation 4.13, where the state vector is transformed from the reduced to the full system using $\mathbf{X}_{c2f}$, and $\mathbf{T_4}$ is an array of ones and zeros selecting the displacements from the complete state vector. The matrix $[0]_{n\times m}$ ensures that the contribution of the m aerodynamic inputs is nullified in the calculation of structural displacements.

Finally, the reaction forces can be extracted by solving the equation of motion as shown in Equation 4.14.

$$\mathbf{M} \cdot \ddot{\mathbf{p}} + \mathbf{C} \cdot \dot{\mathbf{p}} + \mathbf{K} \cdot \mathbf{p} + \mathbf{B}^T \cdot \boldsymbol{\lambda} = \mathbf{F} \tag{4.14}$$

Solving for $\mathbf{B^T}\lambda$,

$$\mathbf{B^T}\lambda = \mathbf{F} - (\mathbf{M} + \mathbf{C} \cdot \dot{\mathbf{p}} + \mathbf{K} \cdot \mathbf{p}) \tag{4.15}$$

This gives the coupled output $\mathbf{C}$ matrix:

$$\mathbf{C_{ss}} = \begin{bmatrix} \mathbf{RAS} \cdot \mathbf{H}_7 \cdot \mathbf{X}_{c2f} \\ \mathbf{T}_4 \cdot \mathbf{X}_{c2f} \\ \mathbf{C_{eq}} \cdot \mathbf{X}_{c2f} \end{bmatrix} \tag{4.16}$$

Where $\mathbf{C_{eq}}$ is an expression following Equation 4.15, to extract the reaction forces from the state vector. The effect of the ΔF_λ does not need to be re-evaluated in the feed-through matrix, since the reaction forces are already being calculated based on the derivative of the displacements from the state vector of the current time-step. Hence the new $\mathbf{D_{ss}}$ matrix takes the following form:

$$\mathbf{D}^F_\mathbf{ss} = \begin{bmatrix} \mathbf{H_2} & \mathbf{0}_{\mathrm{n\times m}} \\ \mathbf{D_{eq}} & \mathbf{0}_{\mathrm{n\times m}} \end{bmatrix}. \tag{4.17}$$

Where, $\mathbf{H_2}$ is a selection array given by $\begin{pmatrix}\mathbf{RAS} \cdot \mathbf{H_8} & 0_{i\times k}\end{pmatrix}^T$, and i and k are matrix sizes depending on the aerodynamic inputs and the reduced structural degrees of freedom. $\mathbf{R_{AS}} \cdot \mathbf{H_8}$ extracts the related gust input values and $0_{n\times m}$ is an array of zeroes related to the corresponding displacement values. Finally, $\mathbf{D_{eq}}$ is a corresponding equation based on Equation 4.15 for the calculation of the reaction forces.

4.4. Dynamic Release

The dynamic solver is linearised around a static equilibrium and integrated in time from that position. In its current form, the model can only test two cases: a hinge that is either locked or free from the start. However, to be able to model a hinge release at different points of a gust encounter, the model is extended by using two dynamic state-space formulations which are combined to accommodate a delayed hinge release.

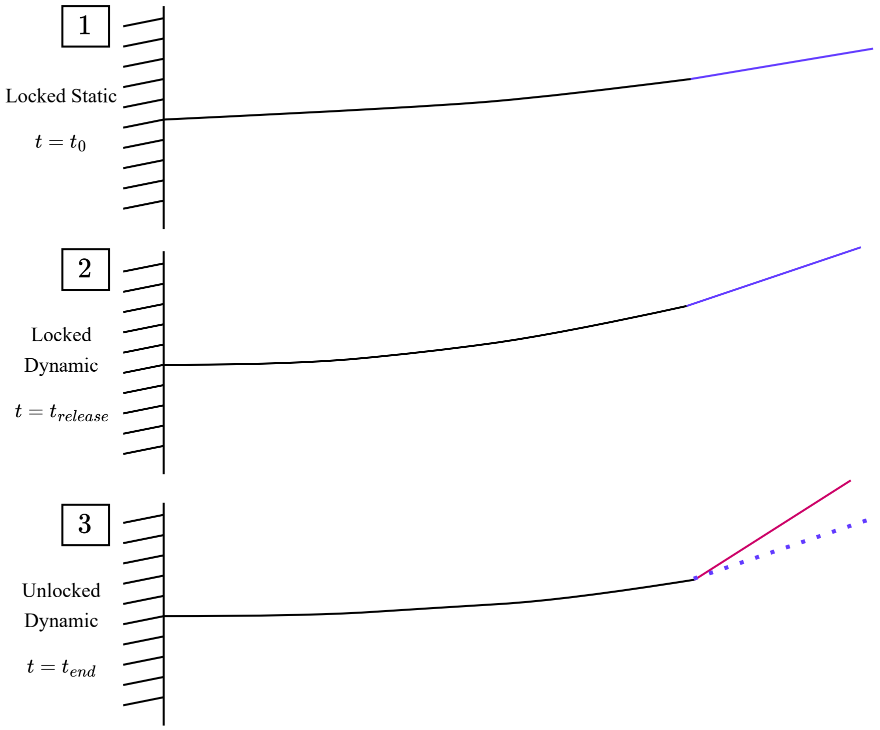

Figure 4.5: Dynamic Solver Steps

The static solution is found for both the locked and unlocked hinge configurations to extract the difference in the $\Delta\mathbf{F}_\lambda$, which is then integrated into the dynamic solver. This is done by appending this $\Delta\mathbf{F}_\lambda$ into the input vector and is resolved through the input matrix as given in Equation 4.10. Figure 4.5 shows the three integral steps of the dynamic release solution. The dynamic solver is initiated using the static locked solution and time-stepped to the release time, $t_{release}$.

At the release time, the state-space system transitions from one initialised with a locked-hinge constraint to another where the hinge constraint is unlocked, achieved by modifying the gradient constraint matrix **B**. Both state-space formulations are linearised around the same locked equilibrium configuration, which is obtained from the non-linear static analysis. To further illustrate the flow of the information Figure 4.6 can be used. However, at the release time, there is a difference in the state vector itself. Since one more degree of freedom is free, the new reduced state is larger since an extra and **p** are added to the state. To facilitate this transformation, the reduced state vector, **x**, is first expanded back to its full state representation, incorporating the constrained states. It is then reduced again according to the decomposition of the free-hinge system, which includes the two additional states mentioned. From the release point to the endpoint, the solver solves with the state-space configured with the unlocked hinge as shown in the third state of Figure 4.5.

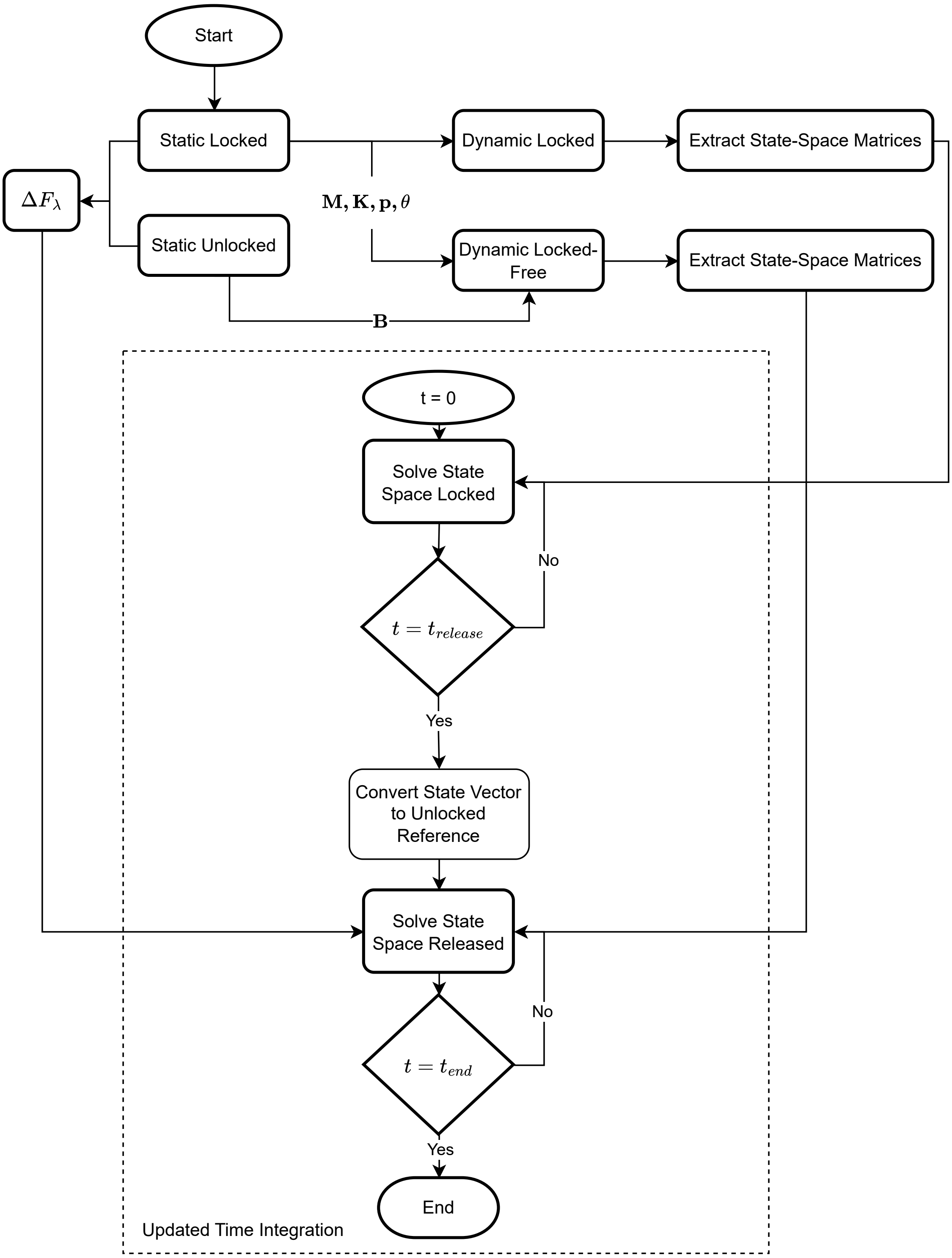

Figure 4.6: Dynamic Solver Process

4.5. Key Assumptions

The static and linear models operate based on a set of assumptions that must be highlighted and should be considered when analysing the results produced by the solver.

- The flare of the hinge alters the geometry of the FFWT, positioning the hinge at an angle. However, the aerodynamic wake mesh remains based on the beam representation of the wing and FFWT, leading to a slight discrepancy between the expected vortex and the vortex generated by the solver, which in turn affects the UVLM results.
- The dynamic solution is derived by linearising around a non-linear static solution. This approach does not fully account for larger deformations, as expected with the folding wing tip.
- Building on the previous point, the effects of linearisation become more pronounced in the locked-to-free hinge model. Since the state spaces are constructed based on the static equilibrium of a locked hinge, there is a significant shift in mass distribution between the linearised reference point and the post-unlock orientation of the wing and FFWT
- The locked-to-unlocked hinge framework transitions between two state spaces: the fully locked state space and an unlocked hinge state space, initialised from the locked position. It is assumed that once the FFWT is unlocked, the system will settle at the unlocked static solution. However, the intermediate transition between these states is not accounted for, which may introduce errors—especially as the system deviates from the small perturbation assumption and inertial effects due to unlocking are neglected.
- Lastly, the aerodynamic solver assumes small unsteady perturbations and uses a rigid wake formulation. This assumption breaks down in the case of a multi-body system with a free degree of freedom, where the rotations are significantly larger.

III

Results & Discussion

5 Static Results

This chapter of the results will focus on presenting and analysing the system's static response. The static solution works by equating the internal forces to the external forces of the wing. Hence, the solution can be used to find the equilibrium positions of the wing at different velocities. Multiple cases will be presented and compared to assess the performance of the FFWT. Baseline cases without the FFWT will be considered to capture the effects of integrating the wing-tip.

5.1. Static Validation Exercise

To assess the solver's validity, an initial verification was performed by comparing the fold angles of the flared folding wing-tip to the corresponding angles of a hinged plate from a simple analytical solution.

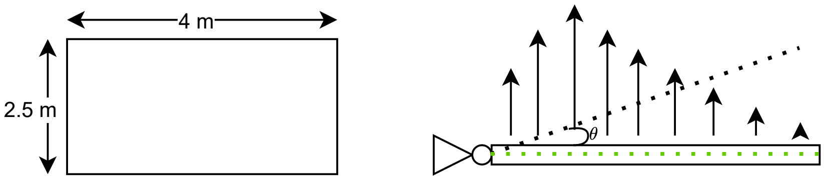

Figure 5.1: Analytical Problem Set-up

The dimensions and the load case are presented in Figure 5.1. For a flat plate, the coefficient of lift, C_L, can be approximated as $2\pi\alpha$, where α is the angle of attack. Under the assumption of ideal flow, which is characterised by incompressibility where the fluid density remains constant, irrotational where vorticity is neglected unlike in PROTEUS, inviscid behaviour where viscous effects are negligible, and steady conditions, the lift force acting on the plate can be calculated as:

$$F_L = \frac{1}{2}\rho V^2 S C_L. \tag{5.1}$$

Where ρ is the density, V_∞ is the flow velocity, and $S$is the plate area. From the plate's static equilibrium with different flow velocities, the fold angles θ as shown in Figure 5.2, can be calculated. The root-heavy lift distribution of the plate is incorporated by taking the distance of the lift force from the plate hinge, d, from the component-wise lift distribution of the wing-tip, as modelled in PROTEUS.

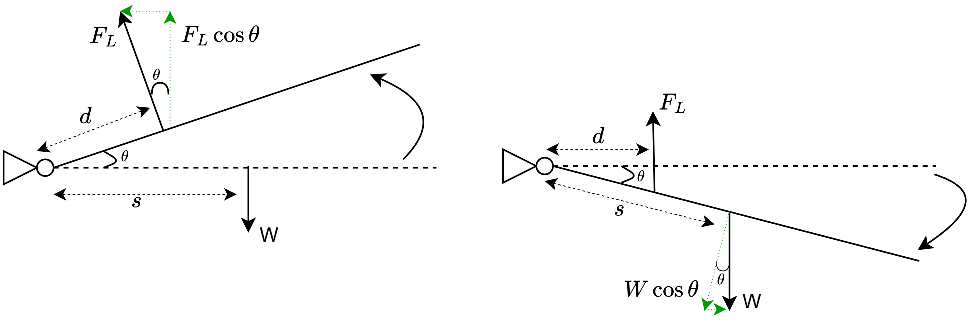

Figure 5.2: Moment Balance Set-up

Figure 5.3 presents the fold angles achieved. The analytical solution over-predicts the fold angles due to several assumptions inherent in the analytical approach. The lift force calculation neglects three-dimensional effects and does not account for the downwash, as captured by PROTEUS, resulting in higher predicted lift values. Additionally, PROTEUS encounters difficulties in predicting low-velocity solutions due to poor numerical convergence. This convergence issue likely arises from initialisation errors, where the aerodynamic stiffness matrix is poorly conditioned due to the minimal or even zero lift generated by a drooping FFWT. Despite these assumptions, the model exhibits similar patterns to the numerical solution. With further corrections and consideration of three-dimensional flow effects, the discrepancy between the two cases can be reduced.

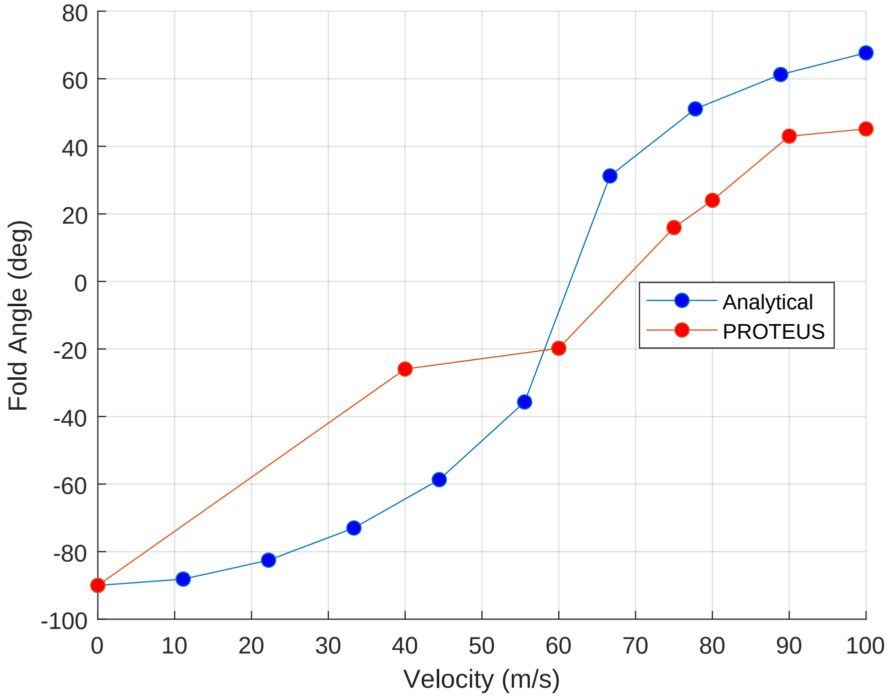

Figure 5.3: Comparison between fold angles achieved from analytical solution and PROTEUS.

5.2. Wing-root Bending Moment

The wing-root bending moment (WRBM) is expected to decrease when the hinge is unlocked. This reduction occurs because the folding wingtip (FFWT) reaches a new rotational equilibrium, effectively shortening the moment arm relative to the wing root. Figure 5.4 illustrates the impact of different flare angles on the WRBM, with the red marker highlighting the WRBM when the hinge is locked.

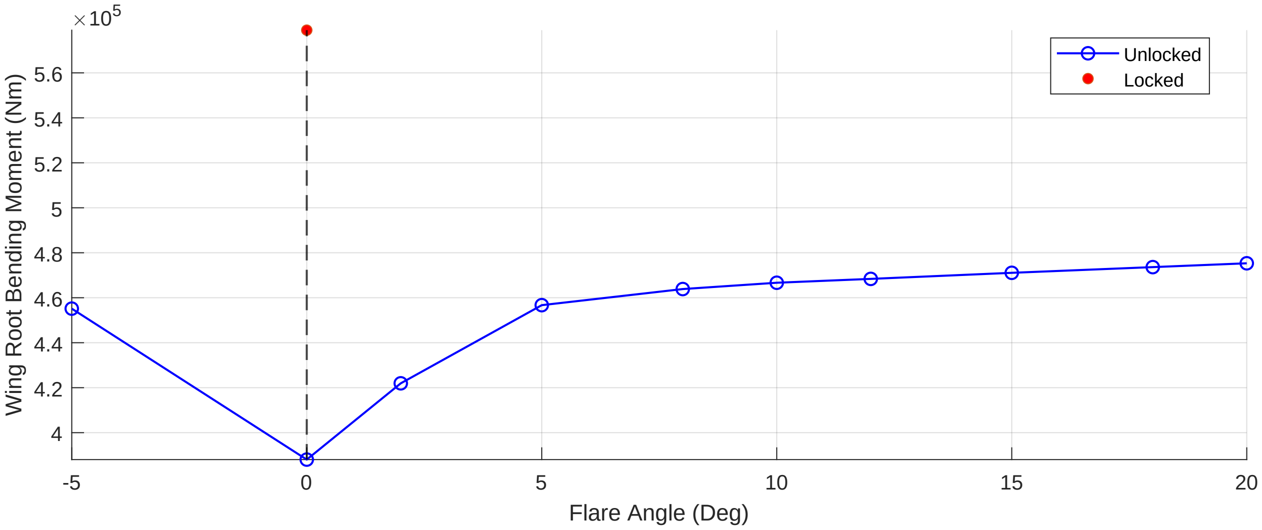

Figure 5.4: Wing Root Bending Moment over different flare angles

For all cases shown, the free-stream velocity is set to 75 m/s, and the wing's angle of attack is 2 degrees. The simulations reveal that unlocking the hinge reduces the WRBM, with a decrease of approximately 26% at zero flare. This reduction is primarily due to two factors:

1. A decrease in overall lift when the FFWT is free to rotate.
2. A shorter effective moment arm which reduces the bending load at the root.

Additionally, the WRBM varies with changes in the flare angle. As the flare angle increases in either the inboard or outboard direction, the WRBM also increases. Specifically, increasing the flare from 0 to 20 degrees results in a 23.3% increase in WRBM. This trend can be explained by two key effects: the increased aerodynamic stiffness of the FFWT as the flare angle grows, and the introduction of a new moment component about the hinge axis, which adds to the overall bending load.

5.3. Hinge Reaction Moments

One interesting observation from the static solutions emerges when examining the effect of the flare angle on the reaction moments at the hinge. Five constraints are imposed to define the hinge, each contributing a corresponding reaction force. Focusing on the two rotational constraints, one primarily counteracts the torsional effects of the wing-tip, while the other resists lead-lag motion. Figure 5.5 illustrates the different components of the hinge moment. Here, M_{hinge} represents the primary hinge moment, decomposed into its horizontal component, M_{τ}, which captures the torsional contribution, and M_{β}, representing the hinge's bending moment. Similarly, two moments arise due to the angle of attack: M_{LL}, the lead-lag component, and $M_{\beta-H}$, the bending component. Based on the size of the flare angle, these components are affected as shown in Figure 5.6. At 0-degree flare, the reaction moments computed by the solver deviate from the trend observed at other flare angles. This discrepancy may stem from errors associated with small flare angles and the solver's numerical stability, as discussed in Section 5.1. Additionally, potential initialisation errors combined with the solution tolerances could contribute to these results.

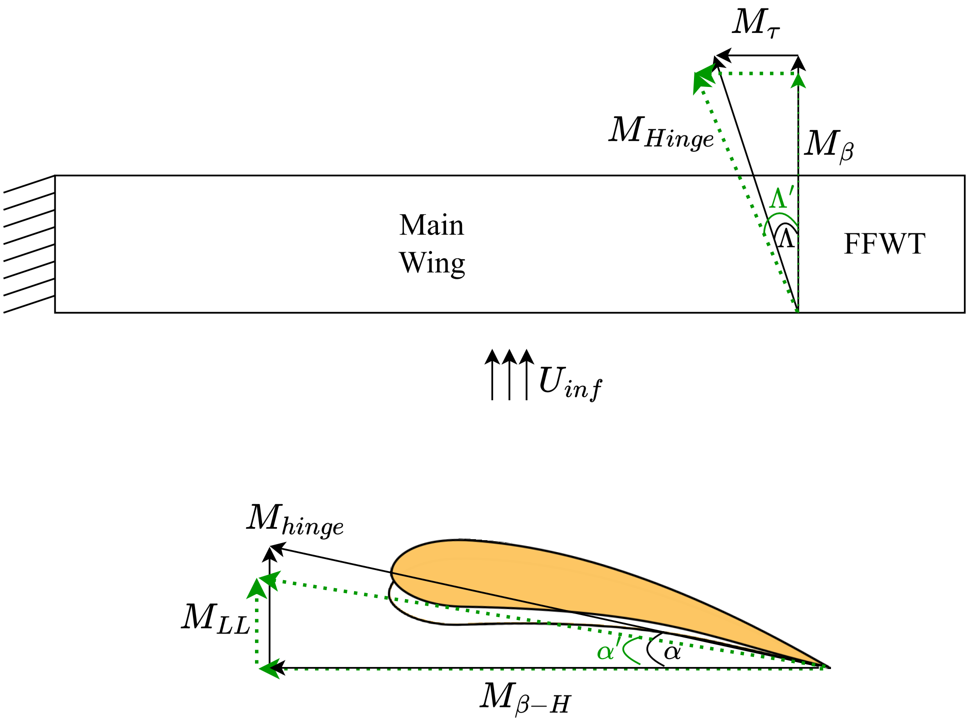

Figure 5.5: Moments around Hinge

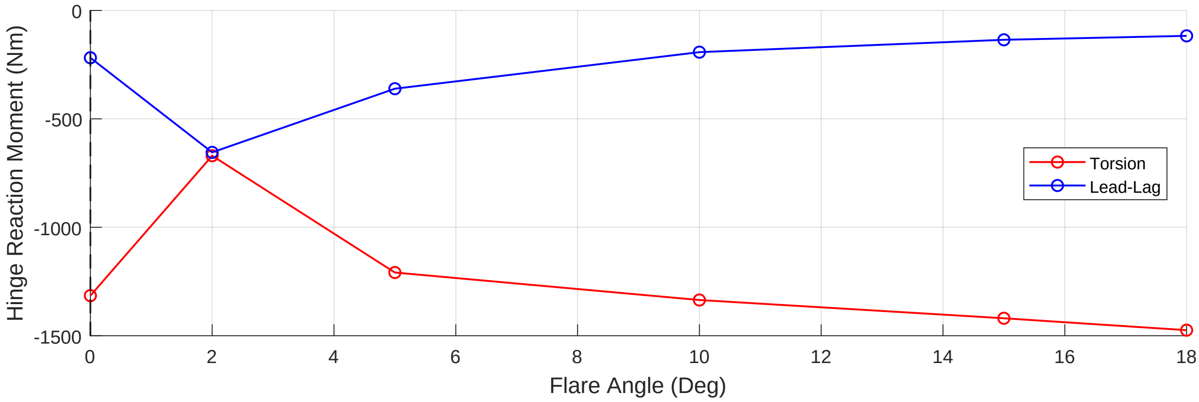

Figure 5.6: Free hinge moment with respect to different flare angles

It can be noticed that the torsion reaction moment increases with the increasing flare, while the lead-lag decreases. This trend is expected and can be explained using Figure 5.5. To explain the increase in torsional moment, the moment components must be understood. As the flare angle increases, the M_τ component increases while the M_β decreases. M_τ component is responsible for the torsional movement of the wing-tip, hence this reaction force increases with the increasing flare angle. While the reduced M_β results in reduced lead-lag. It should also be noted that the lead-lag moment becomes higher at smaller angles than the torsion, corresponding to the decreasing spanwise moment component. Due to the flare, the spanwise moment counteracts the torsional moment near the wing-tip. Around 2 degrees of flare, this countering torsional moment becomes lower than the moment due to the lift. Furthermore, since there is no reduction in the local angle of attack, the lead-lag also increases heavily.

At 0 degrees flare, the torsional and the lead-lag moment increase drastically but in the opposite direction, with the torsional moment again larger than the lead-lag. This could be attributed to possible numerical errors

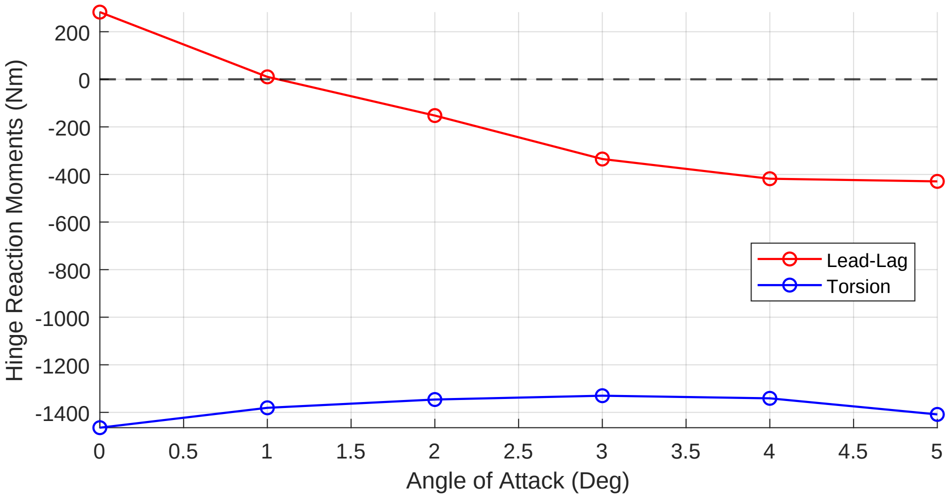

Figure 5.7: Free hinge moment with increasing angle of attack

Figure 5.7 gives the relation between the reaction moments and the increasing angle of attack at a constant flare angle of 10^o. The plot can further show that the lead-lag is primarily affected by the airfoil's angle of attack, while the torsion moment is not affected as much. However, comparing Figure 5.6 and Figure 5.7, a larger reduction in the lead-lag moment can be identified with the growing flare angle.

This additional moment also causes slightly higher inner wing-tip displacements. The static solution of a full wing with a locked hinge gives a displacement of 1.627 meters, meanwhile freeing the hinge reduces the tip displacement to 0.888 meters, further discussed in Section 5.4.

The changing moment arm also contributes a small amount to the system's dynamics. Rotating the hinge axis changes the FFWT's centre of gravity, consequently causing a change in the moment arm from the hinge axis. For a flat plate, the shift of the centre of gravity is more pronounced; however, due to the irregular shape of the airfoil, the mass distribution is skewed towards the leading edge, hence the shift is less apparent.

5.4. Wing-tip Displacement

The reduction in the wing-root bending moment also reduces peak wing-tip displacements of the main wing. By releasing the hinge, the moment arm itself decreases, causing the inner wing-tip displacement to be lowered as well. The effect of different flare angles and different angles of attack are studied in this section. Figure 5.8 shows the wing displacements with the locked and the unlocked hinge configurations for a 10-degree flared configuration. The inner wing-tip deflection is reduced significantly with the hinge unlocked. Further, similar plots can be found in Figure A.1.

Depending on the velocity and the wing's angle of attack, the difference in wing-tip displacement becomes more apparent. Figure 5.9 plots the wing-tip displacements at different flare angles. The reduced inner wing-tip displacement is evident in the cases with the unlocked hinge. Wing-tip displacement for the locked case reaches 0.968 m, whereas the tip deflection reduces by around 50% with an unlocked hinge.

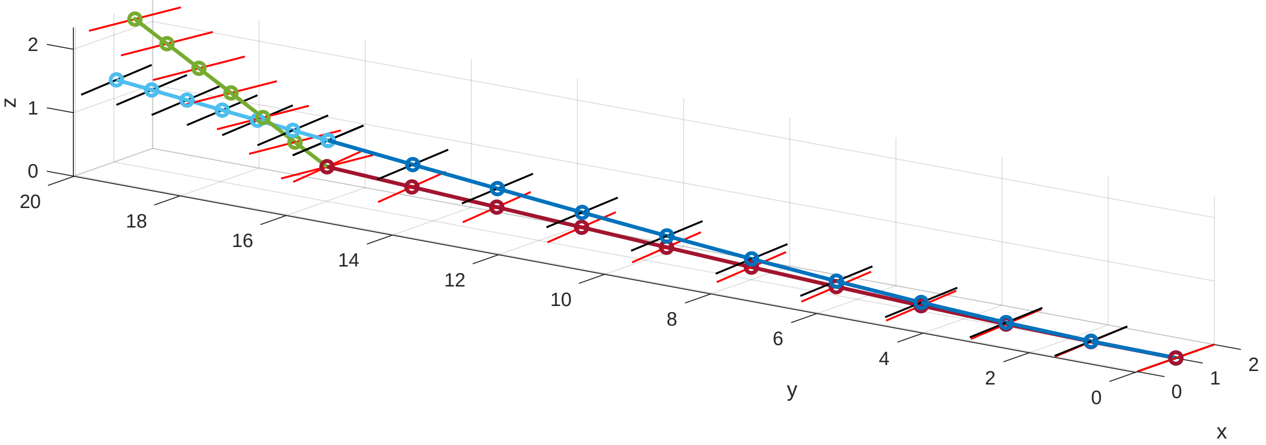

Figure 5.8: Wing displacements of locked and unlocked hinge configurations at 10° flare.

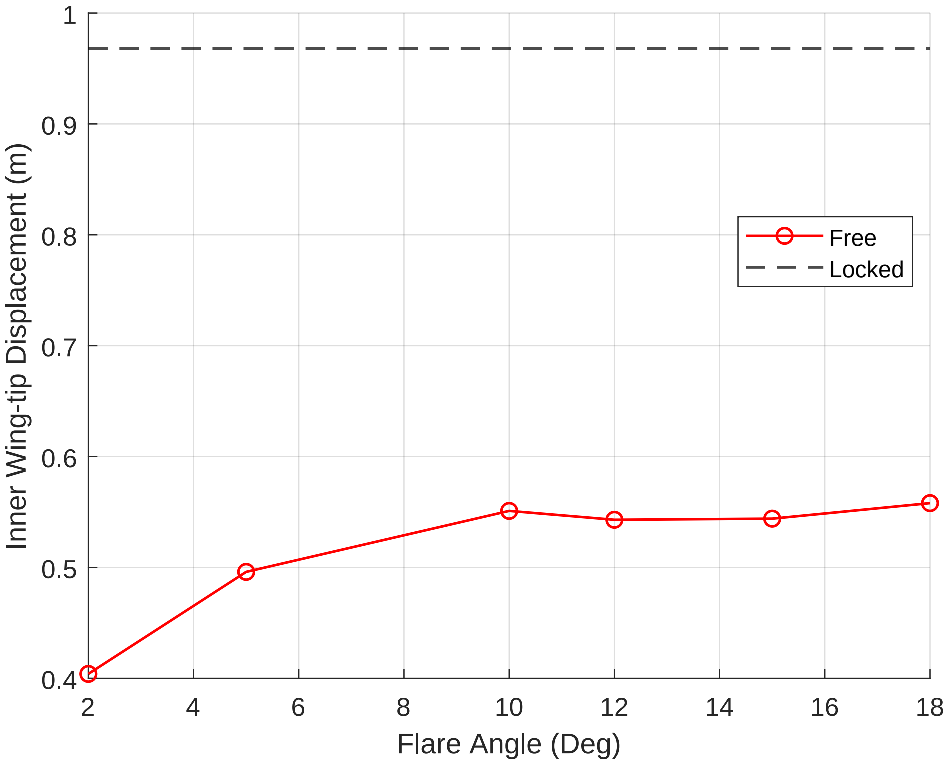

Figure 5.9: Inner wing-tip displacement with varying flare angles.

Further insight can be drawn from analysing the lift distribution across the wing. The free-stream angle of attack is set to 5° and the lift distribution is compared for different flare angles. Figure 5.10 shows the panel-wise lift distributions with increasing flare angle. The blue curve shows the lift distribution under locked conditions. There is a discontinuity in the curves, which is created due to the component-wise lift distribution. The lift near the tip is higher compared to the unlocked case because the wing-tip is fully engaged in generating lift, similar to the rest of the wing.

An observation for all the cases is that the lift values are all consistently slightly lower with the unlocked hinge. The unlocked hinge reduced the wing deformation but also caused an overall shift in the aerodynamic lift generation. The inner wing, with an unlocked hinge, acts more independently with a shorter span which results in reduced aerodynamic efficiency of the inner wing. The reduced overall lift can be attributed to this reduction in the aerodynamic efficiency of the wing.

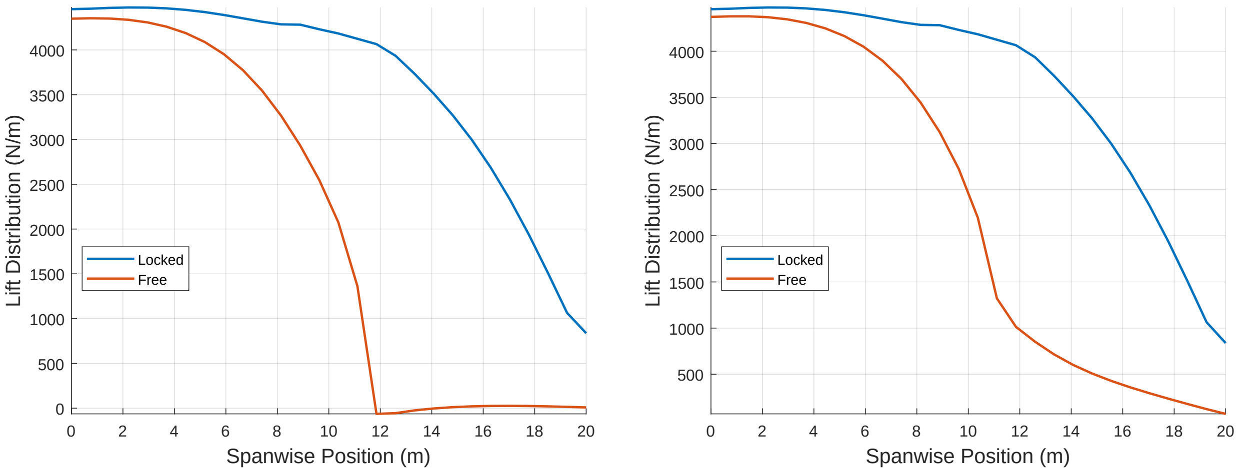

(a) 2° Flare **(b)** 5° Flare

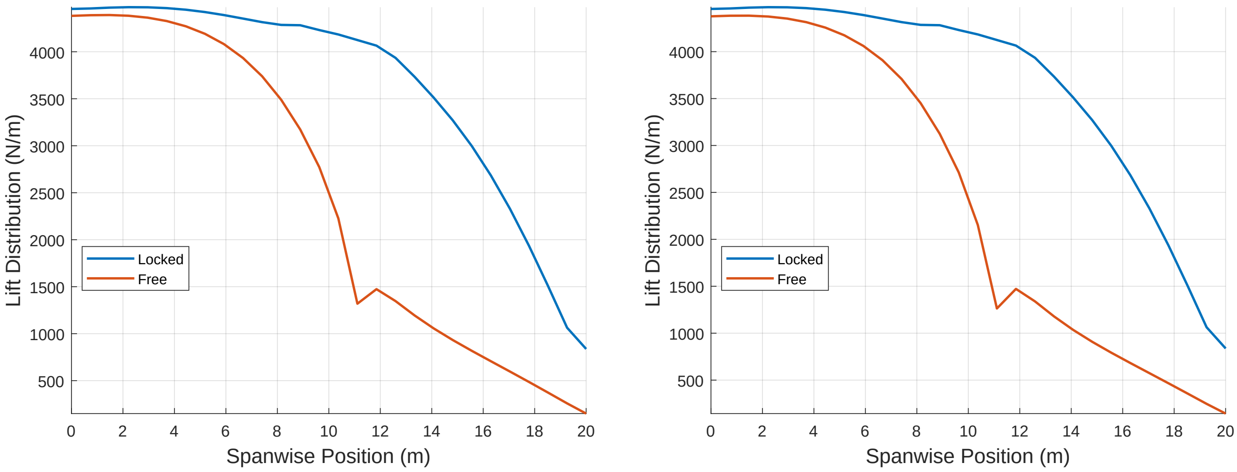

(c) 10° Flare **(d)** 15° Flare

Figure 5.10: Spanwise lift distribution at different flare angles

The lift distributions presented in Figure 5.10 can be linked to the fold angles achieved at static equilibrium, as shown in Figure 5.11. All the locked cases show the same lift distribution, however, with an unlocked hinge, it is clear that the lift distribution is affected by the flare angle. This is due to the fold angles being achieved by the FFWT at these different flare angles. Lower fold angles in the FFWT are achieved due to a greater reduction in the local angle of attack caused by the flare, which in turn results in higher lift values on the FFWT.

As previously discussed, higher flare angles lead to increased local rotational stiffness at the hinge point. This occurs because the bending moment acting on the hinge is divided into multiple sub-components, effectively limiting the extent of folding. Consequently, FFWT at higher flare angles exhibits lower fold angles, which in turn affect the lift distribution as seen in Figure 5.10.

An additional aspect to consider is the irregularity in the lift distribution for the locked configuration. This irregularity arises from the spanwise panel discretisation, which, in a multibody system, results in a discontinuity at the hinge location due to the FFWT's panel arrangement. To mitigate this issue and obtain a smoother lift distribution, a moving average interpolation is applied.

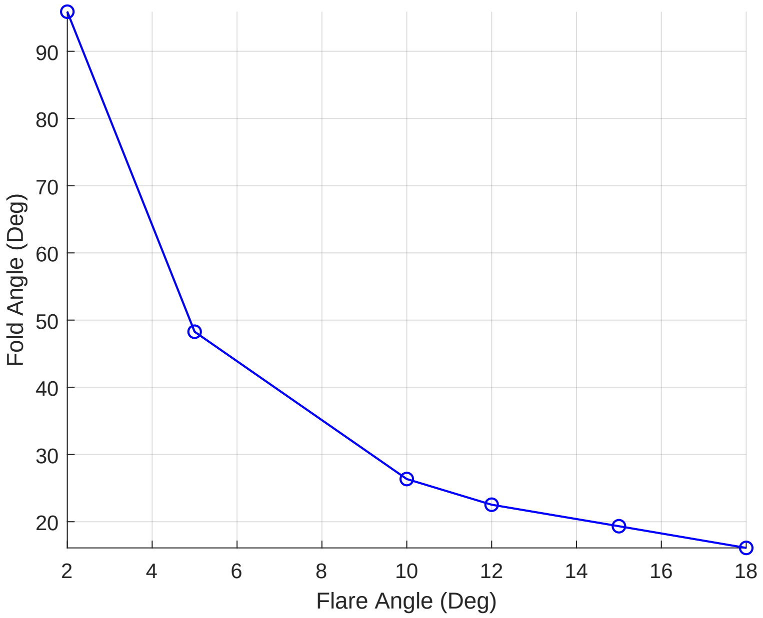

Figure 5.11: Fold angles achieved with different flare angles

Figure 5.11 illustrates the relationship between the fold angle and the increasing flare angle. The FFWT (Flared Folding Wing-Tip) achieves higher fold angles, directly contributing to the overall lift distribution. As shown in Figure 5.10a, the folding wing-tip does not generate any lift in its near-vertical orientation. This lack of lift can be directly attributed to the orientation of the wing-tip, which becomes nearly perpendicular to the aerodynamic forces acting upon it.

Smaller flare angles result in very high fold angles. For example, at a 2-degree flare angle, the fold angle reaches 95 degrees, indicating that the FFWT folds slightly inwards. Interestingly, these smaller flare angles also exhibit bi-stable behaviour once the flow velocity generates sufficient lift on the FFWT. This means the system can settle into two different static equilibrium states, which is linked to the high fold angles achieved at lower flare settings. At these high fold angles, the system can theoretically be stable at both +90 degrees and -90 degrees.

In addition, numerical factors such as residual tolerances in the solver could contribute to these equilibrium solutions. The tolerances are defined separately for displacements, rotations, and Lagrange multipliers in the non-linear static solver in PROTEUS. However, the FFWT experiences larger rotations compared to the inner wing, particularly at lower flare angles, which causes convergence issues. This can ultimately lead to equilibrium solutions that may not physically occur but are a numerically viable solution. For instance, at a 95-degree fold angle, approximately 33% of the FFWT generates negative lift, while the remaining 66% produces small amounts of positive lift, as shown in Figure 5.10a. The negative lift near the hinge is expected due to the reversed orientation of the wetted surface.

Another explanation for the behaviour near 0-degree flares arises from the possible poor conditioning of the tangent stiffness matrix, the stiffness of the structure especially around the hinge is reduced and given the Newton-Raphson method relies on the linearisation (via the tangent stiffness matrix) of the equilibrium equation, lower stiffness has a direct consequence on the quality of the tangent matrix. Furthermore, the high local rotations increase the non-linearity of the system which may further challenge the solver finding a good solution. Reducing the step size can be considered a possible solution, however, reduced flow velocity results in a drooping FFWT, producing no lift, which can lead to poor conditioning of the external load stiffness matrix.

6 Dynamic Results

The dynamic solver developed by Werter (2017) [51] employs a monolithic approach to solving the coupled aeroelastic system, integrating both structural dynamics and unsteady aerodynamics into a unified framework. As described in Section 4.3, this solver captures the interaction between the wing's structural flexibility and the aerodynamic loads over time. The approach is based on linearising the equations of motion around the non-linear static equilibrium of the system, allowing it to efficiently handle small perturbations and predict dynamic responses to external disturbances.

In this study, the solver is used to evaluate the wing's dynamic response to prescribed gust inputs, specifically a 1-cosine gust profile with varying half-lengths. This gust shape is widely used in aeroelastic analyses to simulate transient aerodynamic loading, as required by the CS-25 certification standards. The dynamic response is analysed for three distinct hinge configurations, each representing a different operational state of the folding wing tip.

1. **Locked-Locked:** In this configuration, the hinge remains locked throughout the entire timespan. The wing behaves as a continuous, rigid structure during the gust encounter, with no relative motion between the main wing and the wing tip. This case serves as the baseline for comparison, representing the most rigid and stable scenario.

2. **Free-Free:** Here, the hinge remains completely unlocked for the entire duration of the simulation, allowing the wing tip to rotate freely relative to the main wing. The static equilibrium around which the dynamic solution is linearised corresponds to this fully released state. This configuration helps to understand the impact of a free hinge on the wing's dynamic stability and structural response during gust encounters.

3. **Locked-Free:** In this scenario, the hinge is initially locked but is then unlocked at specific moments during the gust encounter to simulate an in-flight deployment or release of the wing tip. The unlocking time is varied to analyse how the timing of the hinge release influences the wing tip's dynamic displacement and the overall wing response to gust loads. This case highlights the transient effects and the potential risks associated with unlocking the hinge under dynamic loading conditions.

   However, it is important to note that the accuracy of this model may be limited due to the inherent assumptions in the state-space formulation. The dynamic solver relies on linearising the system around a static equilibrium point, which assumes small perturbations from that equilibrium. When the hinge is unlocked mid-gust, the resulting large deformations and abrupt changes in the system's configuration can cause significant deviations from the assumptions underlying the linearised approach. As such, the predicted response may not fully capture the true non-linear behaviour of the system during and after the unlocking event. This limitation should be taken into account when interpreting the results for this configuration, as it represents a more complex dynamic scenario which may not be captured accurately with linear tools.

These three configurations are chosen to cover a wide range of possible in-flight scenarios, from a fully rigid wing tip to a dynamically released one. The results provide insight into how different hinge states influence the aeroelastic stability and performance of the wing under unsteady aerodynamic loading. The comparison between the locked and unlocked cases is particularly valuable for understanding the potential benefits and challenges of incorporating folding wing tips in modern aircraft designs.

6.1. Free-Free

The free-free configuration refers to the state of the wing when the hinge at the wing tip remains unlocked, allowing the hinged section to rotate freely about its axis. The state-space system developed for this case is based on the wing's static equilibrium position, serving as the initial condition for the dynamic analysis. This configuration is critical for understanding the influence of aerodynamic loads and external disturbances, such as gusts, on the wing's structural response when the hinge is not locked from the beginning.

To evaluate the effects of various parameters on the wing's behaviour, simulations are conducted by varying key factors such as the angle of attack, gust length, and flare angle of the hinge axis. The resulting responses are then compared to the behaviour of the fully locked wing tip configuration to highlight the impact of the unlocked hinge. This comparison provides valuable insight into the wing's aeroelastic stability and sensitivity to external inputs in both free and constrained conditions.

6.1.1. Varying Gust Length

Table 6.1 summarises the set-up with varying gust lengths. A high angle of attack is chosen, following a gust profile similar to the CS-25 guidelines. Werter (2017)[51] uses four different gust lengths based on the mean chord of the airfoil (i.e. $5c, 10c, 20c$ & $50c$), which range from an extremely unsteady to a quasi-steady case. Following a similar approach, three half-gust lengths are chosen ranging from an unsteady to a quasi-steady case based on their reduced frequency calculated by adapting Equation 6.1. Where, k is the reduced frequency, b is the semi-chord length and V is the flow velocity. Quasi-steady aerodynamics are considered within a reduced frequency range of $0 \leq k \leq 0.05$, where $k = 0$ represents steady aerodynamics, and values above 0.05 indicate unsteady aerodynamics. Since the 25 m half-gust length case has $k = 0.076$, which exceeds the quasi-steady threshold of 0.05, providing a case for unsteady aerodynamic analysis. Lastly, for comparison, a flare angle of 10 degrees is used, while the effect of varying flare angles is examined in Subsection 6.1.2.

$$k = \frac{\omega b}{V} \tag{6.1}$$

Table 6.1: Configuration and load case definition for testing effects of Gust Lengths in for the Free-Free configuration

Flare	10 degrees
Velocity	75 m/s
Angle of Attack	5 degrees
Gust Amplitude	7.5 m/s
Half-gust Lengths	25 m, 50 m & 100 m
Corresponding Reduced Frequencies (k)	0.076, 0.039 & 0.020

Figure 6.1 plots the first five seconds of the gust-induced angle of attack, α, being tested. While the shortest gust provides more of an impulse load, the longest gust of 100 m disturbs the equilibrium over a longer period, hence the applied force is also distributed over a longer span.

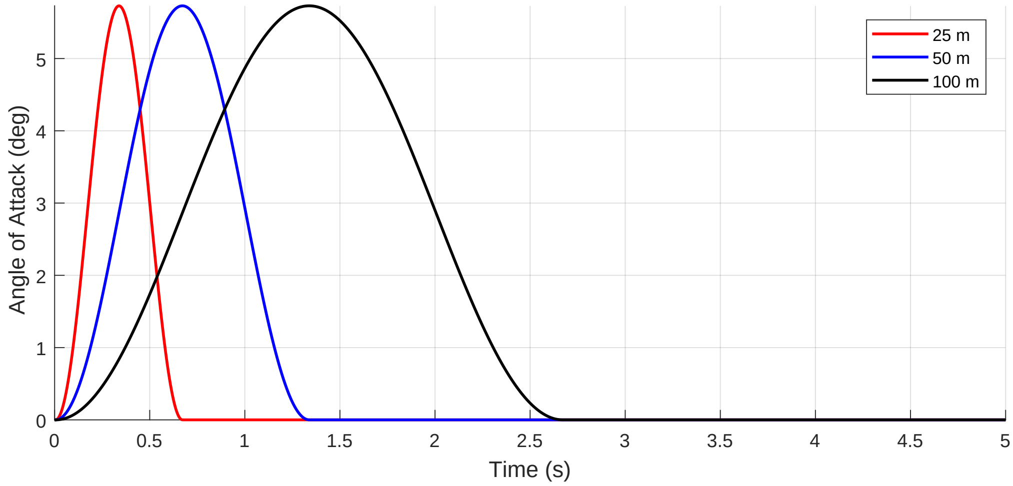

Figure 6.1: Gust-induced angle of attack with respect to time ($0s \leq t \leq 5s$)

Figure 6.2 shows the final state of the free-free folding wing tip and Figure 6.3 plots the change in wing tip displacement from the static equilibrium of the inner wing over time. Compared to the behaviour of the locked hinge, it is evident that the inner wing tip with the free FFWT does not reach the same deflection as the locked hinge. This is a direct consequence of the released hinge, as the moment arm is shortened. However, small oscillations occur after the first peak compared to the locked case, which dampens relatively quicker over time.

Shorter half-gust lengths of 25 and 50 meters are also tested, as shown in Figure 6.4a and Figure 6.4b, respectively. These shorter gust lengths introduce more pronounced aerodynamic unsteadiness, making them valuable for assessing how the wing responds to sudden aerodynamic changes. Each gust length corresponds to a different frequency, influencing the dynamic response of the wing. Depending on how these gust frequencies interact with the wing's structural eigenfrequencies, the response can vary significantly, potentially exciting different vibration modes and altering the overall aeroelastic behaviour.

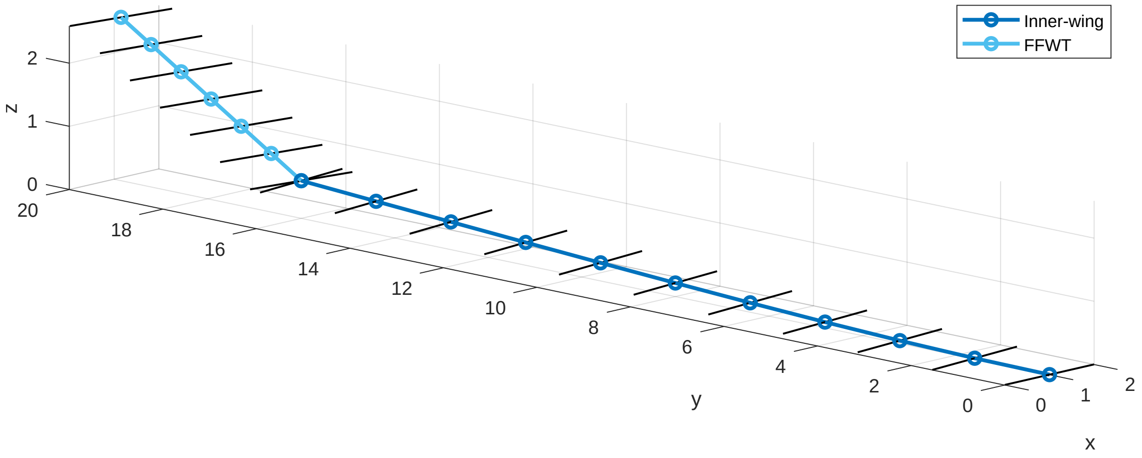

Figure 6.2: Wing deformation after a 100 m gust encounter

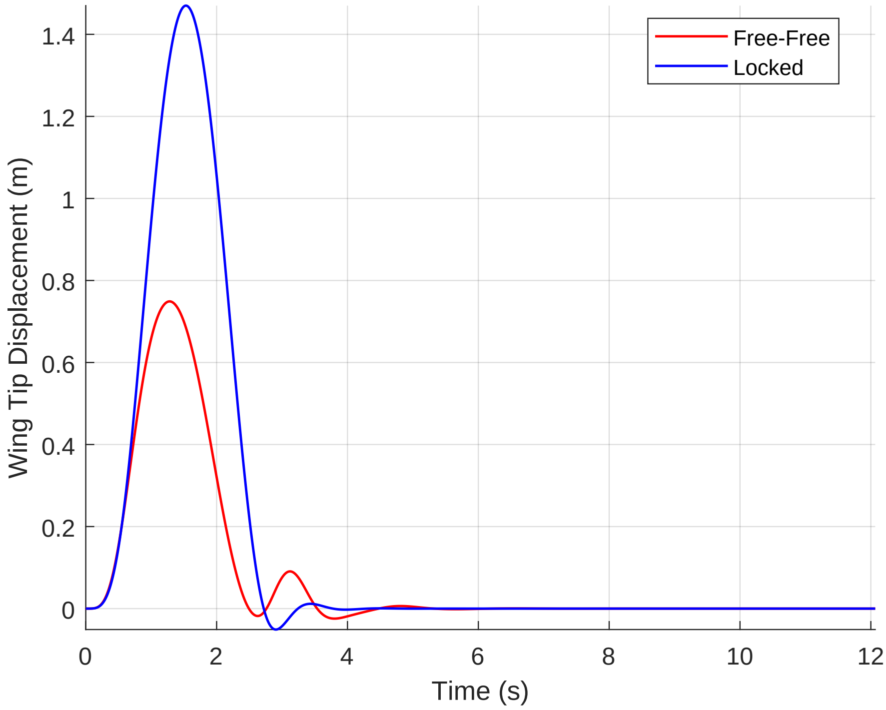

Figure 6.3: Wing tip Displacement for a Free-Free FFWT at 10 Degrees Flare in a gust of 100 m half-length

From Figure 6.3, it is found that as the gust lengths become shorter, the initial response of the inner wing tip seems to align more with the response of the locked wing configuration. Furthermore, it can be seen that the wing tip oscillates more over the timespan in the case of the shorter gusts. This is expected as the system is now being excited at a higher frequency, and with a free-floating mass, the inertial effects are translated to the inner wing tip. These plots also show that the damping is reduced with the free-free case as it takes longer for the oscillations to dissipate.

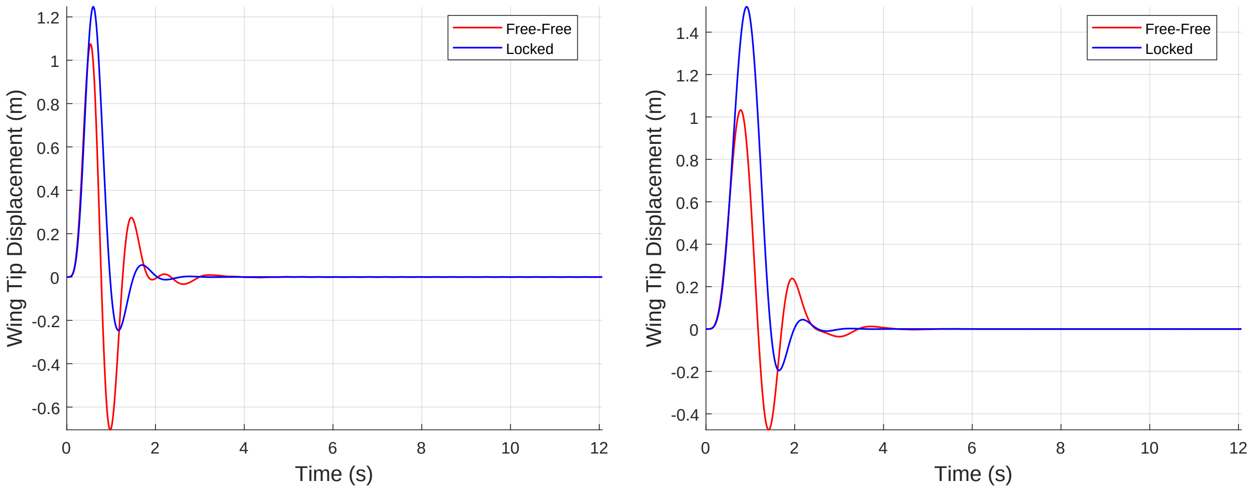

(a) Free-Free FFWT at 10 Degrees Flare in a gust of 25 m half-length.

(b) Free-Free FFWT at 10 Degrees Flare in a gust of 50 m half-length.

Figure 6.4: Comparison of Wing tip Displacement for a Free-Free FFWT at 10 Degrees Flare in different gust half-lengths.

Further insight can be gained from the tip displacement of the flared folding wing tip which is plotted in Figure 6.5. Focusing more on the oscillating behaviour of the wing tip, both the 25 m and 50 m half-gusts seem to create a larger transient displacement when compared to the 100 m gust. Based on the gust profile, this behaviour is expected since the aerodynamics are quasi-steady ($k = 0.020$) as compared to the sharper gusts. Another interesting observation here is the difference in maximum tip displacements reached by the 25 m and 50 m configurations. For the locked case, the inner wing-tip displacement is approximately 0.3 m higher for the 50 m gust case compared to the 25 m gust case. This difference arises because the 50 m gust results in a more quasi-steady aerodynamic loading, as indicated by its lower reduced frequency. Consequently, the wing and wing-tips deform more gradually over time compared to the 25 m gust, where the higher reduced frequency induces more unsteady effects. A similar peak displacement is observed for the 100 m gust case, following the same reasoning.

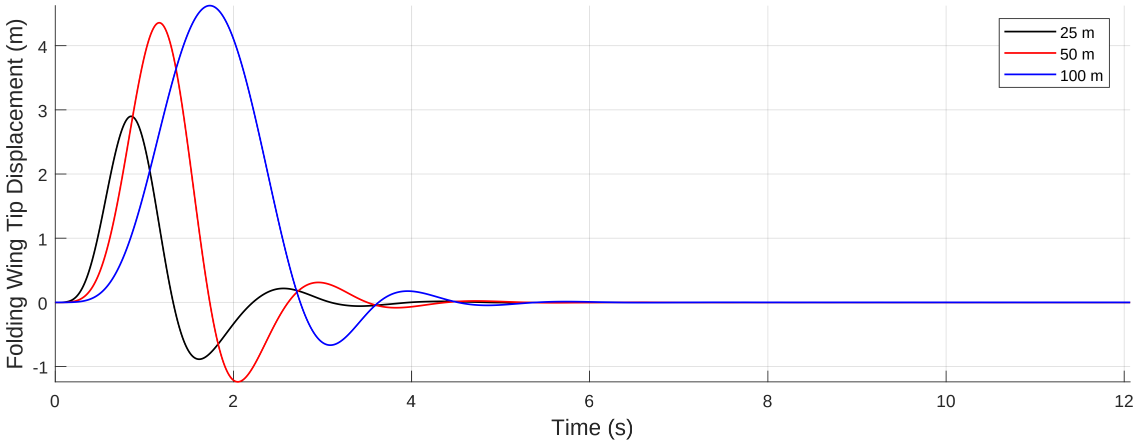

Figure 6.5: Folding Wing tip Displacement for a Free-Free FFWT at 10 Degrees Flare under all three gust profiles.

When compared in terms of the free hinge case, it can be seen that the maximum deflection of the inner wing tip is nearly the same. Co-relating this response with the tip deflections of the FFWT in Figure 6.5, a higher FFWT deflection is reached with the 100 m gust. Unlike the locked case, the FFWT rotates around its hinge axis upon the gust encounter, while the inner wing bends based on the forces produced by its effective lift surface. The 100 m gust represents the longest wavelength perturbation among the cases considered, meaning that the induced aerodynamic loading changes more gradually over time. Compared to shorter gust wavelengths, which introduce more rapid fluctuations and higher-frequency excitation, the 100 m gust imposes a relatively steady aerodynamic force. As a result, the FFWT undergoes a larger overall displacement, as the hinge mechanism accommodates the sustained aerodynamic moment more effectively than in cases with higher-frequency gusts, where inertia and dynamic coupling effects limit deflection.

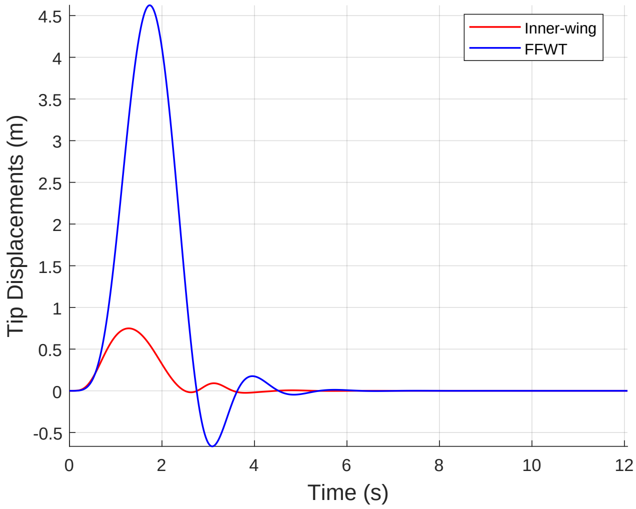

Figure 6.6: Superimposed displacements for the inner wing tip and the FFWT tip for 100 m gust length.

A deeper insight can be gained by plotting the displacements of both the inner wing tip and the FFWT tip together, revealing their coupled behaviour. As the gust impacts the wing, the free hinge allows the FFWT to rotate about its axis, resulting in a steep increase in its tip displacement, while the inner wing tip experiences comparatively less motion. Once the gust passes, oscillations are observed in both components. Notably, as the FFWT dips below its equilibrium position, the inner wing tip exhibits a slight upward motion, indicating dynamic coupling between the two. This interaction becomes more pronounced with shorter gusts, as seen in Figure 6.7, where the increased unsteadiness of the aerodynamic loading (higher reduced frequency) leads to stronger mutual influence between the FFWT and the inner wing.

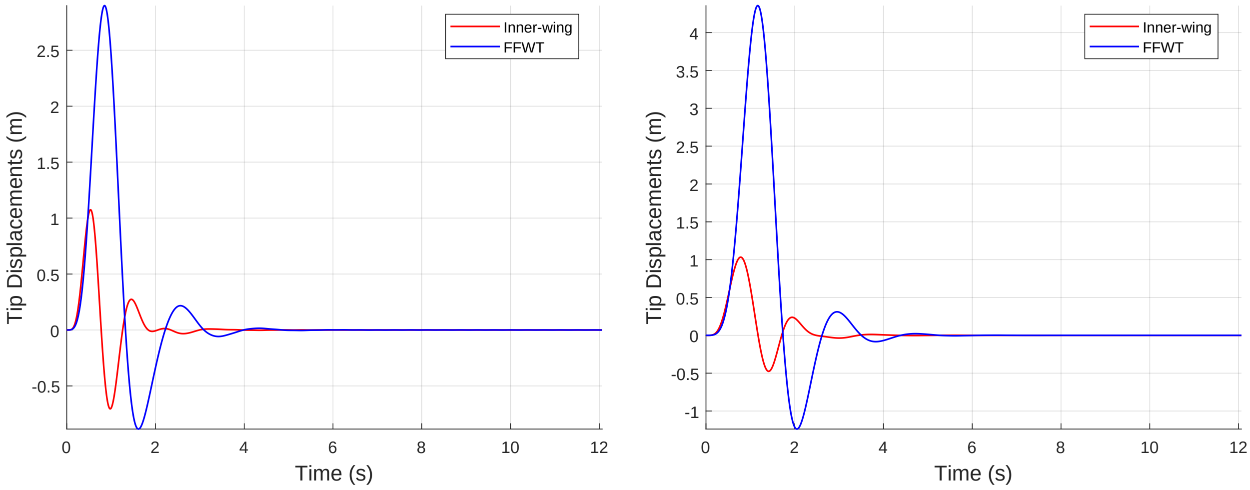

(a) Free-Free Tip displacements at 10 Degrees Flare in a gust of 25 m half-length.

(b) Free-Free Tip displacements at 10 Degrees Flare in a gust of 50 m half-length.

Figure 6.7: Superimposed tip displacements from static equilibrium for the inner wing tip and the FFWT tip for 25 m and 50 m gust lengths.

These oscillations also give rise to corresponding perturbations in the wing root bending moment (WRBM). Figure 6.8 plots the root bending moments. The WRBM follows the pattern of the inner wing tip displacement, as expected, because it directly responds to the aerodynamic loads and structural flexibility, influencing the bending moment distribution. Furthermore, the reduced WRBM must be noted in the case of the larger gusts of 50 and 100 meters. In the case of the 25 m gust, although the moment is reduced, the peak nearly coincides with that of the locked case and the behaviour after the gust passes is less damped as well.

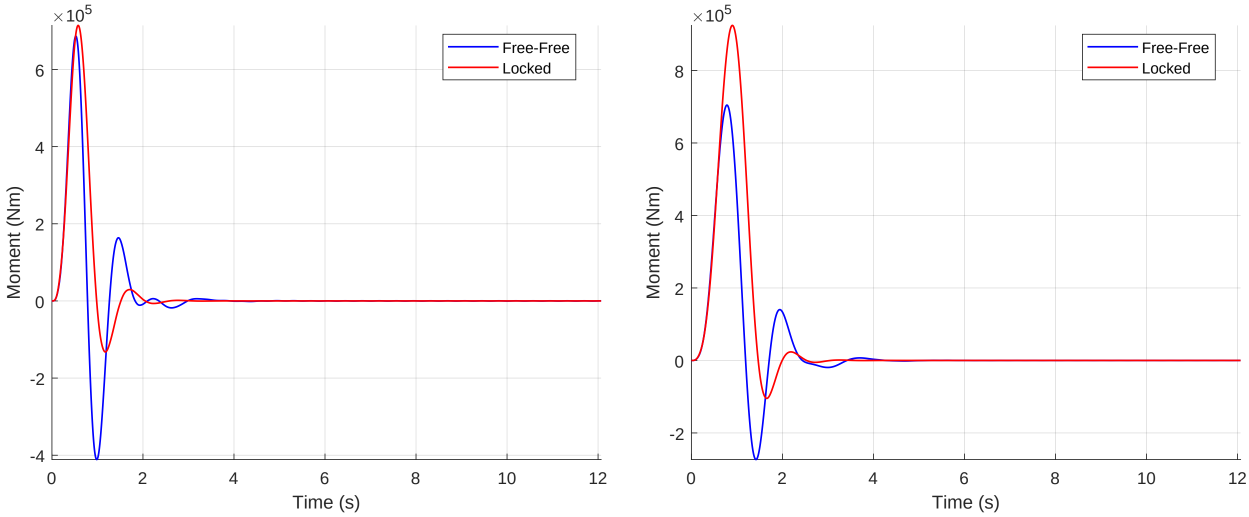

(a) WRBM for 25 m gust

(b) WRBM for 50 m gust

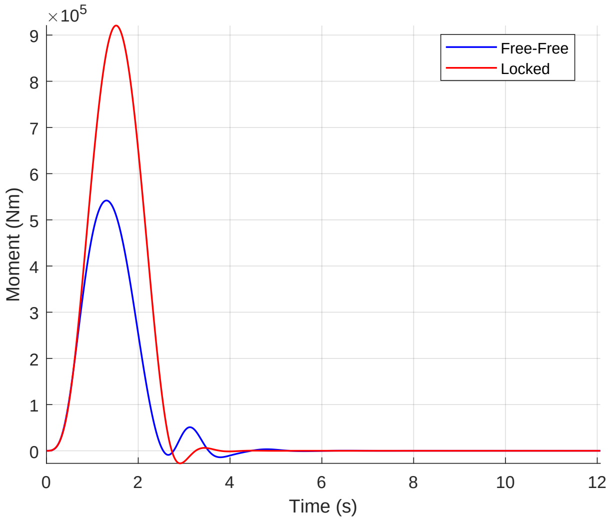

(c) WRBM for 100 m gust

Figure 6.8: WRBM plots for the different gust lengths.

The chordwise shear loads shown in Figure 6.9 illustrate the impact of gusts on shear forces. The trends in the shear plots resemble those observed in the root bending moment. For the shortest gust Figure 6.9a, the free hinge configuration exhibits a larger peak shear load compared to the locked configuration. Shear loads on the wing arise from the aerodynamic loading and the corresponding reactions to maintain equilibrium. Given the unsteady nature of the 25 m gust, a more dynamic response is achieved which results in larger deflections as seen in Figure 6.4a, which directly contributed to the peak shear load. Another possible reason for the peak can be attributed to the movement of the flared folding wing tip itself, as the high initial deflections cause loading which gets transferred to the root when a flare is present, further adding to the higher peak. In contrast, for longer gust durations (Figure 6.9b, Figure 6.9c), the peak shear loads are consistently lower for the free hinge case compared to the fully locked case.

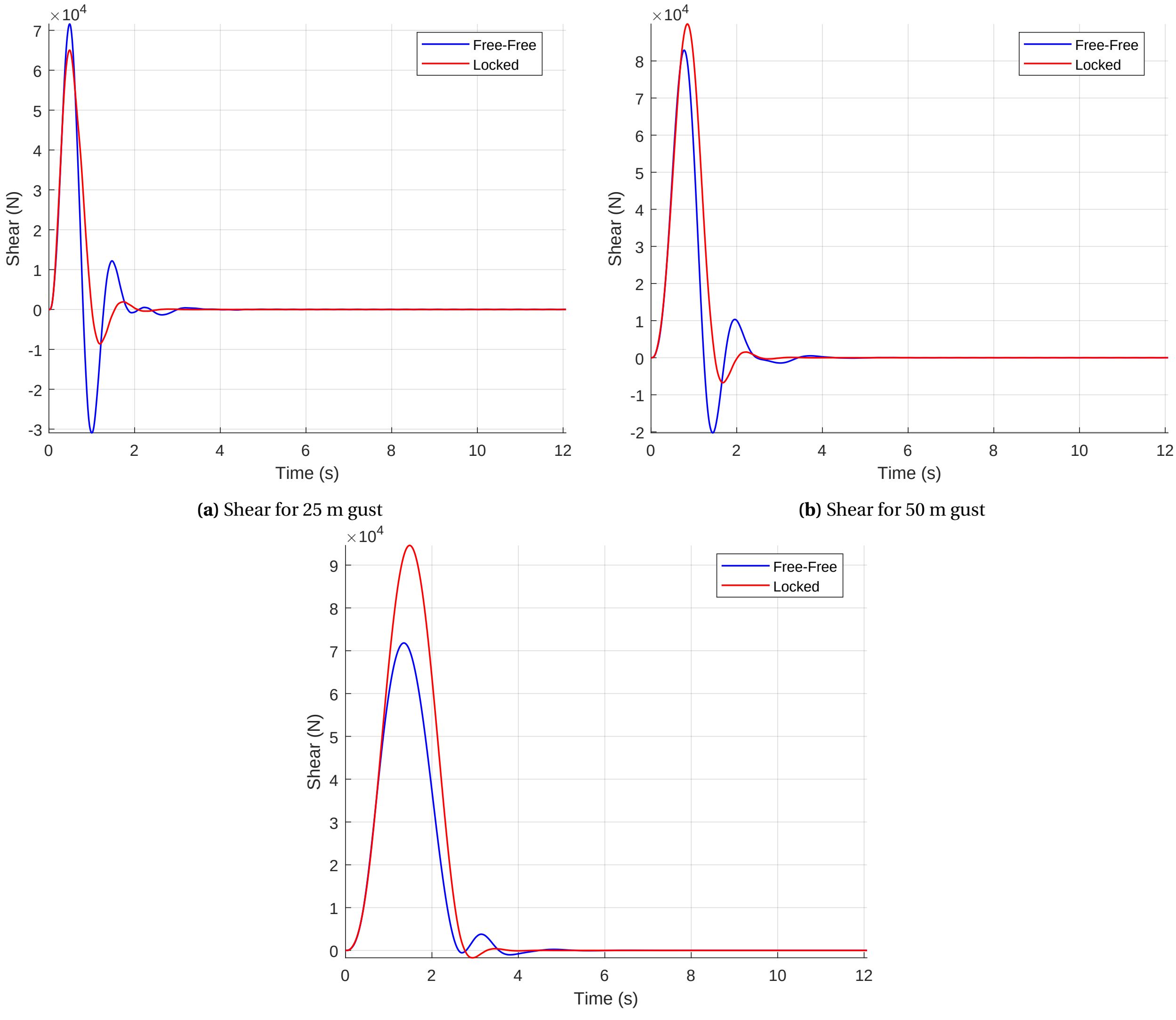

(a) Shear for 25 m gust

(b) Shear for 50 m gust

(c) Shear for 100 m gust

Figure 6.9: Root shear plots for the different gust lengths.

6.1.2. Varying Flare Angle

Figure 6.10 plots the time history of the wing tip displacement for a wing with a free hinge, subjected to $1-\cos$ gust profiles of varying lengths. The dynamic analysis is conducted from an equilibrium state where the hinge is already free. The plots depict the response of the wing tip for different flare angles of the hinge axis: 5°, 8°, 10°, 15°, and 18°.

In Figure 6.10a, the wing is subjected to a shorter gust with a half-length of 25 meters. The displacement exhibits significant oscillations immediately after the gust hits, with the amplitude gradually decaying over time. The initial oscillations are more pronounced due to the shorter gust length, which applies a sharp aerodynamic load on the wing. From the displacement plots, it is evident that as the flare angle increases, the oscillations increase over the timespan, which shows that perhaps increasing the flare reduces the damping.

In Figure 6.10b, the gust length has been extended to 50 meters. Similar to the 25-meter case, the wing tip displacement shows strong oscillations in the initial phase, but the oscillations are slightly less severe compared to the shorter gust. The increased gust length results in a smoother load application, leading to a more controlled dynamic response. The behaviour across different flare angles remains consistent with what was noted in the 25 m gust.

Figure 6.10c shows the wing being subjected to a much longer gust with a half-length of 100 meters. In this case, the aerodynamic load is applied more gradually, leading to a smoother and more stable initial response. However, an anomaly is observed for the 5-degree flare angle, where the wing tip exhibits erratic and unstable behaviour compared to the other cases. However, it should be noted that over the timespan, the 18-degree flare set-up takes longer to stop oscillating compared to the 5-degree case. This suggests that this anomalistic behaviour is limited to the initial excitation.

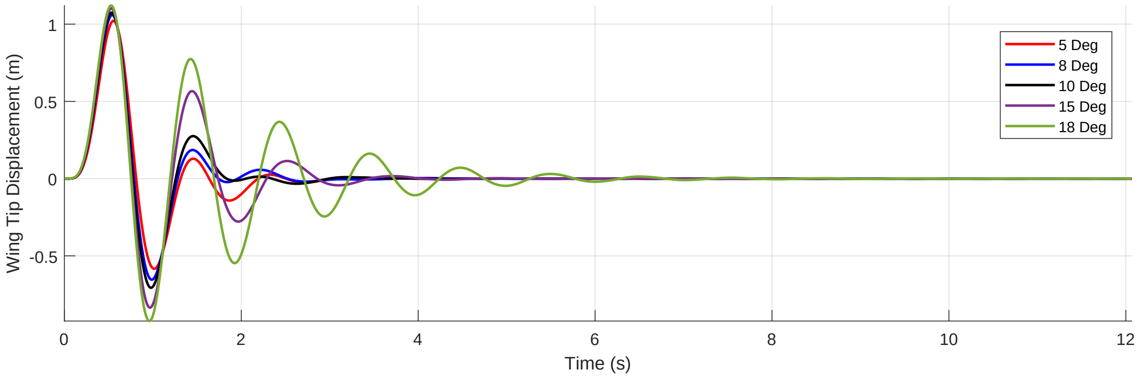

(a) Wing tip Displacement for different flare angles under a 25 m gust.

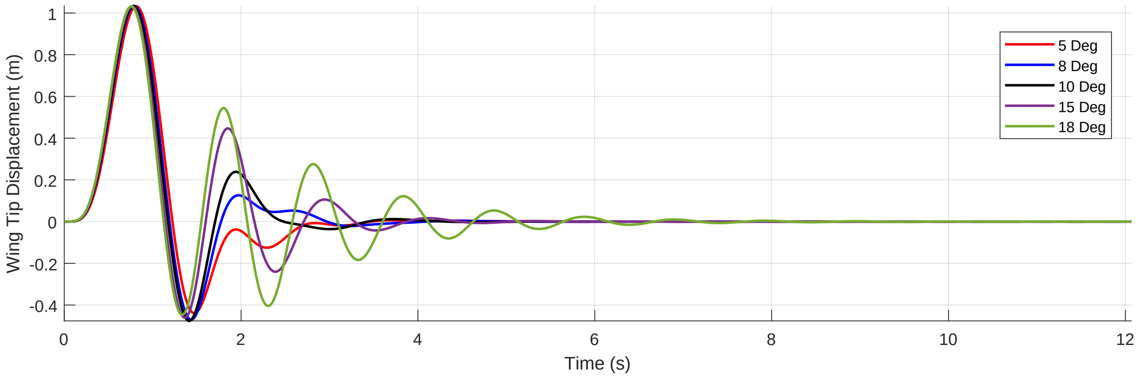

(b) Wing tip Displacement for different flare angles under a 50 m gust.

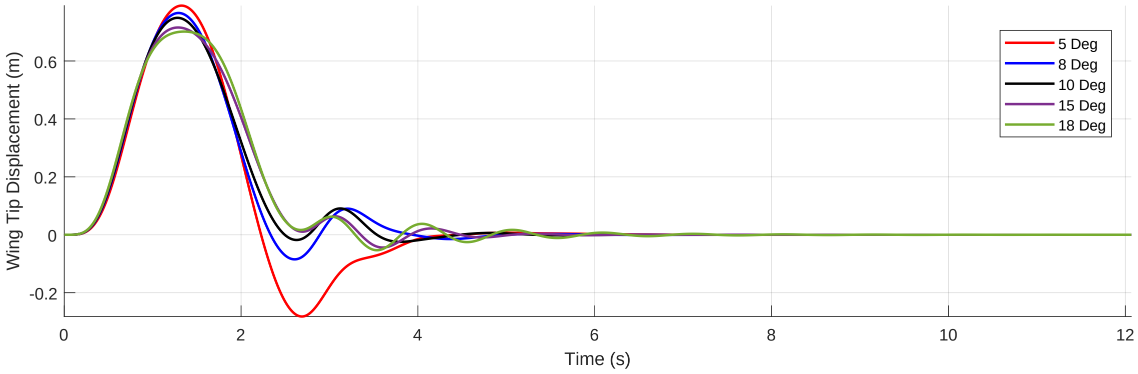

(c) Wing tip Displacement for different flare angles under a 100 m gust.

Figure 6.10: Wing tip Displacements from the static equilibrium for the Free-Free set-up for different flare angles ranging from 5 degrees to 18 degrees under half-gusts of 25 m, 50 m, and 100 m.

To better understand the variation in maximum and minimum displacements across different flare angles, plots Figure 6.11 can be examined. It is evident that for flare angles below 10 degrees, the minimum displacements are significantly larger compared to those at higher flare angles. Furthermore, as shown in Figure 6.11b, while the minimum displacement for the 5 and 8-degree flare cases is smaller than that of the locked 10-degree case, it remains significantly larger than for higher flare angles.

This behaviour can be attributed to the increased deformation of the FFWT at lower flare angles. As previously discussed, smaller flare angles correspond to larger fold angles, which influence the structural response of the wing. Under a 100 m gust, which represents a more steady aerodynamic loading condition, the motion of the FFWT may induce a downward displacement at the wing tip, contributing to the observed increase in minimum displacement.

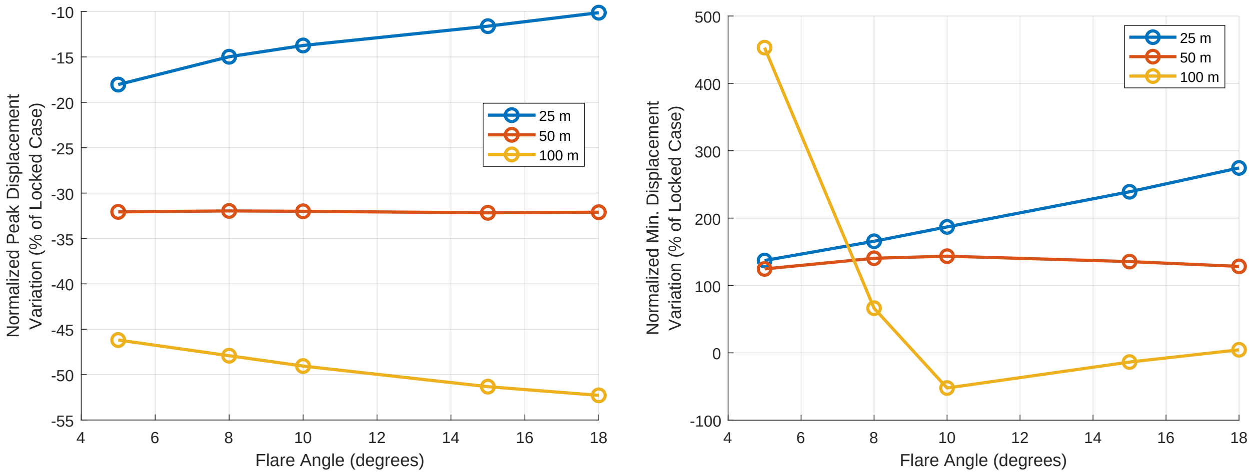

(a) Normalised maximum displacements as a percentage of minimum displacement of Locked-hinge case for different flares

(b) Normalised minimum displacements as a percentage of minimum displacement of Locked-hinge case for different flares

Figure 6.11: Normalised maximum and minimum wing tip displacements (as a percentage of Locked-hinge configuration) for varying flare angles

In order to study the persistence, the root-mean-square of the displacements is computed and plotted in Figure 6.12. Shorter gusts, as discussed in Subsection 6.1.1, introduce a more impulsive aerodynamic load on the wing, resulting in larger initial oscillations in the wing tip displacement. The increase in the oscillations with increasing flare angles is much more evident with the 25 m half gust length when compared to the other two cases, suggesting a more unsteady response. The relatively higher oscillation of the 18-degree flare case is also evident in the case of the 50 m gust, which points to reduced structural damping. This reduction may be led by higher load transfer between the FFWT and the inner wing. Lastly, the higher RMS values for the lower flare angles in the case of the 100 m gust can be explained by noting the initial displacement peak and drop observed in Figure 6.10c.

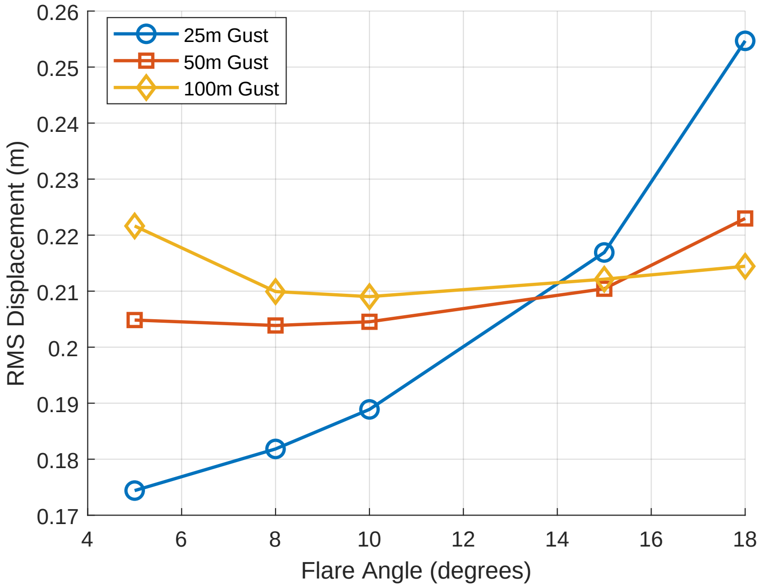

Figure 6.12: Displacement RMS for free hinge over different flare angles and three gust lengths

On the other hand, the RMS values from the wing tip displacements for the locked case are found to be 0.206, 0.307 and 0.419 for the 25 m, 50 m and 100 m half gust lengths respectively. Comparing the RMS of the free hinge with the locked hinge case, it can be seen that the RMS values for the 50 m and 100 m gusts are higher in the case of the locked hinge. However, the oscillations after the first peak dampen out faster with the locked case, hence the higher RMS values are attributed to the higher initial peak.

Lastly, PROTEUS solves an eigenvalue problem for the constrained system, considering only the stiffness and mass matrices. This allows for evaluating how closely the structural modes align with the gust frequencies, as shown in Figure 6.13. Notably, as the flare increases, the structural frequency (1.36 Hz) approaches that of the 25 m gust (1.5 Hz), explaining the observed oscillatory behaviour. Additionally, the structural frequency of the locked hinge case is found to be 1.39 Hz. This indicates that increasing the flare brings the structural frequency of the unlocked case closer to that of the locked case. This trend can be understood by referring to Figure 5.11, which shows that increasing the flare reduces the fold angle, leading to a mass distribution in the unlocked hinge case that increasingly resembles that of the locked hinge case.

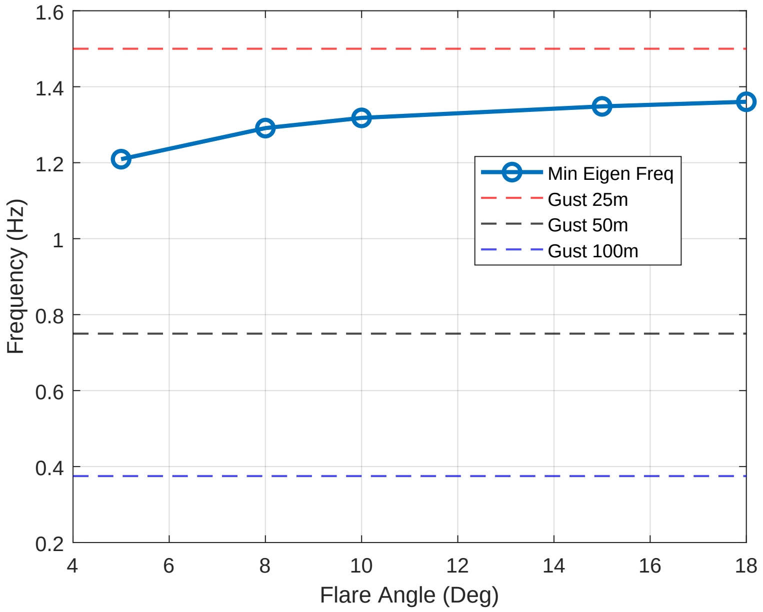

Figure 6.13: Minimum frequency from Eigenvalues compared to the gust frequencies

Finally, the effect of the flare on the bending moment and shear loads are presented in Figure 6.14 and Figure 6.15 respectively, which plot the maximum and minimum values achieved with respect to the locked case. The WRBM can be explained based on the patterns seen in the Figure 6.11, which largely co-relate. The 25 m unsteady aerodynamic load case shows an increasing trend in the peak WRBM with flare angle, which is expected due to the larger load transfer at higher flare angles. For all cases, the values are negative, suggesting that compared to the locked case the WRBM decreases. For the 100 m case, the maximum WRBM decreases, which is expected due to the more steady aerodynamic loading. However, minimum WRBM shows an increase in the minimum WRBM for the 5 and 8-degree flares, which follows the same reasoning as the patterns exhibited in the displacement curves.

Conversely, the shear force distributions exhibit an inverse trend compared to the WRBM plots. Lower flare angles correspond to higher peak shear loads, with a slight increase also observed between 15 and 18 degrees for the more unsteady gust cases of 25 m and 50 m. For the 100 m gust case, the minimum shear follows a smoother trend, whereas the maximum shear exhibits a pronounced peak relative to all other cases. This behaviour can be attributed to the motion of the FFWT but may also indicate constraint drift or ill-conditioned system matrices with an absence of a specialised time-integration scheme. Smaller flare angles are expected to exhibit more chaotic behaviour, potentially leading to error accumulation. As a result, the system may become increasingly sensitive to numerical inaccuracies, further amplifying deviations in the solution.

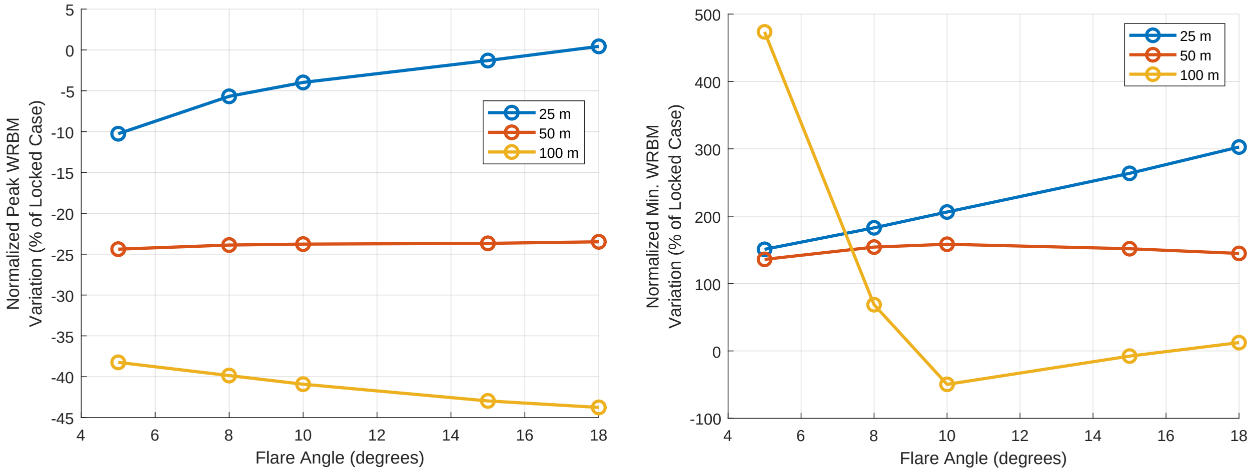

(a) Normalised maximum WRBM as a percentage of minimum WRBM of Locked-hinge case for different flares

(b) Normalised minimum WRBM as a percentage of minimum WRBM of Locked-hinge case for different flares

Figure 6.14: Normalised maximum and minimum WRBM (as a percentage of Locked-hinge configuration) for varying flare angles

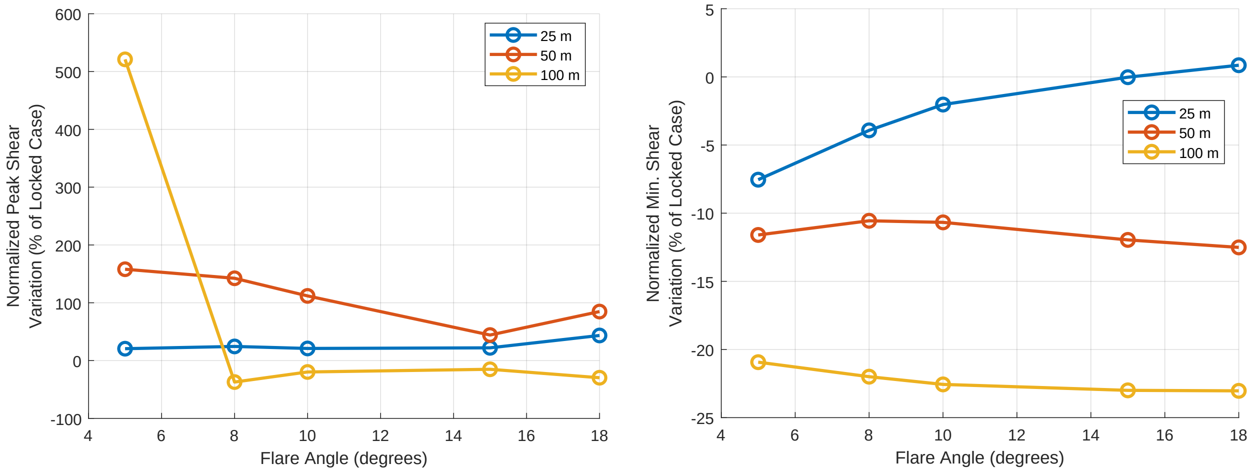

(a) Normalised maximum root shear as a percentage of minimum root shear of Locked-hinge case for different flares

(b) Normalised minimum root shear as a percentage of minimum root shear of Locked-hinge case for different flares

Figure 6.15: Normalised maximum and minimum root shear (as a percentage of Locked-hinge configuration) for varying flare angles

6.2. Locked-Free

The last section presented the results for a free-hinge case, hence the dynamic solver used the same state-space formulation from the beginning to the end of the simulation. This section focuses on testing and presenting the results obtained from the Locked-Free dynamic solver. As presented in Section 4.4, the state-space system for this case is constructed by combining two state-space systems from the locked static equilibrium: one with the hinge locked and the other with the hinge unlocked. Coupling these two states can lead to various numerical errors; therefore, this section begins with a solver validation exercise. Following this, the behaviour of the wing is analysed under different flare configurations and varying gust lengths. The calculated forces are also examined, and their behaviour is discussed. Finally, the impact of unlocking the hinge at different moments during the gust is investigated.

6.2.1. Correlation of Static and Final Dynamic Responses

After the gust has passed, the wing is expected to settle into the static equilibrium position corresponding to the unlocked hinge configuration. This behaviour can serve as a validity check for the model by comparing the wing tip displacements between the static and dynamic cases. A close match would confirm the model's accuracy in capturing the system's static and dynamic behaviour.

Figure 6.16 plots the drop in wing tip displacement achieved from the locked-free dynamic solver and the corresponding difference calculated from the static equilibriums. The largest deviation of 22.6% is found to be for the smallest flare of 2 degrees. The rest of the flare angles conform to a deviation lower than 15%. The diverging nature closer to lower flare angles can be explained by the higher fold angles and the consequent linearised nature of the solver. Following the explanation in Section 5.3, the fold angle reduces with the higher flare angle, which may help explain the convergence, as the perturbations become smaller. As shown in Figure 5.11, lower flare angles exhibit larger fold angles, which for a 4 m wide folding wing tip causes significant deviation of the mass distribution as well as the stiffness from the initialising locked case. This deviation explains the increasing difference with the decreasing flare angles.

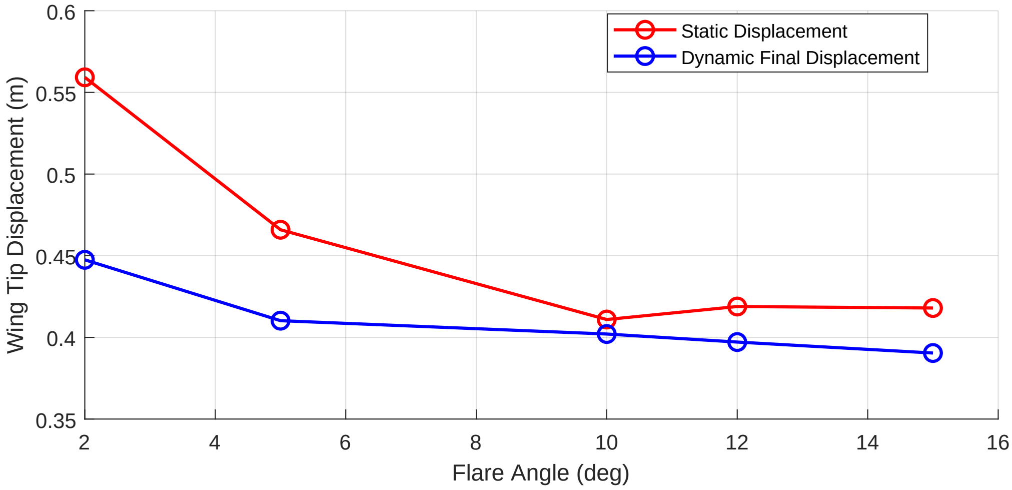

Figure 6.16: Flare angle vs wing tip displacement from locked to unlocked from static solution and converged dynamic solution

6.2.2. Varying Gust Length

The effect of different gust lengths can be analysed for various flare angles. To enable a meaningful comparison with the free-free hinge case, the same set-up is used, as shown in Table 6.1. The position of the wing at the hinge-release point is illustrated in Figure 6.17, which shows the response of the wing subjected to a 50 m gust with a flare angle of 10 degrees. Initially, the wing rises approximately 1.5 m from its locked steady state as shown in the figure before the hinge is unlocked, which causes the inner wing tip to drop. Figure 6.17 presents the variation in wing tip displacement from the initial steady state over time. To ensure comparable state-change onsets, the release time is intentionally set to occur relatively early.

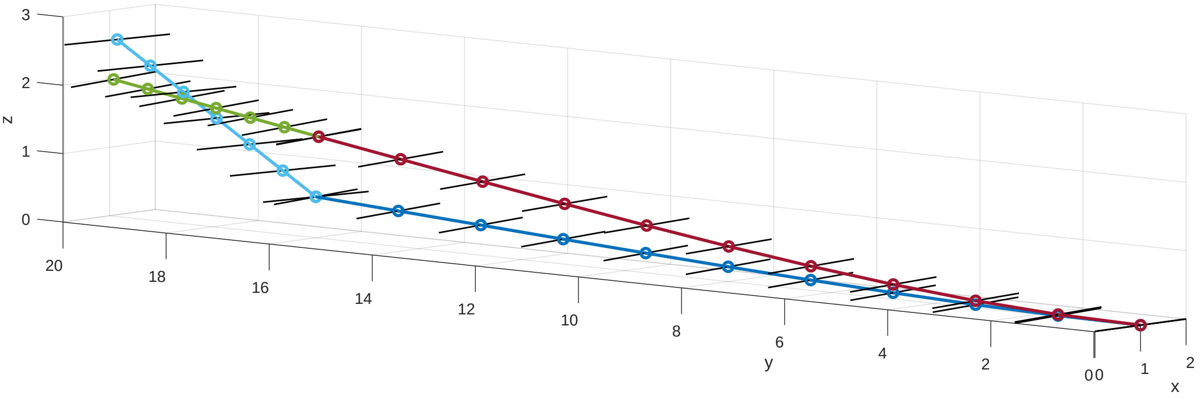

Figure 6.17: Release Time vs Final Deformation Plot

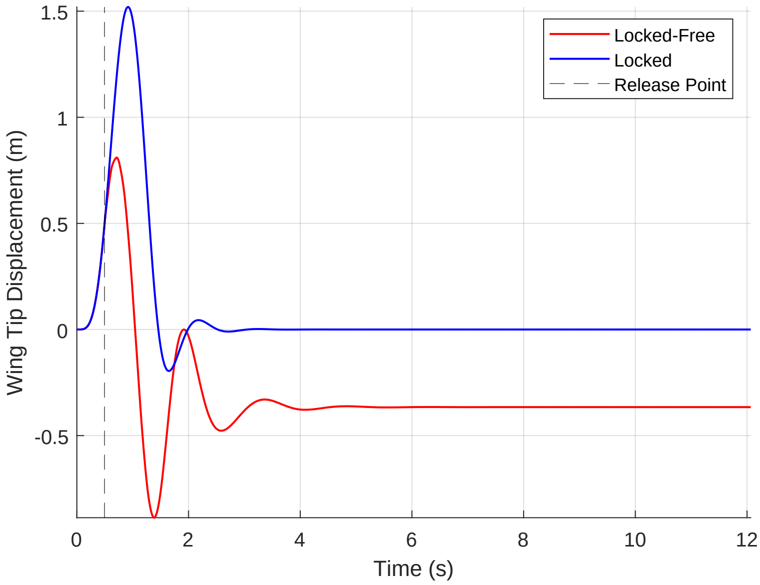

Figure 6.18: Wing tip Displacement for a Locked-Free FFWT at 10 Degrees Flare in a gust of 50 m half-length

The response to the 50 m gust case is shown in Figure 6.18. It can be observed that the release point does not exhibit significant discontinuity. Instead, the wing tip continues to rise but reaches a lower maximum compared to the fully locked case. Additionally, the wing tip begins to drop earlier than in the locked case and exhibits larger oscillations, likely due to the high accelerations experienced when the hinge is released. This sudden change in the system causes prolonged oscillations, with the system taking approximately 1.5 seconds longer than the locked case to stabilise. Similar trends are found in the numerical and experimental study performed by Córcoles et al. (2022) [49].

Figure 6.19 compares the responses for gust lengths of 25 and 100 meters. The effect of the release point varies depending on the gust profile over time. For instance, in the 100 meter gust case, the wing tip initially drops for a few milliseconds before the gust forces it to rise, followed by a drop-off. Conversely, in the 25 meter gust case, the wing tip drops more abruptly before settling into its new equilibrium.

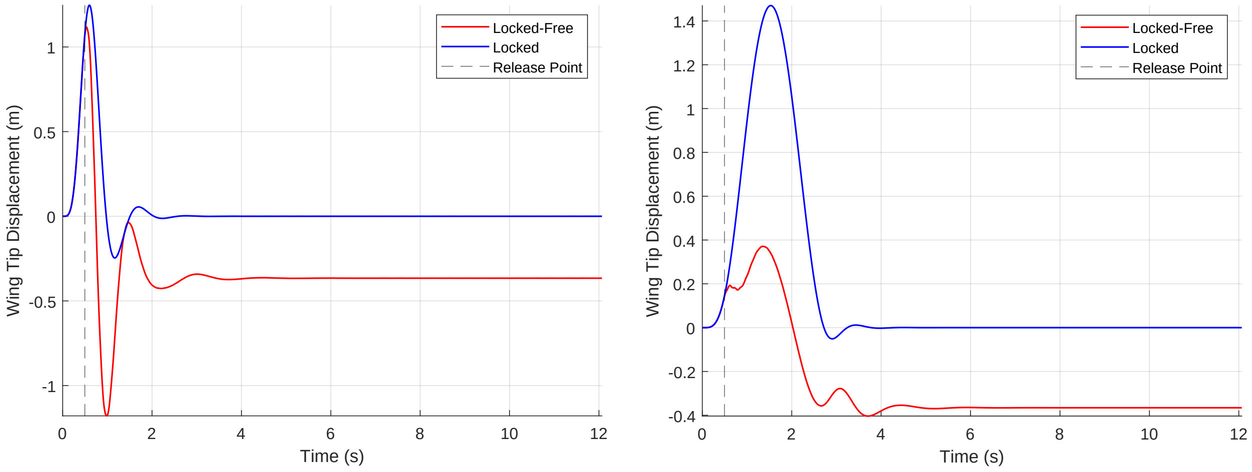

(a) Locked-Free FFWT at 10 Degrees Flare in a gust of 25 m half-length.

(b) Locked-Free FFWT at 10 Degrees Flare in a gust of 100 m half-length.

Figure 6.19: Comparison of wing tip displacement for a Locked-Free FFWT at 10 degrees Flare in different gust half-lengths.

Figure 6.20 illustrates the tip displacement of the folding wing tip under three gust scenarios: 25 m, 50 m, and 100 m. Notably, the final tip displacement for all cases converges to approximately 1.3 m, corresponding to the difference in final wing tip positions predicted by the static solutions. For the 25 m gust scenario, the wing tip displacement shows a sharper initial drop, followed by rapid oscillations that dampen over time. In contrast, the 50 m gust scenario exhibits a smoother rise to a peak before undergoing oscillations that stabilise slightly later. The 100 m gust case demonstrates a larger peak displacement and more sustained oscillations before converging to the final equilibrium. The differences in response are indicative of the varying aerodynamic loads imposed by the gust lengths. The responses are quite different compared to the free-free case, where the largest gust results in peak tip displacement shown in Figure 6.5, and highlights the change in dynamics due to the release.

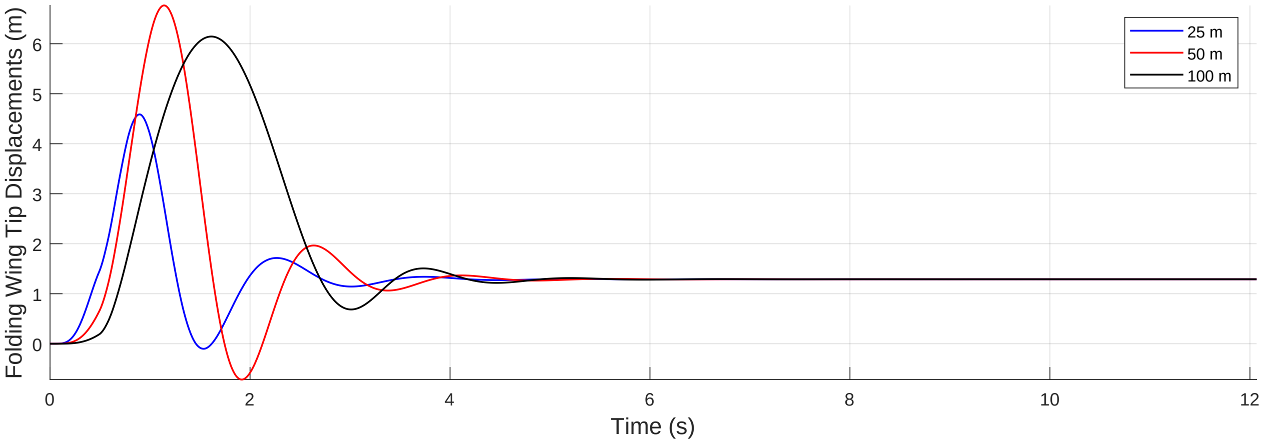

Figure 6.20: Folding wing tip displacement for a Locked-Free FFWT at 10 degrees Flare under all three gust profiles.

6.2.3. Varying Flare Angle

As studied in the static section, increasing the flare angle slightly reduced the wing's damping while slightly increasing the wing root bending moment. The effect of the flare angle under dynamic gust loads is explored in this subsection. Figure 6.21 presents the wing tip displacements for configurations with different flare angles subjected to half-gust lengths of 25, 50, and 100 meters.

For the 25 m half-gust length (Figure 6.21a), the wing tip displacements show a clear trend: as the flare angle increases, the oscillation amplitudes also increase. The increase is especially pronounced when the flare angle rises from 15° to 18°. For smaller flare angles (5°, 8°, and 10°), the oscillations settle into steady-state behaviour more quickly, indicating better damping characteristics.

The 50 m case (Figure 6.21b) follows a similar pattern, with oscillation amplitudes increasing as the flare angle grows. However, the peak displacements are slightly larger compared to the 25 m gust due to the wing tip flexing further into the gust peak. The effects of higher flare angles (15° and 18°) are still more pronounced, both in terms of amplitude and the time required for the oscillations to stabilise.

The trend is consistent for the 100 m half-gust (Figure 6.21c), but the impact of the flare angle is less significant. Larger flare angles result in much greater initial oscillation amplitudes, but the following dissipation is much quicker. Notably, the 5 degree configuration shows sharp initial peaks followed by relatively prolonged oscillations with higher amplitudes compared to the other flare angles. This behaviour is localised in the folding wing tip rather than the inner wing. This can be attributed to two contributing factors. First, the reduced effect of the flare at smaller angles diminishes its stabilizing influence on the folding wing tip, making it more susceptible to dynamic loads. Second, the nature of the gust at this length interacts differently with the wing, potentially exciting modes of oscillation that are less damped for lower flare angles. Increasing the flare not only reduces the local angle of attack but also splits the local hinge moment into two components, which enhances the stability of the folding wing tip. In contrast, lower flare angles are inherently more unstable for the folding wing tip because the absence of this stabilising effect allows for larger oscillatory responses.

In the first two cases, it is evident that as the flare angle increases, the oscillations in the inner wing become more pronounced. This general increase in oscillations can be attributed to the growing unsteady nature of the load case, where the dynamic response is amplified by the aerodynamic forces acting on the system. Additionally, the higher amplitudes observed in the 50 meter half-gust length can be partially explained by the timing of the hinge release, which introduces a more abrupt dynamic effect. For the 18 degree flare configuration, the higher oscillations and reduced apparent damping are primarily due to the increased stiffness of the system. With a larger torsional moment generated at the hinge due to the larger flare angle, greater moment transfer occurs between the folding wing tip and the inner wing, resulting in amplified oscillatory behaviour in the inner wing structure.

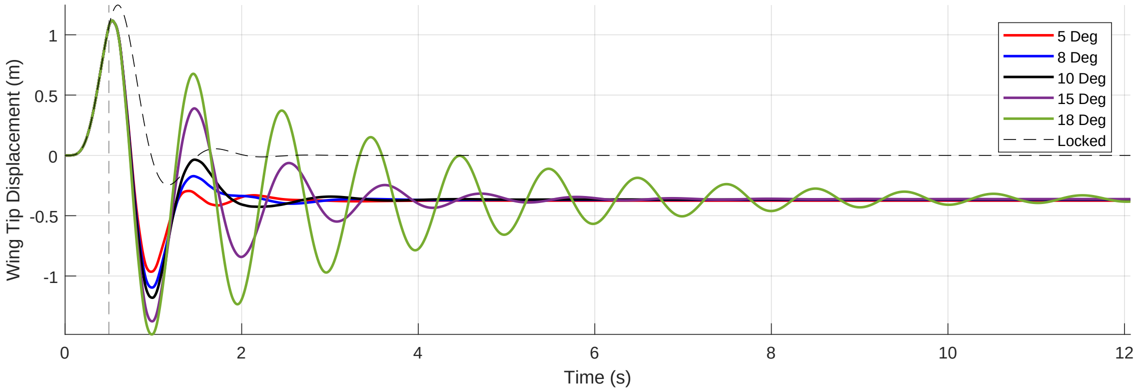

(a) Wing tip displacement for different flare angles under a 25 m half-gust.

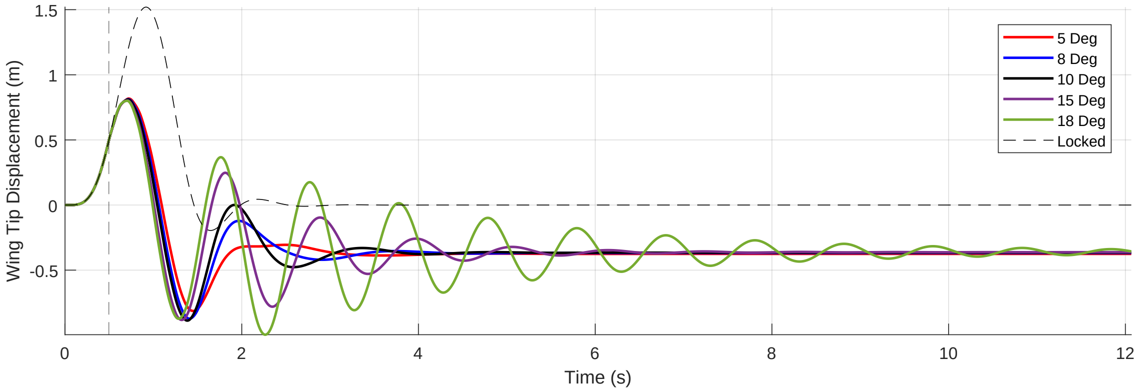

(b) Wing tip displacement for different flare angles under a 50 m half-gust.

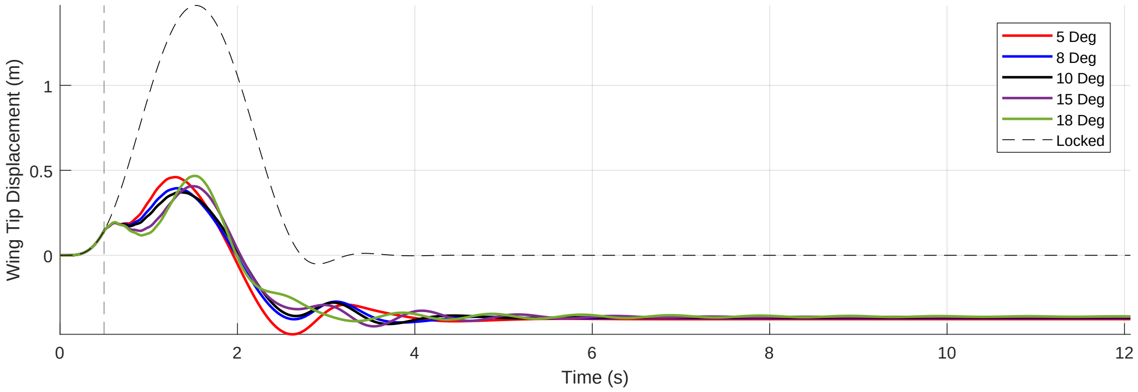

(c) Wing tip displacement for different flare angles under a 100 m half-gust.

Figure 6.21: Wing tip displacements for different flare angles ranging from 5 degrees to 18 degrees under half-gust lengths of 25 m, 50 m, and 100 m.

6.2.4. Varying Release Time

The release point of the flared folding wing tip is varied across different gust profiles to investigate how the timing of the hinge unlocking affects the dynamic response of the wing. The half-gust lengths considered for this study are 25 m, 50 m, and 100 m. For each gust length, the wing tip is initially locked and then released at different moments during the gust encounter to assess the influence of release timing on the wing tip displacement and its oscillations. The hinge release is tested at the peak of the gust loads — when the aerodynamic disturbance is at its maximum — as well as immediately after the peak, during the descending phase of the gust. These cases are of interest as they represent scenarios where the wing experiences abrupt aerodynamic changes, potentially leading to distinct dynamic behaviours. By comparing these results, the effects of early, peak, and delayed releases on the wing's response can be better understood, providing insight into the timing sensitivity of the folding wing tip mechanism.

In comparison to Figure 6.21, where the hinge is free from the start of the gust encounter, in Figure 6.22 the hinge is unlocked at a later stage, specifically after the peak wing tip displacement has already occurred. This change in the release timing introduces significant variations in the dynamic response, particularly in how quickly the system stabilises after the gust impact. For shorter gusts, it is observed that releasing the hinge after the peak displacement results in a quicker dissipation of oscillations, as the wing tip is already closer to its final equilibrium position. The wing tip experiences smaller subsequent deflections after the release, which reduces the overall energy in the system and helps the structure settle more efficiently.

Additionally, attention should be drawn to the discontinuous profile of the displacements as the flare is reduced in Figure 6.22c. This behaviour of the wing tip can be attributed to the greater fold angles and the increasing deviation of the structure's displacement from the mass distribution and stiffness about which it is linearised.

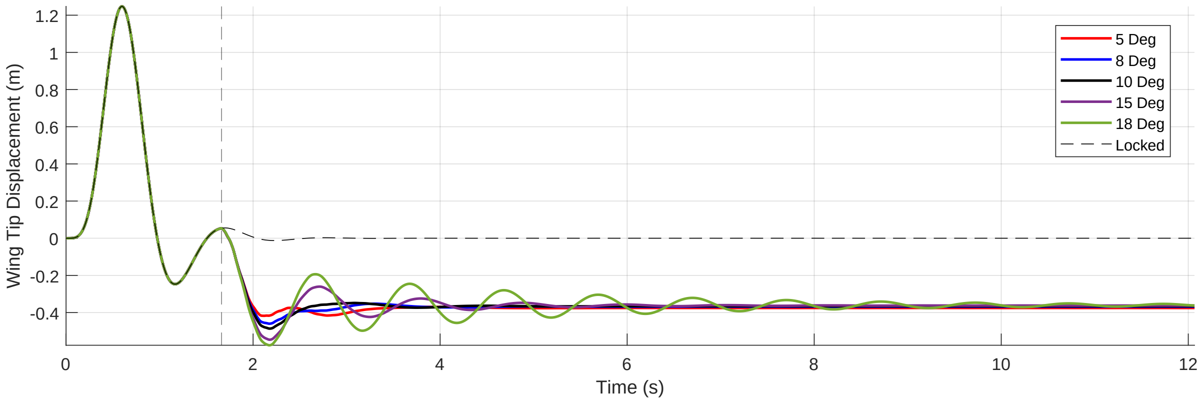

(a) Wing tip displacement for different flare angles under a 25 m half-gust.

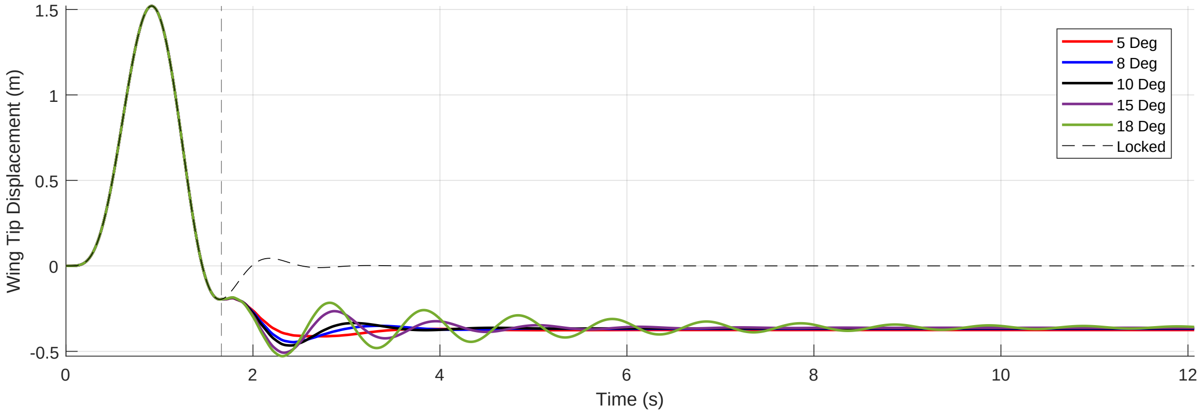

(b) Wing tip displacement for different flare angles under a 50 m half-gust.

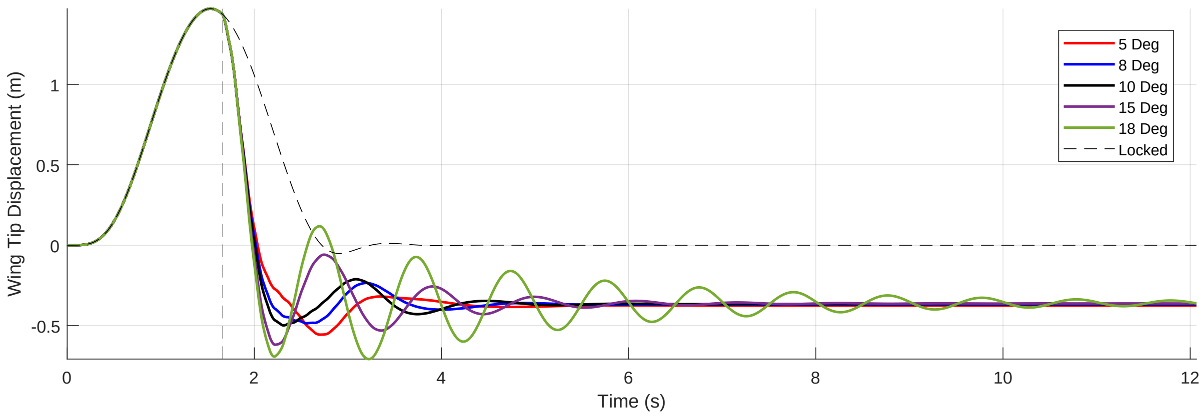

(c) Wing tip displacement for different flare angles under a 100 m half-gust.

Figure 6.22: Wing tip displacements for different flare angles ranging from 5 degrees to 18 degrees under half-gusts of 25 m, 50 m, and 100 m.

To further examine the effects of releasing the hinge at the peak, Figure 6.23 provides relevant insights, illustrating a hinge release at the peak of the 50 m half-gust length case. In this case, the wing experiences larger oscillations following the release, compared to the post-peak release case in Figure 6.22. This is primarily due to the higher acceleration imparted when the hinge is unlocked from the peak displacement position, causing a more sudden dynamic shift in the system. The wing tip is effectively dropped from its maximum deflection, which adds additional energy to the oscillations and delays the system's return to equilibrium. This behaviour highlights the critical importance of release timing on the overall stability of the wing structure, particularly in scenarios involving impulsive gusts where sudden changes in boundary conditions can have pronounced effects on dynamic performance.

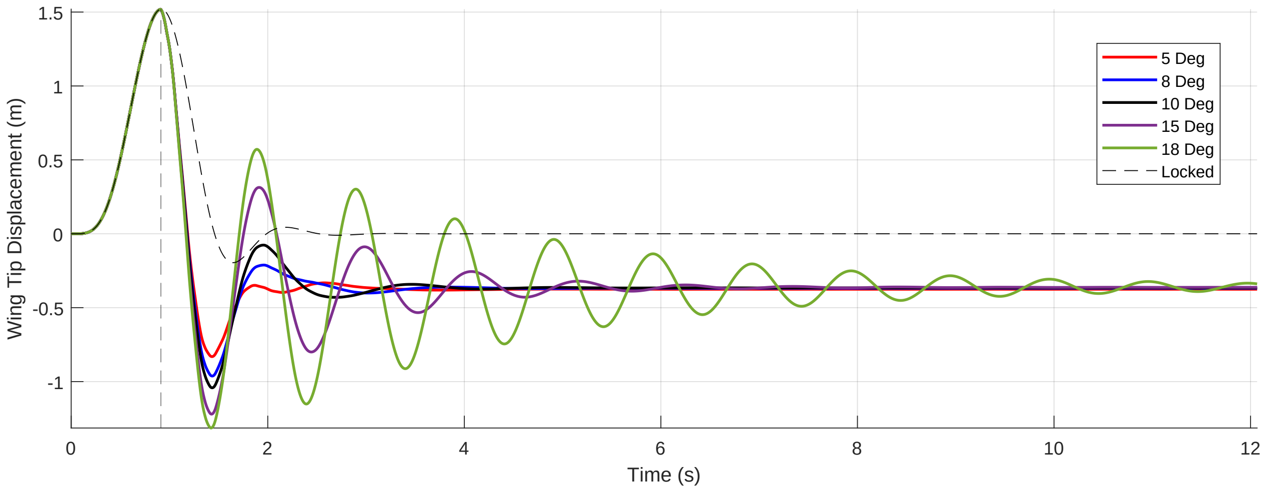

Figure 6.23: Wing tip displacement for different flare angles under a 50 m half-gust at peak displacement.

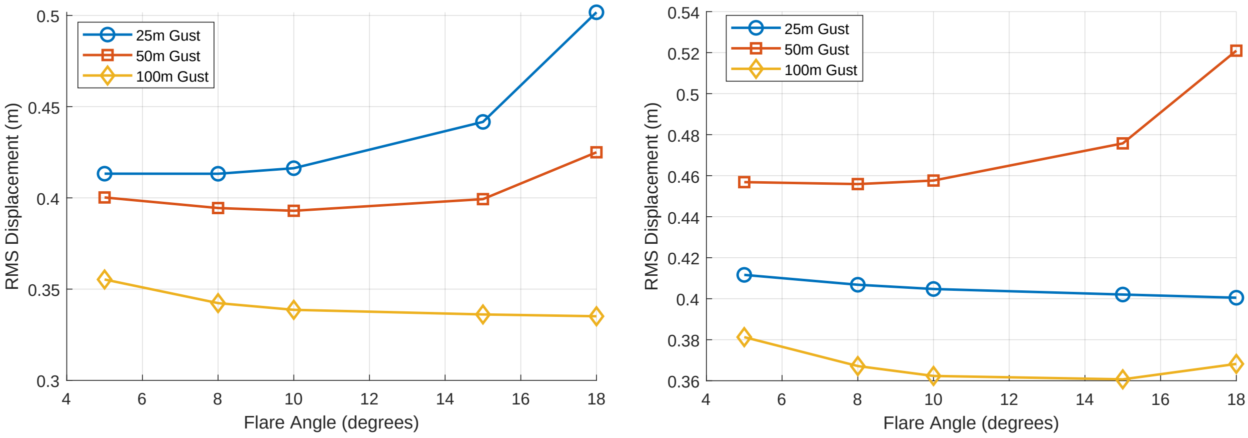

(a) RMS variation for early release (≈ 5 ms) **(b)** RMS variation for 50m gust peak release (≈ 0.9 ms)

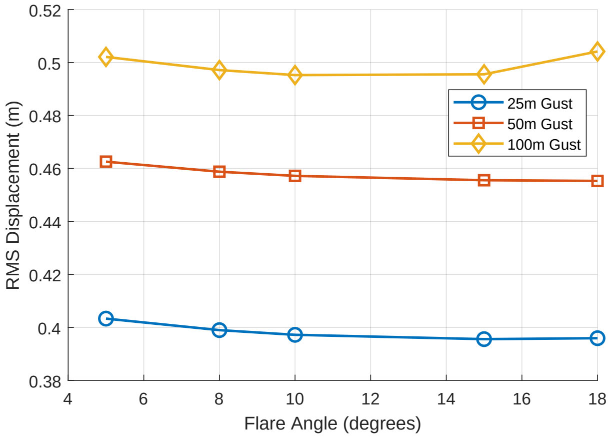

(c) RMS variation for late release (≈ 1.66 ms)

Figure 6.24: Displacement RMS plots for the three different hinge release cases

The three RMS displacement plots in Figure 6.24 illustrate how the hinge release timing, relative to gust peaks, influences oscillatory behaviour. The release points correspond to different gust lengths: the early release (≈ 5 ms) is closer to the peak of the 25 m half-gust, the 50 m gust peak release (≈ 0.9 ms) aligns with the peak of the 50 m half-gust, and the late release (≈ 1.66 ms) is closer to the peak of the 100 m half-gust. Given this correlation, it is expected that the RMS displacement values are higher when the hinge is released at a gust peak, as this timing coincides with maximum disturbance.

A key observation can be drawn from the 100 m gust case in Figure 6.24c and Figure 6.24b, where the RMS displacement increases slightly for the 15 and 18-degree flare angles. Figure A.2 can be referenced to correlate the tip displacement of the wing under the ≈ 0.9 ms release case. This behaviour can be attributed to an increase in load transfer between the FFWT and the inner wing. Additionally, the structural modes in these configurations are closer to the natural frequency of the wing, leading to a system with reduced damping. As a result, the wing structure interacts more dynamically with the gust-induced oscillations. However, this does not seem to comply with the early release case, where for the 100 m gust, the RMS decreases with flare angle. This does not fully reflect the identified behaviour of the curve, since there are small oscillations for the 18-degree flare over time while the other curves are much more damped. The main reason a lower RMS value is obtained is due to the initial response. where the peaks are lower for the 18-degree curve compared to the rest of the flare configurations.

As expected, the RMS values for all the cases, regardless of the release point, are much higher than the maximum RMS achieved in the case of the free-free hinges. However, for most of the cases, a similar trend can be found where the 18-degree flare angle produces more oscillations over the timespan.

6.2.5. Reaction Forces

Similar to the free hinge case, the locked-free case also outputs reaction forces. In order to gauge the output of the solver, a set flare of 10 degrees is simulated under the three gusts and its reaction forces are plotted in Figure 6.25.

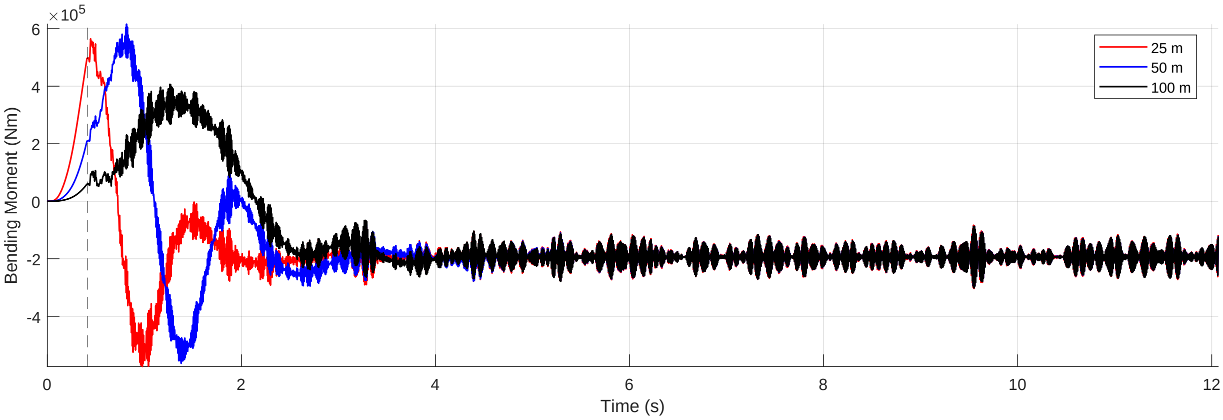

(a) Bending Moment for 10 degree flare configuration released at 0.4 s.

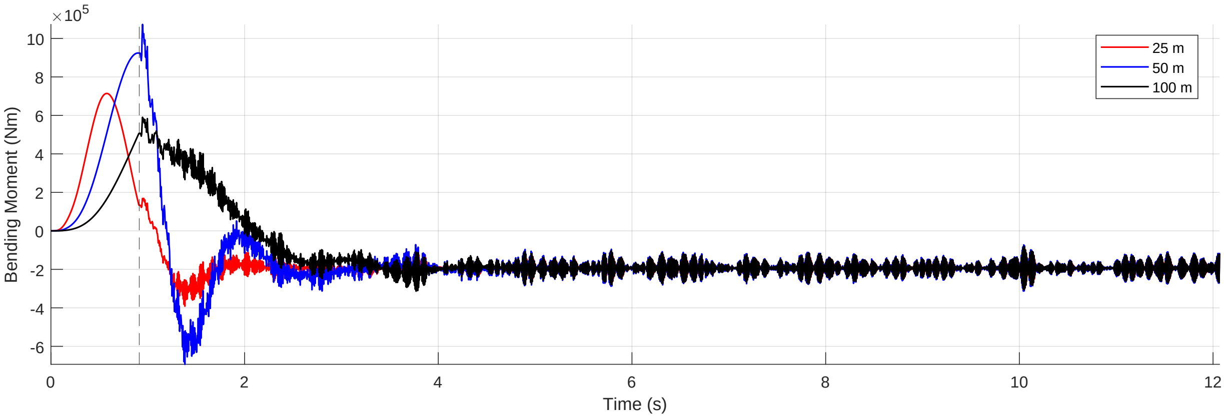

(b) Bending Moment for 10 degree flare configuration released at 0.9 s.

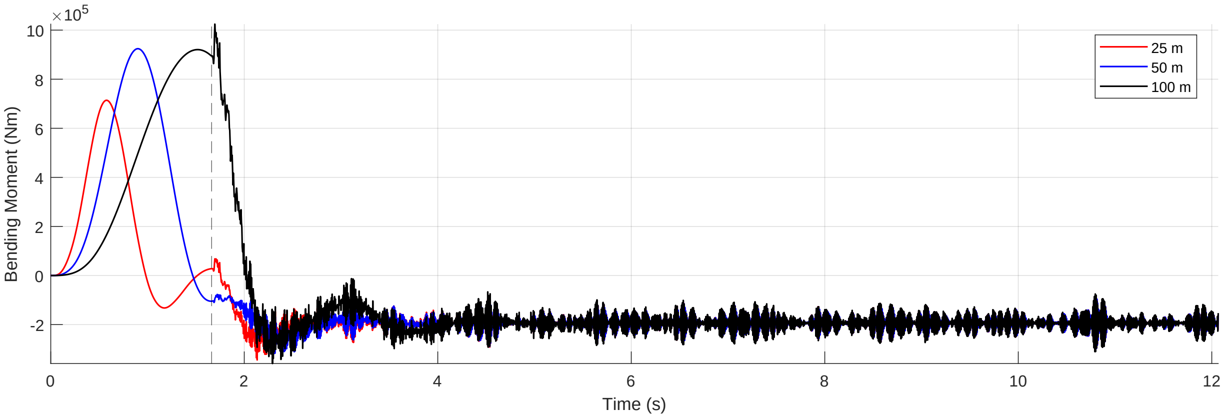

(c) Bending Moment for 10 degree flare configuration released at 1.7 s.

Figure 6.25: Root bending moments for different flare angles ranging from 5 degrees to 18 degrees under half-gust lengths of 25 m, 50 m, and 100 m.

The bending moment plots for the 10-degree flare configuration exhibit a smooth response up to the release point. However, after the release, a noticeable noise appears in the bending moment signal. This noise arises from the sudden change in system dynamics. The unlocking event is modelled through a change in the state-space representation, but the system matrices are linearised around the locked static equilibrium solution, neglecting variations in mass and stiffness. Consequently, since the reaction moments are derived from the equations of motion, an inconsistency arises between the beam's mass and stiffness properties and the calculated displacements, leading to noise.

Furthermore, releasing the wing tip at different times — 0.4 s, 0.9 s, and 1.7 s — does not significantly alter the overall dynamic behaviour after the release. However, the final settling position of the bending moment follows the expected trend, with the bending moment decreasing as the wing tip displacement stabilises. This behaviour aligns with the physical expectation that, after the release, the wing experiences less resistance due to reduced bending forces. Despite the noise introduced during the transition, the system reaches a stable equilibrium position, confirming the validity of the dynamic model for the post-release phase.

Lastly, since shear forces are related to the spatial derivative of the bending moment, any rapid change in the bending moment response can explain the higher-frequency components in the shear force signal. As a result, the abrupt load change at the release point amplifies the noise in the reaction shear forces at the wing, as evident in Figure 6.26. The following section discusses two approaches through which this noise was minimised.

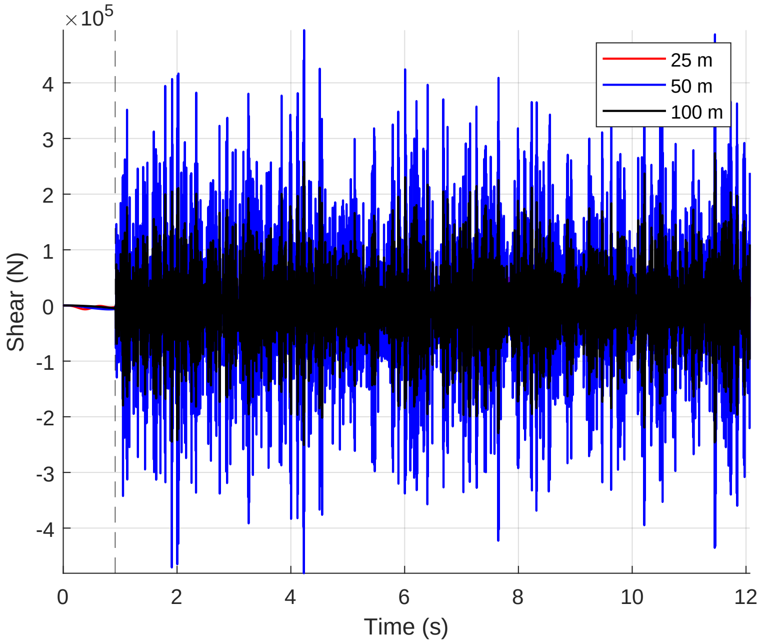

Figure 6.26: Root shear reaction forces for a 10 degree flare configuration

6.3. Addressing the Noise in Reaction Forces

Numerical noise in the locked-free solver is observed to arise during the transition from the locked to the unlocked state-space representation. As aforementioned, this occurs due to the linearisation from the locked static equilibrium. Another possible source of the noise can also be attributed to the accumulating numerical errors introduced due to the time-integration scheme used in PROTEUS. To mitigate these effects, incorporating both structural damping and numerical diffusion has been observed to effectively reduce the noise.

Numerical diffusion is achieved by adding a diffusion term to the state update equation. This approach is similar to the numerical dissipation techniques used in time integration schemes for structural dynamics, such as the Newmark-beta method, and the Generalized-α method [54, 55]. These methods introduce controlled damping to reduce high-frequency numerical oscillations while maintaining accuracy for lower-frequency structural responses. The modified state-space update equation is then given by:

$$x_i = \mathbf{F}x_{i-1} + \Delta t \mathbf{B_{ss}} \frac{u_{i-1} + u_i}{2} - \chi(x_{i-1} - x_{i-2}), \tag{6.2}$$

where:

- x_i is the state vector at time step i,
- $\mathbf{F}$ is the state transition matrix,
- $\mathbf{B_{ss}}$ is the input matrix,
- u_i is the input at time step i,
- Δt is the time step,
- χ is a diffusion coefficient that controls the strength of the numerical damping effect.

The term $\chi(x_{i-1} - x_{i-2})$ acts as a numerical damping force, effectively reducing high-frequency noise by penalizing rapid changes in the state variables. By carefully selecting χ, it is possible to achieve a balance between noise reduction and preserving the system's dynamics. In this section, the effect of incorporating only structural damping as well as this simple numerical damping method is studied.

6.3.1. Effect of Adding a Diffusion Parameter

As introduced before, a small numerical diffusion parameter is also added to test the numerical stability of the solver. Using only the diffusion parameter aids in reducing the noise to some degree, but in the case of the shear loads, the noise still masks the response of the system.

Figure 6.27 plots the bending moment and shear reaction forces at the root, showing noticeable improvement in the bending moment response. However, the shear loads continue to exhibit significant noise. Further increasing the diffusion parameter results in an increase in noise toward the end of the simulation, as shown in Figure A.5. This highlights the trade-off between diffusion and stability, where excessive diffusion can adversely affect the response accuracy in certain regions of the simulation.

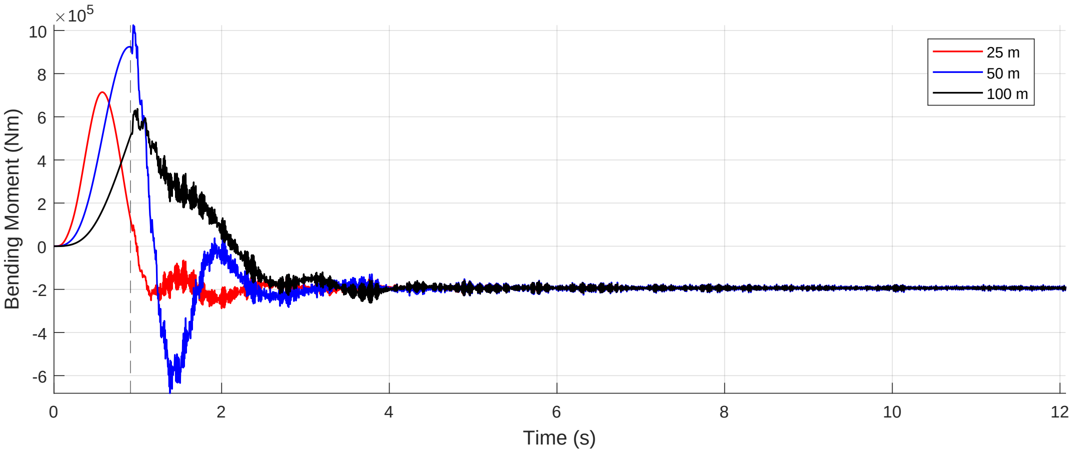

(a) Wing Root Bending Moment over time

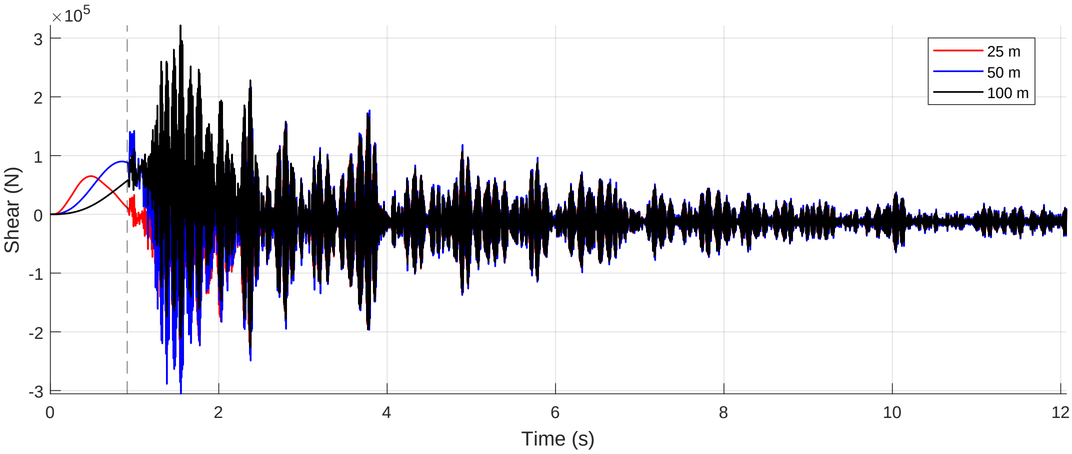

(b) Shear load at root over time

Figure 6.27: Reaction WRBM and shear load at the root with a 10 degree flare and a diffusion parameter of 0.0005

6.3.2. Effect of Adding Structural Damping

Structural damping is defined as a percentage of critical damping, typically low values such as 2% are often used to represent the energy dissipation characteristics of a structure under dynamic loading as seen in the model presented in Córcoles et al. (2023) [45]. For a flexible composite wing with a folding wing tip exhibiting high deformations, structural damping not only helps capture the non-linear behaviour induced by large deflections and complex aerodynamic interactions but also plays a crucial role in stabilizing numerical results.

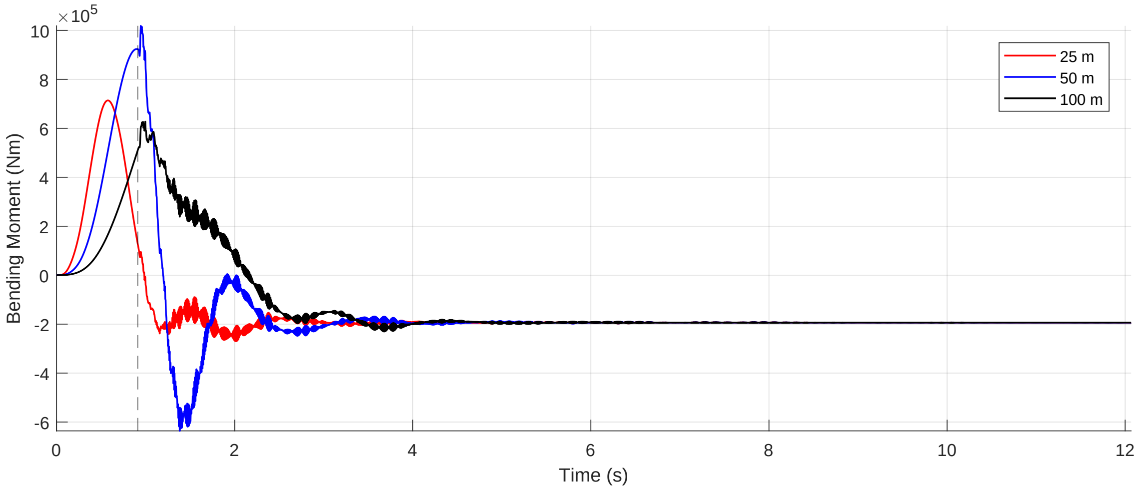

(a) Wing Root Bending Moment over time

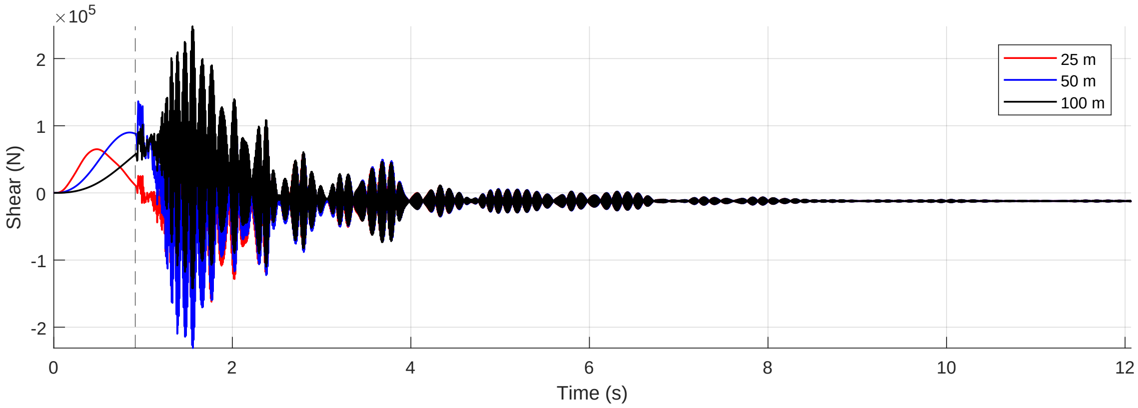

(b) Shear load at root over time

Figure 6.28: Reaction WRBM and shear load at the root with a 10 degree flare and 2% structural damping

Evidently, incorporating structural damping helps improve the noise seen in the reaction forces. Comparing Figure 6.28 to Figure 6.25, there is a significant noise reduction. This reduction is further apparent in the case of the root shear loads. Figure 6.28b shows much higher resolution compared to Figure 6.26. Nevertheless, there is still quite a bit of noise around the release point. Higher damping values are also explored and can be found in Figure A.4; however, they can lead to overly attenuated dynamic responses, masking critical behaviours such as resonance effects or transient oscillations. While increased damping may further reduce noise in the reaction forces and root shear loads, it can also introduce unphysical energy dissipation, which may compromise the accuracy of the simulation. Hence, sufficient damping is needed to stabilise the results and reduce noise, but overly high damping values risk obscuring the true dynamic characteristics of the system. Thus, the choice of damping must carefully account for both numerical stability and physical accuracy.

6.3.3. Effect of Adding Structural Damping and a Diffusion Parameter

Lastly, a combination of both structural damping as well as the numerical diffusion parameter is tested. It is found that slightly higher numerical diffusion values can be used while maintaining stability in the solver. The main advantage of using a combination lies in effectively reducing noise in the reaction forces while preserving the physical accuracy of the system's response. Structural damping primarily targets low-frequency dynamics, providing stability and reducing oscillations, while numerical diffusion mitigates the high-frequency noise. By combining the two, the solver achieves a more balanced and robust performance, allowing for higher diffusion values without introducing excessive noise or compromising the stability of the simulation. This approach enables the system to handle non-linearities and transient behaviours more effectively, as observed in improved bending moment and shear load responses.

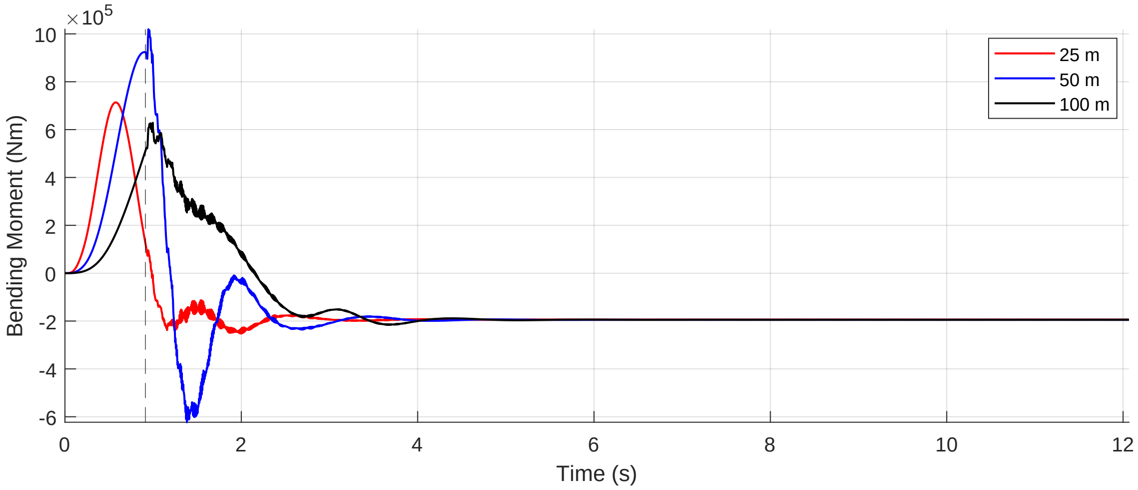

(a) Wing Root Bending Moment over time

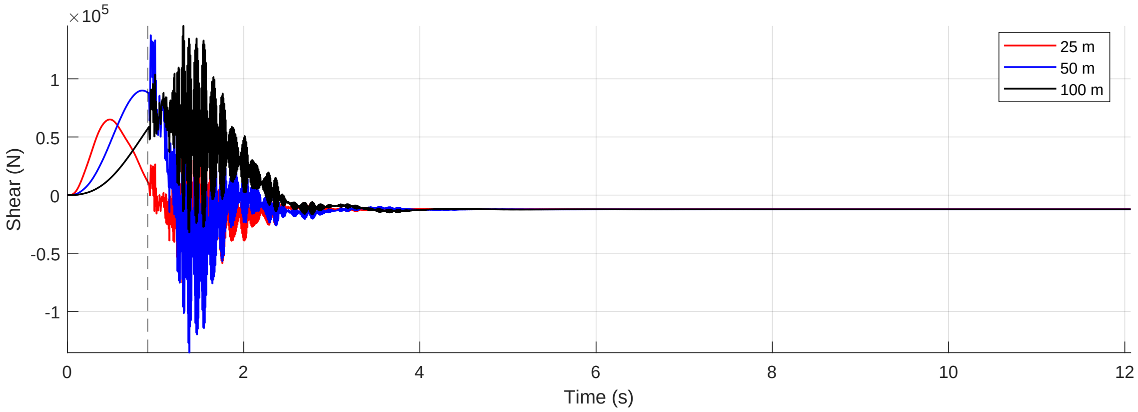

(b) Shear load at root over time

Figure 6.29: Reaction WRBM and shear load at the root with a 10 degree flare and a diffusion parameter of 0.003 and 2% structural damping.

Figure 6.29 clearly illustrates the reduction in noise achieved by combining the diffusion and damping parameters compared to Figure 6.28 and Figure 6.27. However, it is important to note that increasing the numerical diffusion can still lead to significant deviations from the physical response. Furthermore, it was found that the release time also affected the initial noise generated. The three gust lengths are tested and compared with the fully locked case with a pre-released hinge to draw further similarities with the existing solver. It can be found that similar trends are followed by both the locked and the locked-free cases.

Figure 6.30 shows a comparison of the shear force at the root of the wing for three different gust lengths: 25 m, 50 m, and 100 m. In all cases, the initial shear response shows a significant peak due to the sudden gust impact. The red curves represent the Locked-Free configuration, where the hinge is released after an initial locked phase, while the blue curves represent the fully locked case, where the hinge remains fixed throughout the simulation.

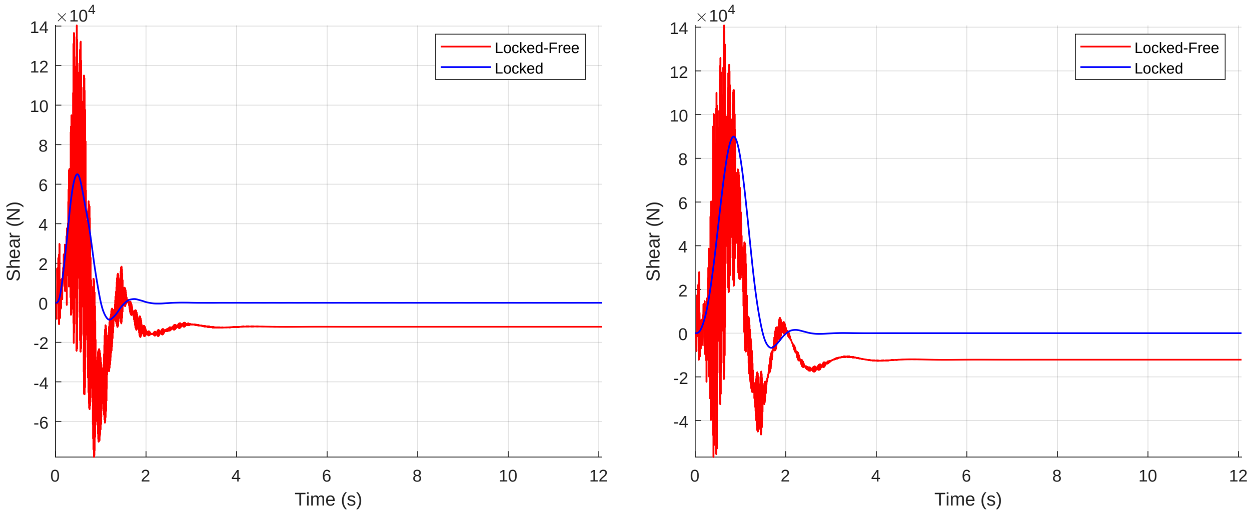

(a) Root Shear for 25 m gust

(b) Root Shear for 50 m gust

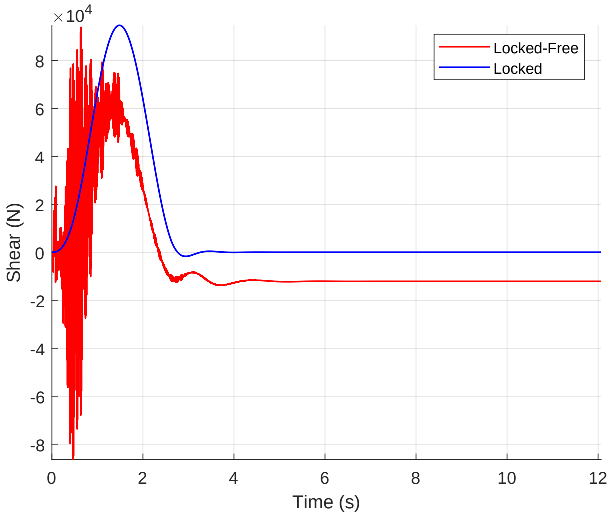

(c) Root Shear for 100 m gust

Figure 6.30: Root chordwise shear plots for the different gust lengths.

The results show a sharp drop in root shear force when the hinge is released in the Locked-Free configuration. This drop is attributed to the release of stored torsional energy at the hinge, which allows the FFWT to pivot more freely and reduces the shear force at the root. Furthermore, the out-of-plane shear loading is higher when the FFWT is not folding and the entire lift acts normally to the wing. However, upon release, the FFWT folds and the lift shifts inboard, transferring some of the load as axial force. In contrast, the locked configuration maintains consistently higher root shear, indicating that keeping the hinge fixed results in greater internal loads transmitted to the root. Additionally, the decreased shear loads in the Locked-Free case align with the static difference in shear forces observed at the root.

Focusing more on the noise, it can be seen that for this pre-released case, the noise generated in the longest gust dissipates sooner compared to the shorter gusts. A qualitative comparison of the noise compared to Figure A.3, suggests that there is not a significant difference in the noise being generated. The noise dissipates slightly sooner in the case of the pre-released case. Rather it is found that a post-peak release creates fluctuations which deviate further from the expected curve.

6.4. Limitations of the Framework

Both the Free-Free and the Locked-Free frameworks effectively capture the dynamic behaviour of wing tip displacements during gust encounters, providing realistic displacement responses across various scenarios. However, its accuracy is limited by the underlying assumptions and linearisation approach used in the model.

A key limitation arises from the use of state-space models linearised around a static equilibrium. While suitable for small to moderate displacements, this approach struggles with large displacements and non-linear transitions, such as hinge unlocking under dynamic loading. The abrupt shift from a constrained (locked) state to an unconstrained (free) state introduces discontinuities that the linearised model cannot fully accommodate. This leads to solver instabilities, particularly in the reaction force calculations at the hinge. Although structural damping and numerical diffusion help mitigate these errors, a fully non-linear dynamic framework would be required for a more accurate representation.

These inaccuracies stem from the assumption of small perturbations around a fixed equilibrium. The system transitions to a new equilibrium when the hinge unlocks, altering the structure's dynamics. However, the solver continues to rely on the original linearised model and, more importantly, the original mass matrix. The mass distribution is significantly altered when the state changes, which does not fully mesh with the calculated displacements, which can be a possible source of the noise.

The framework's limitations are more pronounced in scenarios involving smaller flare angles and shorter gust lengths. Shorter gusts introduce rapid, high-frequency load changes that amplify the wing's dynamic response, making it difficult for the solver to handle abrupt transitions. The non-linear coupling between the inner wing and the FFWT further complicates the simulation, leading to increased numerical instabilities and force discrepancies.

Lastly, the time integration in the solver is performed by a simple trapezoidal scheme. Such a time-integration scheme does not help provide numerical robustness to the solver, with possible cases of errors being carried through the timespan. Errors in this formulation can arise from several sources such as poorly conditioned stiffness matrix from the static solver ($\mathbf{K_s}$ and $\mathbf{K_{ext}}$), constraint drifts caused by errors induced from the gradient constraint matrix ($\mathbf{B}$), and even rounding errors. Time integration schemes such as Newmark-Beta are more adept in simulating more chaotic and non-linear systems, with the middle-point rule, for example, providing unconditional stability and resisting errors from growing over time.

In summary, while the Locked-Free framework provides a reasonable approximation for moderate displacements, it struggles with large, non-linear transitions and abrupt state changes. Improving accuracy would require incorporating non-linear dynamics, a more adaptive state-space model, wherein the mass matrix is updated during the dynamic solution.

IV

Conclusions & Recommendations

7 Conclusions

The literature review revealed extensive research on various modelling frameworks for the Flared Folding wing tip (FFWT) concept, with SHARPy [43] recognised as another prominent non-linear analysis tool currently available. Building on this, the primary objective of this thesis was to integrate and test a flared hinge multibody capability within the in-house aeroelastic optimisation framework, PROTEUS. This enhancement aims to enable future analysis and optimisation of the FFWT concept under various configurations using PROTEUS's relatively cost-effective static and dynamic solvers. The conclusions are presented in two sections, addressing the research questions based on the performance of the static and dynamic solvers within PROTEUS.

1. Static Behaviour

- **Main Question:** How can the static behaviour of the Flared Folding Wing Tip be accurately captured using the in-house aeroelastic optimization framework?
- **Sub-Question:**
  - How can the hinge axis be integrated into the existing co-rotational, non-linear static structural framework?

The static behaviour of the Flared Folding Wing Tip (FFWT) was successfully captured using the existing non-linear static solver in PROTEUS. This was achieved by addressing the sub-question—integrating the hinge axis into the co-rotational, non-linear static structural framework. The hinge joint was effectively incorporated into the constraint gradient matrix by defining constraints locally using the nodal elastic frames. Analytical checks confirmed that the solutions from the solver followed expected patterns. However, an initial-value problem was found with possible division-by-zero errors possibly due to the reduced stiffness leading to poor conditioning of the tangent stiffness matrix, which ultimately led to erratic behaviour of the solver, especially with smaller flare angles. The presence of bi-stable numerical solutions at lower flare angles further suggested the dependence of the solver on initial conditions.

Further exploration of the flared folding wing tip revealed that the solver's predictions aligned well with results from existing literature. Notably, around 17% reduction in wing root bending moment was observed with a 15-degree flare, indicating the potential benefits of incorporating the FFWT. Introducing a flare angle divides the hinge moment into two components: a bending moment and a chordwise torsional moment. Increasing the flare angle reduces the bending moment while increasing the torsional moment, resulting in a smaller fold angle for the FFWT. Additionally, around 25% increase in wing-root bending moment (WRBM) was noted with increased flare, likely due to the larger torsional moment transferring more load from the FFWT to the main wing structure.

2. Dynamic Behaviour

- **Main Question:** How can the dynamic module of PROTEUS be adapted to simulate a hinge-unlocking event in a wing with a Flared Folding Wing Tip?
- **Sub-Questions:**
  - Can PROTEUS' dynamic solver capture the response of a Flared Folding Wing Tip (FFWT) with an unlocked hinge?
  - What modifications can be made to the existing dynamic formulation to transition from a locked to an unlocked hinge state?
  - How does the timing of the hinge release affect the wing's response during a gust encounter?

Two configurations were tested against a baseline locked-hinge configuration, where the wing tip remained fixed. Addressing the first sub-question, the first configuration, referred to as *free-free*, was simulated. In this setup, the hinge remained continuously free, with the solver initialised from this free state. The second configuration, termed *locked-free*, initially solved the dynamics with a locked hinge, which was then released during the gust encounter to simulate an unlocking event. Developed to address the second sub-question, the locked-free configuration allowed for testing the effect of different release times on the wing's response.

The solver demonstrated robust performance for the free-free hinge configuration, maintaining stability across most tested cases by linearising around the free non-linear static solution. However, for a 5-degree flare angle, the wing tip displacement exhibited a relatively higher initial excitation under the 100 m half-gust length, along with an increased root-mean-square (RMS) displacement compared to other flare angles under the same gust conditions. Additionally, the normalised minimum WRBM and peak root shear loads were significantly higher in the 5-degree flare cases. To better understand the increased persistence of oscillations at higher flare angles, the structural frequency of these configurations was compared with the gust frequency. This analysis revealed that the eigenfrequency of the structure approached that of the 25 m half-gust case, explaining the amplified oscillations. Testing the free-free configuration also provided insight into the capability of the current solver to handle such large deformations, building the grounds for the locked-free solver to simulate the hinge release.

To simulate the dynamic release of the hinge, an adaptation of the current framework was proposed. This approach involved initialising two dynamic cases, both starting from the locked static equilibrium. However, in one case, the constraint gradient matrix was modified to free the rotational degree of freedom, allowing the hinge to be modelled after release. At the designated release time, the state-space matrices were switched from the locked to the unlocked configuration, with the state vector adjusted to incorporate the additional rotational degree of freedom. This solver directly addresses the main research question by enabling the simulation of hinge release. It successfully produced a realistic displacement response; however, the reaction forces after release exhibited significant noise, likely due to the abrupt state change and the resulting high accelerations.

Efforts to mitigate this noise revealed that introducing structural damping significantly reduced the issue. Higher values of structural damping (up to 5%) were required to suppress most of the noise in the reaction forces, though this is relatively high for lightweight aerospace structures, where damping is typically below 2%. However, excessive structural damping can lead to deviations from the physical response, underscoring the need for a balanced approach. Consequently, a numerical diffusion term was implemented to reduce high-frequency noise. While a high diffusion coefficient masked important aspects of the response, a combination of 2% structural damping and a tuned diffusion coefficient effectively filtered out much of the noise while preserving the underlying dynamics.

Finally, the release timing of the FFWT was varied to evaluate its impact on the wing's response addressing the final sub-question. An early release resulted in behaviour resembling the free-free system, with reduced peak displacements. However, as the gust had not yet reached its peak, the wing tip continued to rise before settling into equilibrium. Releasing the FFWT at the gust peak caused a significant drop and high-amplitude oscillations due to the rapid dissipation of stored energy. Conversely, a late release exhibited behaviour akin to a fully locked system until the moment of release, after which oscillations occurred before stabilising. The analysis of the 10-degree flared hinge system, incorporating structural damping and numerical diffusion, confirmed the expected reduction in loads at the main wing root.

8 Recommendations and Potential Improvements for the Framework

This section outlines key usage recommendations and suggests possible improvements for the PROTEUS framework based on the limitations and advantages identified in this thesis.

Usage Recommendations

- The augmented framework is suitable for optimisation cases but should be applied to cases with relatively large flares ($> 8°$). Smaller flares can result in instability, causing the static solver to either diverge or produce bi-stable solutions, which may propagate into the dynamic solver.
- To mitigate instability, a more accurate initial displacement guess should be provided to the Newton-Raphson solver.

Dynamic Framework Observations

- The dynamic hinge unlock framework provides stable displacement results. However, large accelerations at the release point generate noise in the reaction forces.
- Noise can be damped using structural damping and the coarse numerical diffusion term implemented in this thesis. For more physically accurate results, a specialised numerical approach should be employed to eliminate this noise effectively.

Future Improvements

- While this model can support preliminary design problems, further development is necessary to enhance its accuracy and applicability. Specifically:
  - A more tailored initial displacement guess for the static solver to improve convergence rates.
  - Implementation of a fully non-linear solver updating the mass and stiffness of the structure to handle large deformations.
  - Account for changes in the aerodynamic mesh resulting from large deformations.
  - Using a more robust time integration framework like Newmark-Beta to handle dynamic instability and improve solver convergence.

Possible Research Directions

Based on the suggested improvements, further research is required to assess the performance of this framework with more specialised numerical damping to better accommodate larger displacements and reduce noise. The issue of noise could also be addressed by exploring alternative time-integration methods to enhance solver stability. However, accumulating errors and potential constraint drift must be considered in the development of a fully non-linear solver. The challenge of constraint drift in constrained multibody simulations, as investigated by Braun & Goldfarb (2009) [56], highlights how error accumulation can cause motion constraints to deviate over time, leading to physically inconsistent solutions.

Moreover, the findings suggest that a linearised dynamic approach may be insufficient for capturing larger displacements, further reinforcing the need for a fully non-linear solver. To accurately represent all state transitions, the current framework could be extended by incorporating an iterative update of the mass and stiffness matrices at each time step. However, this would come at a high computational cost.

Once a more stable solver is established, its accuracy should be validated through experimental analysis, ensuring reliability for more complex studies.

Additionally, this model provides a powerful tool for exploring various design parameters of the flared folding wing tip (FFWT) concept. One key research gap in the existing literature is the effect of the aspect ratio between the main wing and the folding wing tip. With a more stabilised solver, the framework can be leveraged for a sizing study across a range of flare angles to optimise performance.

The results indicate that as flare angles increase, the dynamic response of the FFWT becomes less damped. To address this, a design study can be conducted using PROTEUS to identify parameters that enhance the wing tip's dynamic behaviour. One potential avenue is investigating the use of ailerons on the FFWT to help mitigate oscillations after the hinge is unlocked.

Furthermore, with these added capabilities, a more focused study can be carried out using PROTEUS to assess the impact of hinge release timing on system behaviour. Finally, analysing the FFWT's response under a continuous gust model would provide deeper insight into its aerodynamic and structural performance.

Bibliography

[1] Chi Wing Cheng, Alvaro Cea, Rafael Palacios, Andrea Castrichini, and Thomas Wilson. *Nonlinear Multibody Modelling of Flexible Aircraft with Flared Hinged Wings*. doi: 10.2514/6.2024-1441.

[2] Frederico Afonso, Martin Sohst, Carlos M.A. Diogo, Simão S. Rodrigues, Ana Ferreira, Inês Ribeiro, Ricardo Marques, Francisco F.C. Rego, Abdolrasoul Sohouli, Joana Portugal-Pereira, Hugo Policarpo, Bruno Soares, Bruna Ferreira, Edgar C. Fernandes, Fernando Lau, and Afzal Suleman. Strategies towards a more sustainable aviation: A systematic review. *Progress in Aerospace Sciences*, 137:100878, 2023. ISSN 0376-0421. doi: https://doi.org/10.1016/j.paerosci.2022.100878.

[3] Peretz P. Friedmann. On-blade control of rotor vibration, noise, and performance: Just around the corner? the 33rd alexander nikolsky honorary lecture. *Journal of the American Helicopter Society*, 59 (4):1–37, 2014. ISSN 2161-6027. doi: 10.4050/JAHS.59.041001.

[4] Luca Marino, Ilias Kiat, Adrian Eberle, and Jurij Sodja. *Parametric study of a switchable vortex generator for load alleviation in transonic conditions*. doi: 10.2514/6.2024-2110.

[5] Izabela K Kuder, Andres F Arrieta, Mathias Rist, and Paolo Ermanni. Aeroelastic response of a selectively compliant morphing aerofoil featuring integrated variable stiffness bi-stable laminates. *Journal of Intelligent Material Systems and Structures*, 27(14):1949–1966, 2016. doi: 10.1177/1045389X15620038.

[6] Andrea Castrichini, Vijaya H. Siddaramaiah, Dario E. Calderon, Jonathan E. Cooper, Thomas Wilson, and Y. Lemmens. Preliminary investigation of use of flexible folding wing tips for static and dynamic load alleviation. *The Aeronautical Journal*, 121(1235):73–94, 2017. doi: 10.1017/aer.2016.108.

[7] Fintan Healy, Ronald C. Cheung, Djamel Rezgui, Jonathan E. Cooper, Thomas Wilson, and Andrea Castrichini. *On the Nonlinear Geometric Behaviour of Flared Folding Wingtips*. 2022. doi: 10.2514/6.2022-0656.

[8] Roeland De Breuker. *Energy-based Aeroelastic Analysis and Optimisation of Morphing Wings*. Dissertation (tu delft), Delft University of Technology, 2011.

[9] Candelaria Bergero, Greer Gosnell, Dolf Gielen, Seungwoo Kang, Morgan Bazilian, and Steven J Davis. Pathways to net-zero emissions from aviation. *Nature Sustainability*, 6(4):404–414, 2023.

[10] Xavier Carrillo Córcoles. *An experimental study on flared folding wingtips*. Master thesis, Delft University of Technology, 2022. URL http://resolver.tudelft.nl/uuid:ef44ea11-a9b4-415d-97be-51d38380a3a5.

[11] Jan R. Wright and Jonathan. E. Cooper. *Introduction to Aircraft Aeroelasticity and Loads*. John Wiley Sons, Incorporated, 2015. ISBN 9781118700426.

[12] Zhenlong Wu, Yihua Cao, and Muhammad Ismail. Gust loads on aircraft. *The Aeronautical Journal*, 123(1266):1216–1274, 2019. doi: 10.1017/aer.2019.48.

[13] *Easy Access Rules for Large Aeroplanes (CS-25)*. EASA, ammendment 27 edition, January 2023. URL https://www.easa.europa.eu/en/document-library/easy-access-rules/online-publications/easy-access-rules-large-aeroplanes-cs-25?page=1.

[14] Andrea Mancini and Roelof Vos. *The Effect of Maneuver Load Alleviation Strategies on Aircraft Performance Indicators*. doi: 10.2514/6.2019-3272.

[15] Roland J. White. Improving the airplane efficiency by use of wing maneuver load alleviation. *Journal of Aircraft*, 8(10):769–775, 1971. doi: 10.2514/3.59169.

[16] Boris Moulin and Moti Karpel. Gust loads alleviation using special control surfaces. *Journal of Aircraft*, 44(1):17–25, 2007. doi: 10.2514/1.19876.

[17] Sebastian Heinze and Moti Karpel. Analysis and wind tunnel testing of a piezoelectric tab for aeroelastic control applications. *Journal of Aircraft*, 43(6):1799–1804, 2006. doi: 10.2514/1.20060.

[18] Lars O Bernhammer, Jurij Sodja, Moti Karpel, and Roeland De Breuker. Design of an autonomous flap for load alleviation. In *25th International Conference on Adaptive Structures and Technologies*, pages 1–11. ICAST, 2014.

[19] Lars O. Bernhammer, Roeland De Breuker, and Moti Karpel. Energy harvesting for actuators and sensors using free-floating flaps. *Journal of Intelligent Material Systems and Structures*, 28(2):163–177, January 2017. ISSN 1045-389X. doi: 10.1177/1045389X16645954.

[20] Abdel Darwich Ajjour, Jonathan Cooper, and Thomas C S Rendall. *Gust and Manoeuvre Loads Alleviation Using Lower Surface Spoiler*. doi: 10.2514/6.2022-0245.

[21] Junaid Ullah, Thorsten Lutz, Lorenz Klug, Rolf Radespiel, Jochen Wild, and Ralf Heinrich. Approach for aerodynamic gust load alleviation by means of spanwise-segmented flaps. *Journal of Aircraft*, 60 (3):835–856, 2023. doi: 10.2514/1.C037086.

[22] Junaid Ullah, Skander Kamoun, Jens Müller, and Thorsten Lutz. *Active Gust Load Alleviation by Means of Steady and Dynamic Trailing and Leading Edge Flap Deflections at Transonic Speeds*. doi: 10.2514/6.2022-1334.

[23] Lorenz Klug, Rolf Radespiel, Junaid Ullah, Ferdinand Seel, Thorsten Lutz, Jochen Wild, Ralf Heinrich, and Thomas Streit. *Actuator concepts for active gust alleviation on transport aircraft at transonic speeds*. doi: 10.2514/6.2020-0271.

[24] Luca Marino, Adrian Eberle, and Jurij Sodja. Three-dimensional parametric analysis of a switchable vortex generator for aerodynamic load alleviation at transonic speeds. In *Proceedings of the AIAA SCITECH 2025 Forum*, 2025. doi: 10.2514/6.2025-0035. Article AIAA 2025-0035.

[25] Yonghong Li and Ning Qin. A review of flow control for gust load alleviation. *Applied Sciences*, 12 (20), 2022. ISSN 2076-3417. doi: 10.3390/app122010537.

[26] Zhijun Wang, Daniel Peeters, and Roeland De Breuker. An aeroelastic optimisation framework for manufacturable variable stiffness composite wings including critical gust loads. *Structural and Multidisciplinary Optimization*, 65, 2022. URL `https://api.semanticscholar.org/CorpusID:252409412`.

[27] Marco Tito Bordogna, P.M.G.J. Lancelot, Dimitri Bettebghor, and Roeland De Breuker. Static and dynamic aeroelastic tailoring with composite blending and manoeuvre load alleviation. *Structural and Multidisciplinary Optimization*, 61:2193–2216, 2020. URL `https://api.semanticscholar.org/CorpusID:212778397`.

[28] Enzo Cosentino and C. R. Llewellyn-Jones. Flow control device. UK Patent Application, April 2022. https://patents.google.com/patent/GB2600130A/en.

[29] Andrea Castrichini, Enzo Cosentino, Federica Siotto, Xiaoyang Sun, Josh Coppin, Raul L. Vargas, Ignacio G. Ruis, and Michael Hadjipantelis. Preliminary investigation of the superelastic monostable

spoiler for dynamic gust loads alleviation. In *20th International Forum on Aeroelasticity and Structural Dynamics (IFASD 2024)*, 2024. URL https://conf.ifasd2024.nl/proceedings/display_manuscript/26.htm.

[30] Shijun Guo, Daochun Li, and Otto Sensburg. *Optimal design of a passive gust alleviation device for a flying wing aircraft.* doi: 10.2514/6.2012-5625.

[31] Shijun Guo, Jaime Espinosa De Los Monteros, and Ying Liu. Gust alleviation of a large aircraft with a passive twist wingtip. *Aerospace*, 2(2):135–154, 2015. ISSN 2226-4310. doi: 10.3390/aerospace2020135.

[32] Robert W. Kress. Variable sweep wing design. In *Aircraft Prototype and Technology Demonstrator Symposium*, page 1051, 1983.

[33] Tigran Mkhoyan, Nisarg Rashmin Thakrar, Roeland De Breuker, and Jurij Sodja. *Design and Development of a Seamless Smart Morphing Wing Using Distributed Trailing Edge Camber Morphing for Active Control.* doi: 10.2514/6.2021-0477.

[34] Comandur Venkatesan. *Fundamentals of Helicopter Dynamics.* CRC Press, 2014. ISBN 9781466566354.

[35] Airbus. AlbatrossONE - Airbus, 2025. URL https://www.airbus.com/en/innovation/future-aircraft/wings/albatrossone. Accessed: 2025-02-01.

[36] Airbus. Extra performance wing demonstrator takes off, 2023. URL https://www.airbus.com/en/newsroom/stories/2023-11-extra-performance-wing-demonstrator-takes-off. Accessed: 2025-02-01.

[37] Jan Irving and R Davies. Wing tip device. United States Patent, Oct. 2007. https://patents.google.com/patent/US7275722B2/en.

[38] Thomas Wilson, Martin Herring, John Pattinson, Jonathan Cooper, Andrea Castrichini, Rafic Ajaj, and Hitul Dhoru. An aircraft wing with a moveable wing tip device for load alleviation. World Intellectual Property Organization, July 2017. https://patents.google.com/patent/WO2017118832A1/en.

[39] Andrea Castrichini, Vijaya H. Siddaramaiah, Dario E. Calderon, Jonathan E. Cooper, Thomas Wilson, and Y. Lemmens. Nonlinear folding wing tips for gust loads alleviation. *Journal of Aircraft*, 53(5): 1391–1399, 2016. doi: 10.2514/1.C033474.

[40] Ronald C. M. Cheung, Djamel Rezgui, Jonathan E. Cooper, and Thomas Wilson. Testing of a hinged wingtip device for gust loads alleviation. *Journal of Aircraft*, 55(5):2050–2067, 2018. doi: 10.2514/1.C034811.

[41] Claudio Conti, Francesco Saltari, Franco Mastroddi, Thomas Wilson, and Andrea Castrichini. Quasi-steady aeroelastic analysis of the semi-aeroelastic hinge including geometric nonlinearities. *Journal of Aircraft*, 58(5):1168–1178, 2021. doi: 10.2514/1.C036115.

[42] Michel Géradin and Alberto Cardona. *Flexible Multibody Dynamics: A Finite Element Approach.* Wiley, 2001. ISBN 9780471489900.

[43] Alfonso del Carre, Arturo Muñoz-Simón, Norberto Goizueta, and Rafael Palacios. Sharpy: A dynamic aeroelastic simulation toolbox for very flexible aircraft and wind turbines. *Journal of Open Source Software*, 4(44):1885, 2019. doi: 10.21105/joss.01885.

[44] Grigorios Dimitriadis. *Introduction to Non-Linear Aeroelasticity.* John Wiley Sons, 2017. ISBN 9781118756478. doi: 10.1002/9781118756478.

[45] Xavier Carrillo, Roeland De Breuker, and Jurij Sodja. *Nonlinear Low-Fidelity Numerical Model of the Flared Folding Wingtip*. . doi: 10.2514/6.2023-0378.

[46] Fintan Healy, Ronald Cheung, Djamel Rezgui, Jonathan Cooper, Thomas Wilson, and Andrea Castrichini. Experimental and numerical nonlinear stability analysis of wings incorporating flared folding wingtips. *Journal of Aircraft*, 61(1):140–154, 2024. doi: 10.2514/1.C037167.

[47] Carmine Valente, Andrea Castrichini, Thomas Wilson, Alessandro Landi, and Jonathan E. Cooper. High fidelity cfd/csm analysis of a folding wing-tip device for aircraft loads alleviation. In *6th Aircraft Structural Design Conference*, 2018.

[48] Joseph Katz and Allen Plotkin. *Low-Speed Aerodynamics*. Cambridge Aerospace Series. Cambridge University Press, 2 edition, 2001.

[49] Xavier Carrillo, Christoph Mertens, Andrea Sciacchitano, Bas van Oudheusden, Roeland De Breuker, and Jurij Sodja. *Wing Stiffness and Hinge Release Threshold Effects on Folding Wingtip Gust Load Alleviation*. . doi: 10.2514/6.2022-1559.

[50] Ronald C. Cheung, Christopher Wales, Djamel Rezgui, Jonathan E. Cooper, and Thomas Wilson. *Modelling of Folding Wing-Tip Devices for Gust Loads Alleviation*. doi: 10.2514/6.2018-0462.

[51] Noud Werter. *Aeroelastic Modelling and Design of Aeroelastically Tailored and Morphing Wings*. Dissertation (tu delft), Delft University of Technology, 2017.

[52] Jean-Marc Battini and Costin Pacoste. Co-rotational beam elements with warping effects in instability problems. *Computer Methods in Applied Mechanics and Engineering*, 191(17):1755–1789, 2002. ISSN 0045-7825. doi: https://doi.org/10.1016/S0045-7825(01)00352-8.

[53] Oliver A. Bauchau. *Flexible Multibody Dynamics*. Solid Mechanics and Its Applications. Springer Netherlands, 2010. ISBN 9789400703353.

[54] Nathan M. Newmark. A method of computation for structural dynamics. *Journal of the Engineering Mechanics Division, ASCE*, 85(EM3):67–94, 1959.

[55] Kenneth E. Jansen, Christian H. Whiting, and Gregory M. Hulbert. A generalized- method for integrating the filtered navier–stokes equations with a stabilized finite element method. *Computer Methods in Applied Mechanics and Engineering*, 190(3):305–319, 2000. ISSN 0045-7825. doi: https://doi.org/10.1016/S0045-7825(00)00203-6.

[56] David J. Braun and Michael Goldfarb. Eliminating constraint drift in the numerical simulation of constrained dynamical systems. *Computer Methods in Applied Mechanics and Engineering*, 198(37): 3151–3160, 2009. ISSN 0045-7825. doi: https://doi.org/10.1016/j.cma.2009.05.013. URL `https://www.sciencedirect.com/science/article/pii/S0045782509002011`.

A Appendix

A.1. QR Decomposition of Structural State Space

The full structural system is characterized by the mass ($\mathbf{M}$), stiffness($\mathbf{K}$), and damping matrix ($\mathbf{C}$). The boundary conditions are imposed via the constraint gradient matrix, $\mathbf{B}$. If N_{dof} is the total number of degrees of freedom and N_{BC} is the number of constrained DOFs, then the number of free DOFs is:

$$N_{\text{free}} = N_{\text{dof}} - N_{\text{BC}}.$$

A QR decomposition of $\mathbf{B}^T$ yields:

$$\mathbf{B}^T = \mathbf{QR},$$

where $\mathbf{Q}$ is an orthogonal matrix partitioned as

$$\mathbf{Q} = \begin{pmatrix} \mathbf{Q}_1 & \mathbf{Q}_2 \end{pmatrix}.$$

Here, $\mathbf{Q}_1 \in \mathbb{R}^{N_{\text{dof}} \times N_{\text{Bc}}}$ is associated with the constrained directions, and $\mathbf{Q}_2 \in \mathbb{R}^{N_{\text{dof}} \times N_{\text{free}}}$ spans the null space of $\mathbf{B}$. Defining

$$\mathbf{Q}_2^T = \text{Qi},$$

we then construct the matrix:

$$\mathbf{A} = \begin{pmatrix} \mathbf{B} \\ \mathbf{Q}_2^T \end{pmatrix}.$$

Its inverse is computed as:

$$\mathbf{R}_R = \mathbf{A}^{-1},$$

which is partitioned into

$$\mathbf{R}_R = \begin{pmatrix} \mathbf{S} & \mathbf{R} \end{pmatrix},$$

where $\mathbf{S}$ corresponds to the constrained (fixed) DOFs and $\mathbf{R}$ to the free DOFs.

This transformation effectively projects the full state-space equations into their reduced forms, considering only the free degrees of freedom:

$$\mathbf{R}^T\mathbf{M}\mathbf{R}\ddot{\mathbf{p}} + \mathbf{R}^T\mathbf{C}\mathbf{R}\dot{\mathbf{p}} + \mathbf{R}^T\mathbf{K}\mathbf{R}\mathbf{p} = \mathbf{R}^T\mathbf{f},$$

thereby incorporating the boundary conditions directly into the structural dynamics. Now since all the terms appear explicitly in the equation, a state-space system can be formulated with the following state matrix $\mathbf{A_{ss}}$:

$$\mathbf{A}_{\text{ss}} = \begin{pmatrix} (\mathbf{R}^T\mathbf{M}\mathbf{R})^{-1}(\mathbf{R}^T\mathbf{C}\mathbf{R}) & (\mathbf{R}^T\mathbf{M}\mathbf{R})^{-1}(\mathbf{R}^T\mathbf{K}\mathbf{R}) \\ \mathbf{I} & \mathbf{0} \end{pmatrix}$$

A.2. Static Equilibrium of Different Flare Angles

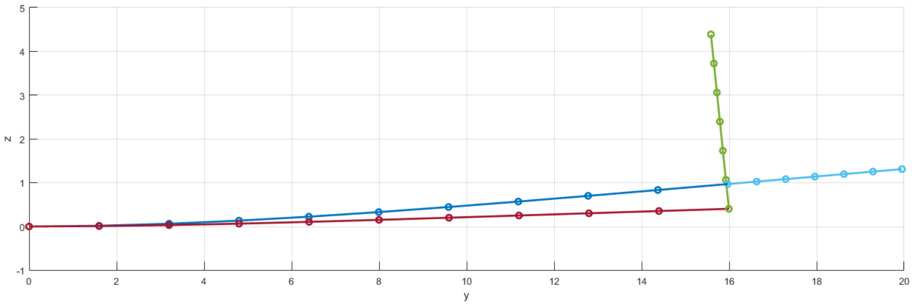

(a) 2° Flare

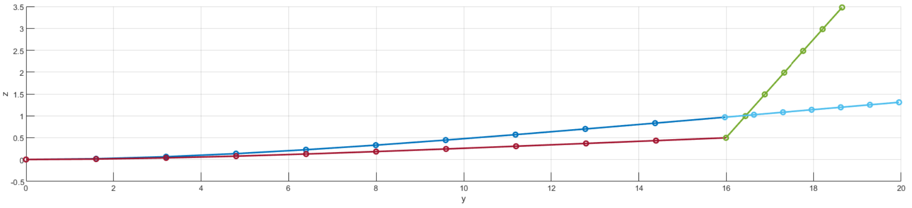

(b) 5° Flare

Figure A.1: Locked wing-tip deformation compared to unlocked hinge at different flare angles (Part 1).

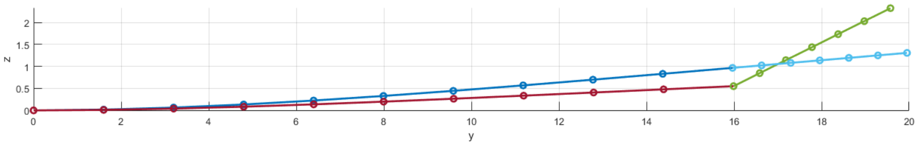

(c) 10° Flare

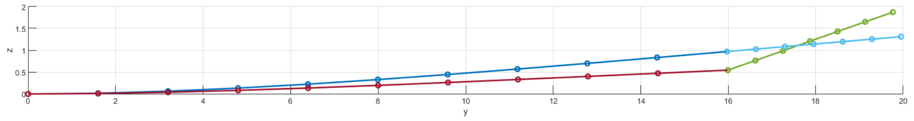

(d) 15° Flare

Figure A.1: Locked wing-tip deformation compared to unlocked hinge at different flare angles (Part 2).

A.3. Late Release (≈ 0.9 ms) Displacement Plots for 25m and 100m Gusts

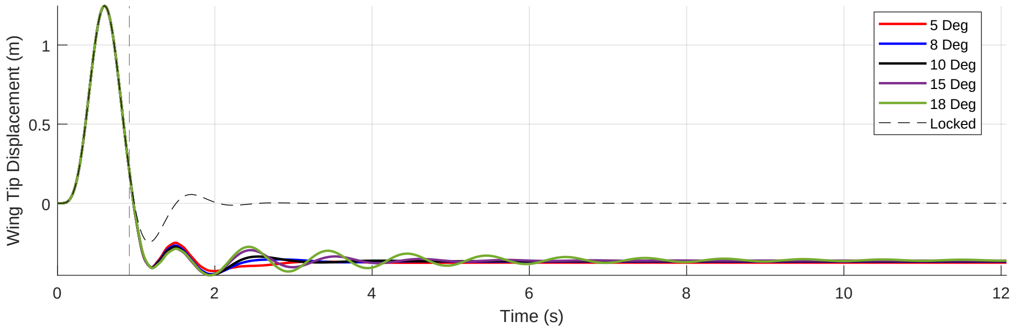

(a) Displacement over time for 25m half gust length

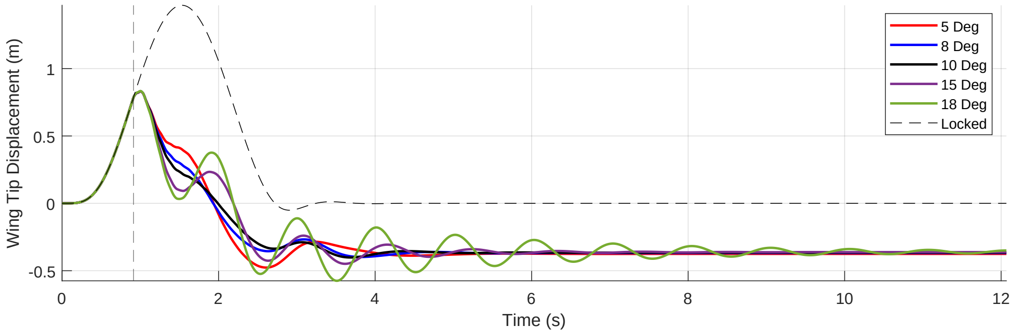

(b) Displacement over time for 100m half gust length

Figure A.2: Displacement over time of different flare configurations for 25m and 100m half gust length for a (≈ 0.9 ms) release.

A.4. Root Shear Plots for Late Release(≈ 0.9 ms)

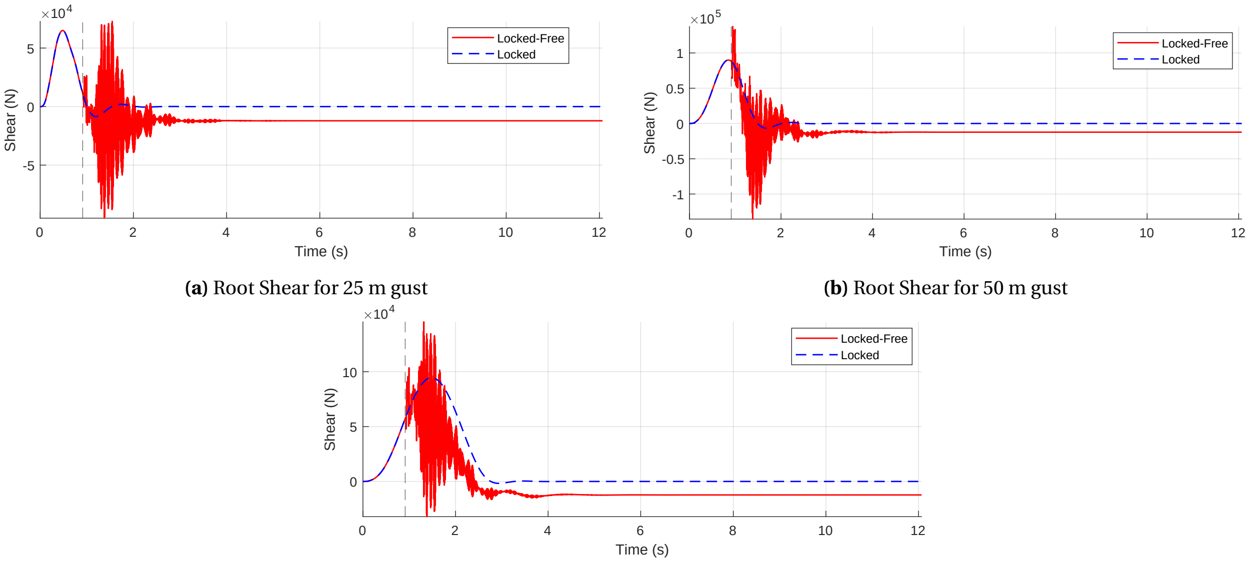

(a) Root Shear for 25 m gust

(b) Root Shear for 50 m gust

(c) Root Shear for 100 m gust

Figure A.3: Root chordwise shear plots for the different gust lengths, with hinge unlock at 0.9 seconds.

A.5. WRBM and Root Shear Plots with 5% Critical Damping

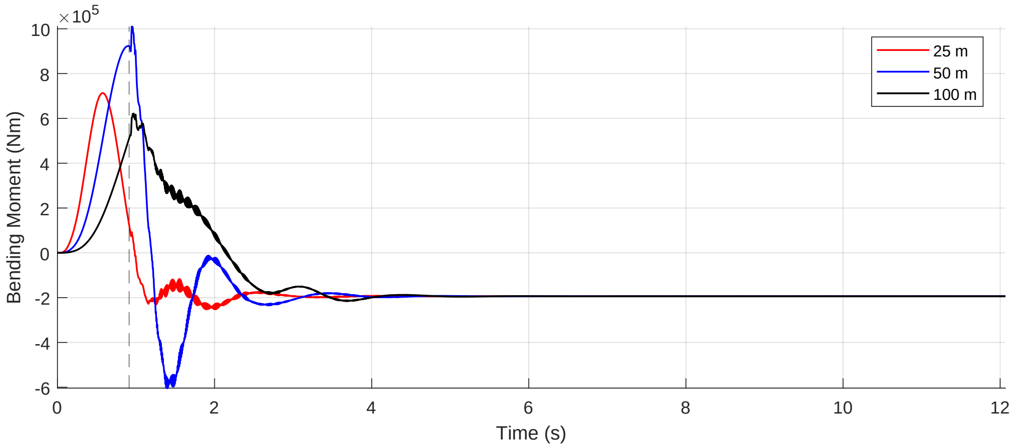

(a) Wing Root Bending Moment over time

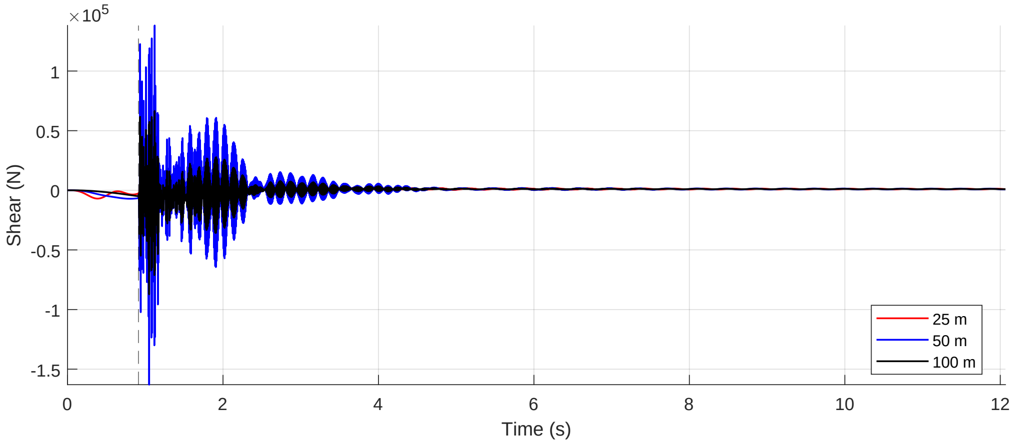

(b) Shear load at root over time

Figure A.4: Reaction WRBM and root shear load with a 10 degree flare and 5% structural damping

A.6. WRBM and Root Shear Plots with Numerical Diffusion Parameter of 0.001

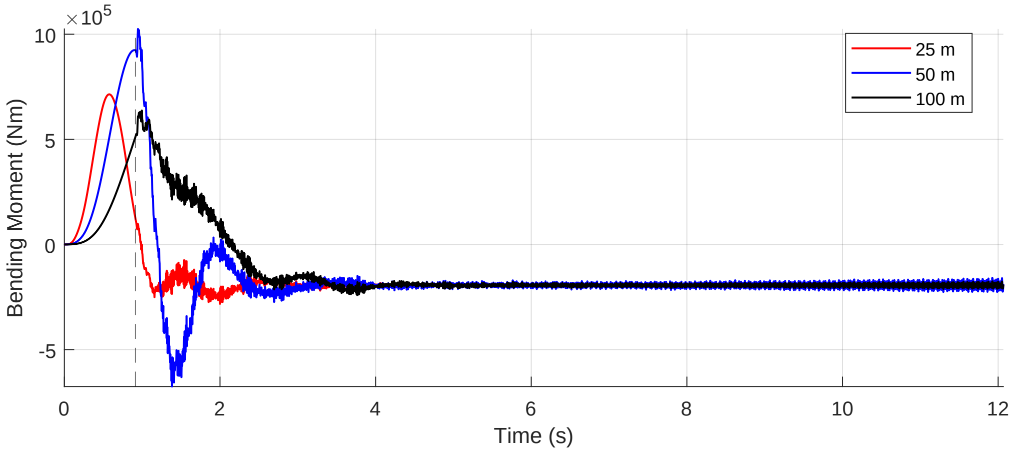

(a) Wing Root Bending Moment over time

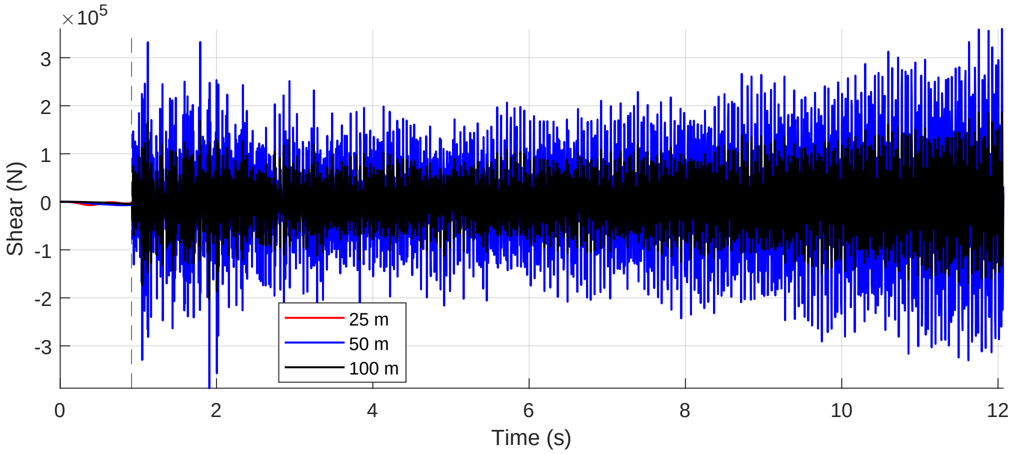

(b) Shear load at root over time

Figure A.5: Reaction WRBM and shear load at the root with a 10 degree flare and a diffusion parameter of 0.001